Characterising Molecules and Molecular Interactions on Surfaces

6.1 Vibrational Spectroscopies

6.1.1 Introduction

While the techniques described in Chapter 2 allow one to determine the elemental composition of a surface, they do not, at least as discussed in that early chapter, provide information on the chemical bonding of the surface atoms and, in particular, they do not identify the molecular character or integrity of any adsorbed species. As a spectral fingerprint of molecular character, vibrational spectroscopies are particularly effective. Most internal vibrational modes within an adsorbed molecule are closely similar to those of the free-gas-phase species, although strong bonding to the surface or partial fragmentation through bond breaking can modify some modes, providing a good indication of the nature of the bonding and the surface chemistry. The vibrational spectroscopy of molecular adsorbates on surfaces thus offers the possibility of (i) identifying the surface molecular species (are these the intact molecules initially adsorbed or has some dissociation or reaction occurred?) and (ii) obtaining information on the orientation and perhaps the adsorption site of the adsorbed molecules. These vibrational modes of the adsorbed species on a surface can be investigated by a number of methods, most notably by reflection-absorption infrared spectroscopy (RAIRS, also known as infrared reflection-absorption spectroscopy, IRRAS or IRAS) and high-resolution electron energy loss spectroscopy (HREELS), but also by inelastic electron tunnelling spectroscopy (IETS), Raman spectroscopy, sum frequency generation (SFG) and inelastic atom scattering. Notice that while energies in this book are generally expressed in eV, and indeed vibrational energies in the HREELS technique are commonly expressed in meV, in many optical techniques it is still common to express energies in terms of the inverse wavelength, $1/\lambda$, generally referred to as the wavenumber, in cm⁻¹ units. The underlying relationship is $E = hc/\lambda$ with E in joules and λ in m⁻¹; thus E (in meV) = $(e/hc) \times 10^{-5} (1/\lambda \text{ in cm}^{-1}), \text{ or } 1 \text{ meV} = 8.06 \text{ cm}^{-1}.$

6.1.2 Reflection-Absorption Infrared Spectroscopy

Historically, the use of infrared light in surface studies began with the experiments of Eischens, Pliskin and coworkers (see Eischens & Pliskin, 1958), who investigated the infrared absorption due to molecular adsorbates on dispersed metal particles on oxide supports by transmission of the light through a (compressed powder) sample.

In reflection–absorption infrared spectroscopy (RAIRS) the absorption of infrared radiation due to the excitation of vibrational modes of the adsorbates is measured after reflection from a plane substrate surface, most commonly that of a metal. Energy is extracted from the radiation field when the frequency of the light matches the eigenfrequency ω of the dipole-active oscillator and it is ultimately converted to heat via the anharmonic coupling of the infrared-active oscillators to all eigenmodes of the system. The interaction between the radiation and the vibrating dipole is due to the force exerted on the charge e^* (the effective ionic charge of the oscillator) by the electric field of the light wave. The wavelength of light is long compared with atomic distances, so the excitation is almost completely in phase for neighbouring dipoles. For an adsorbate mesh this is equivalent to the statement that the wavevector k_{\parallel} of the surface wave is large, where k_{\parallel} is the component of the wavevector parallel to the surface; k_{\parallel} can be written in terms of the wavevector component $k_{\rm L}$ of the incident light and the angle of incidence $\theta_{\rm i}$ (relative to the surface normal) as

$$k_{\parallel} = k_{\rm L} \sin \theta_{\rm i} \tag{6.1}$$

The RAIRS technique involves measuring the absorption spectrum in an adsorbed layer via the reflection losses as the wavelength is scanned through the absorption bands. An alternative version of the experiment is also possible. This involves measuring the changes in ellipticity of the reflected plane-polarised radiation that result from the different phase and amplitude changes, following reflection, of the components of the radiation electric vectors that lie parallel to the plane of incidence (*p*-polarisation) and perpendicular to it (*s*-polarisation). This technique of infrared ellipsometry (Stobie *et al.*, 1976) continues to find some applications in thin film characterisation but is not generally applied to molecular adsorbate characterisation.

The absorption of infrared radiation by thin films at a metal surface is strongly enhanced at high angles of incidence (i.e. grazing incidence) and is effectively limited to *p*-polarised radiation. This can be seen from a simple consideration of the electric fields produced by radiation at a bare metal surface. Figure 6.1 shows the incident and reflected vectors of the *s*- and *p*-polarised radiation components. At all angles of incidence the *s*-polarised component is

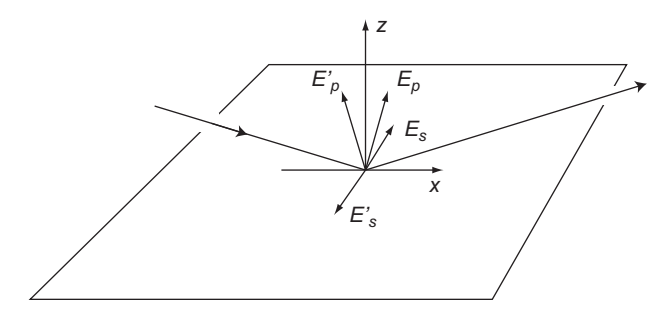


Fig. 6.1 The incident and reflected electric vectors of the p- and s-polarised radiation components at a metal surface. The plane of incidence is the xz plane.

practically reversed in phase upon reflection, and as the reflection coefficient is near unity the resultant of the incident and reflected vectors is close to zero at the surface. Consequently, the s-component cannot interact significantly with the surface dipoles. The p-component, however, suffers a phase change that varies strongly with the angle of incidence. As shown in Fig. 6.2, at grazing incidence the p-component can be enhanced to yield a nearly double resultant electric vector component, $E_{p\perp}$, perpendicular to the surface, whilst the tangential vector component $E_{p\parallel}$ is very much weaker. These two vector components form the major and minor axes of an elliptical surface standing wave. The p-component can, therefore, interact strongly only with vibrational modes of adsorbed species that have a dipole derivative perpendicular to the surface. This need for a component of the dynamic dipole moment to be perpendicular to the surface is a key selection rule for RAIRS studies of adsorbed molecules on conducting surfaces.

Figure 6.2 shows the angular dependence of the resultant amplitude of the electric field components at a bare metal surface relative to E_0 , the amplitude of the incident light, and demonstrates the pronounced maximum near grazing incidence. For a given incident beam width, the area of metal surface over which the enhanced field is effective increases as $1/\cos\theta_i$, and the intensity of absorption by a surface layer experiencing this field can be expected to depend on θ_i as $E^2 \sec\theta_i$. This intensity function is shown in Fig. 6.3 and reproduces the angular dependence of the absorption function deduced theoretically by Greenler (1966). The key conclusion is that only perpendicular dipole components can be detected by RAIRS.

A more quantitative treatment of RAIRS, albeit simpler than that of Greenler (1966) mentioned above, is based on the linear approximation theory of McIntyre & Aspnes (1971); this approximation is justified because the change in reflectivity

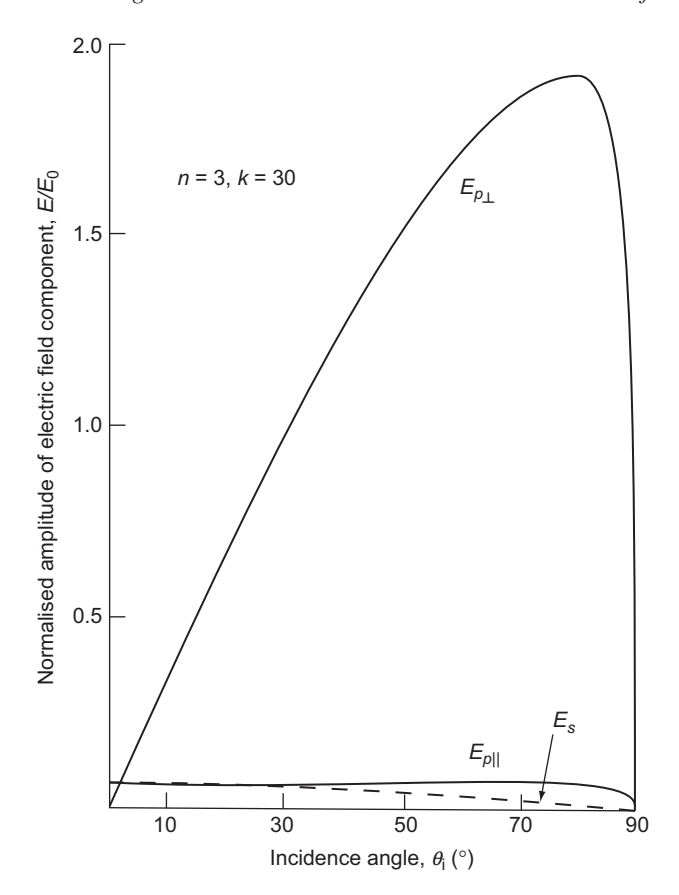


Fig. 6.2 Angular dependence of the resultant amplitude of the electric field components at a bare metal surface relative to E_0 , the amplitude of the incident beam, for a surface with refractive index n=3 and absorption index k=30; k is a measure of the attenuation per vacuum wavelength λ .

due to adsorbates, $\Delta R/R$, is always small. In addition, only terms that are linear in the concentration of adsorbates are considered, an approximation justified by experimental results, at least at low coverages. In this simple theory the adsorbate layer is regarded as a homogeneous film of thickness d, which is much less than the wavelength λ . Linear approximations lead to equations (6.2) and (6.3), where ε_1 , ε_2 and ε_3 are the complex dielectric constants of the ambient atmosphere (a vacuum in the present case) of the thin isotropic film and of the substrate respectively; n_1 , n_2 and n_3 are the corresponding refractive indices (see Fig. 6.4):

$$(\Delta R/R)_s = (8\pi dn_1 \cos \theta_i/\lambda) \operatorname{Im} \frac{\varepsilon_2 - \varepsilon_3}{\varepsilon_1 - \varepsilon_3}$$
(6.2)

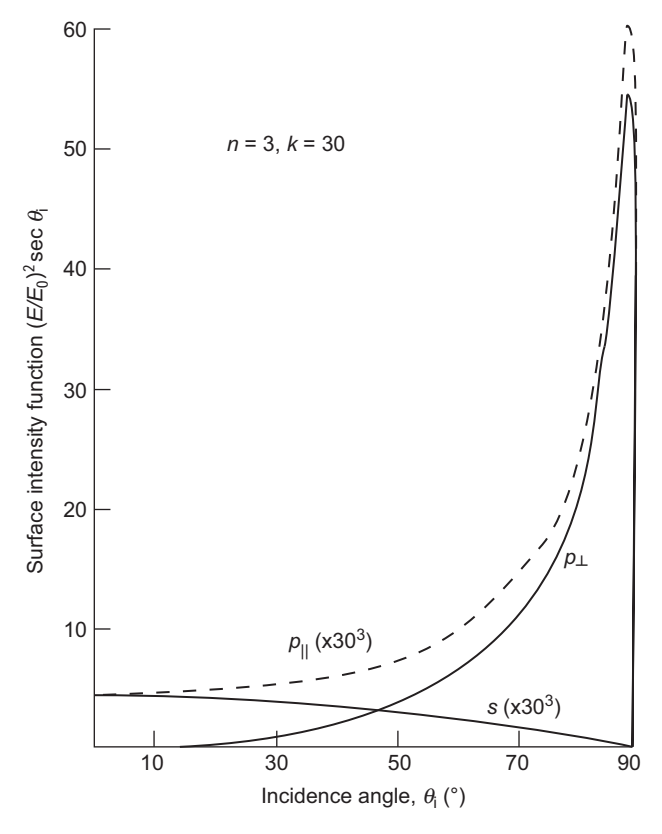


Fig. 6.3 Surface intensity function $(E/E_0)^2$ sec θ_i for the electric field components at a bare metal surface of refractive index n = 3 and absorption index k = 30.

$$(\Delta R/R)_{p} = (8\pi dn_{1}\cos\theta_{i}/\lambda) \times \operatorname{Im}\left\{\left(\frac{\varepsilon_{2} - \varepsilon_{3}}{\varepsilon_{1} - \varepsilon_{3}}\right) \left[\frac{1 - (\varepsilon_{1}/\varepsilon_{2}\varepsilon_{3})(\varepsilon_{2} + \varepsilon_{3})\sin^{2}\theta_{i}}{1 - (1/\varepsilon_{3})(\varepsilon_{1} + \varepsilon_{3})\sin^{2}\theta_{i}}\right]\right\}$$
(6.3)

The s and p subscripts refer to light polarisation perpendicular and parallel to the plane of incidence, respectively, as described above.

In the infrared region, ε_3 for metals is usually much larger than ε_2 ; for example, for Pt $\varepsilon_3 \approx -120 + 340$ i at a λ^{-1} value of 2200 cm⁻¹, whereas a 0.25 ML CO layer on Pt{111} has $\varepsilon_2 = 1 + 2$ i (Ibach, 1977), so $(\Delta R/R)_s$ is then negligible. This result is consistent with the near-perfect cancellation of the incident and reflected *s*-components of the radiation shown in Fig. 6.2. Applying the same approximation to equation (6.3) leads to

$$(\Delta R/R)_p = \frac{8\pi d \sin^2 \theta_i}{\cos \theta_i \lambda} \operatorname{Im}(-1/\varepsilon_2)$$
 (6.4)

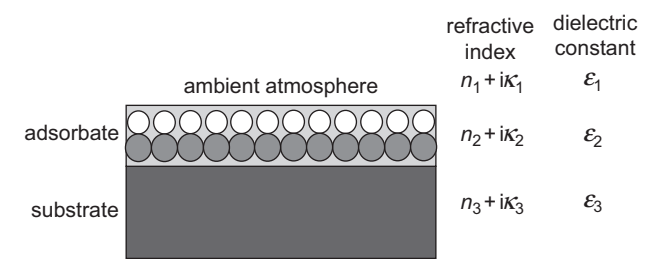


Fig. 6.4 Labelling system for the ambient atmosphere, adsorbate and substrate, showing the respective refractive indices and dielectric constants.

If the absorption index in the film, κ_2 , is small then this further approximation leads to

$$(\Delta R/R)_p = \left(\frac{\sin^2 \theta_i}{\cos \theta_i n_2^3}\right) 4\pi \kappa_2 d/\lambda \tag{6.5}$$

The term in parentheses here gives the enhancement of absorption due to the reflection at a metal surface, whilst the term outside the bracket is the Beer's law attenuation coefficient that would be expected in transmission at normal incidence; in this situation, if I_0 is the incident intensity then the transmitted intensity is given by

$$I = I_0 \exp(-4\pi\kappa_2 d/\lambda) \tag{6.6}$$

In practice, the curve in Fig. 6.3 deviates from this angular dependence only when θ_i significantly exceeds 80°.

Ibach (1977) used equation (6.4) together with a harmonic oscillator model for ε_2 to derive a value for the effective dipole ionic charge e^* associated with the surface dipole derivative. The expression he obtained is

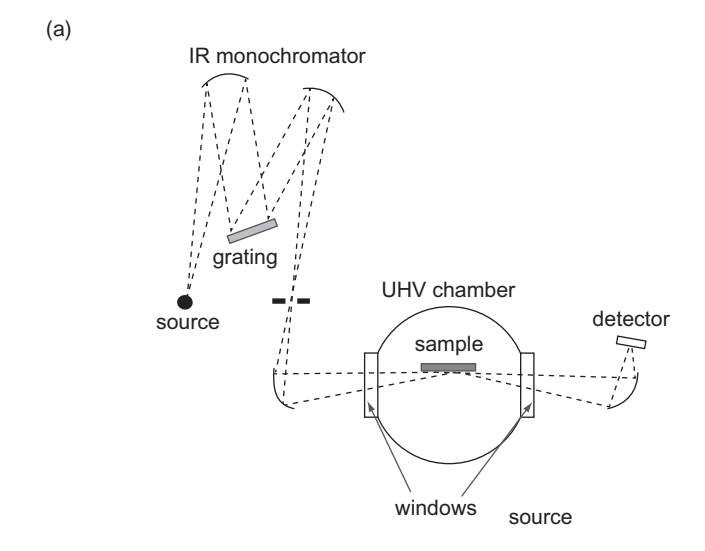
$$\left(\frac{\Delta R}{R}\right)_{p} d\omega = \frac{32\pi^{3}}{\lambda} \sin\theta_{i} \tan\theta_{i} N d\frac{e_{\perp}^{*}}{\mu\omega_{0}}$$
(6.7)

where N is the surface concentration of oscillators, e_{\perp}^* is the component of e^* in the direction of the polarisation of the light (perpendicular to the surface), μ is the reduced mass of the harmonic oscillator and ω_0 is the oscillator frequency.

Notice that for a transparent (insulating or semiconducting) substrate, rather than a metallic substrate, ε_3 is real (as is ε_1 for a vacuum), in which case

$$\operatorname{Im}\frac{\varepsilon_2 - \varepsilon_3}{\varepsilon_1 - \varepsilon_3} = -\frac{\operatorname{Im}\varepsilon_2}{\varepsilon_1 - \varepsilon_3} = \frac{2n_2\kappa_2}{n_1^2 - n_3^2} \tag{6.8}$$

As a consequence $\Delta R/R$ can be either positive or negative depending on the relative values of n_1 and n_3 . Thus while, on a metal surface, coupling to vibrational



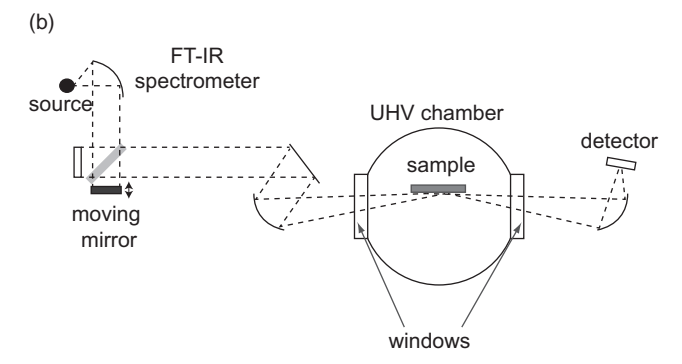


Fig. 6.5 Simplified schematic diagrams of two alternative arrangements for recording RAIR spectra based on (a) a scanning monochromator and (b) a Fourier transform interferometer.

states in the overlayer always leads to a reduction in the reflectivity, on transparent substrates some bands may appear as increased reflectivity (sometimes referred to as 'transmission' bands). An interesting example of this effect is in a RAIRS study of CO adsorption on Pb deposited on TiO₂(110) (Evans *et al.*, 1996); the observation of these 'transmission' bands for C–O stretching frequencies in this study indicated that the Pb was in small particles rather than a continuous film, so that the dielectric properties of the oxide substrate dominated the IR coupling mechanism.

Figure 6.5 shows the core ingredients of two different experimental approaches to obtaining RAIRS spectra from adsorbed layers on surfaces. Figure 6.5(a) shows the general approach of most early studies, in which monochromated radiation from a broad-band black-body infrared source (typically a 'globar') is reflected

from the surface before detection. Both the monochromator and detector are external to the UHV chamber containing the sample and are, at best, in lowvacuum enclosures; commonly they are in vessels at ambient pressure that can be purged with dry air or nitrogen to minimise the problem of atmospheric IR absorption, especially that due to water vapour. Infrared-transparent windows are used to separate the UHV and low-vacuum or ambient-pressure components of the system. The presence of these windows does place some limitation on the range of accessible wavelengths. For example, the absorption in CaF2 windows leads to a lower energy cut-off of accessible wavelengths of ~9 µm (i.e. ~1100 cm⁻¹); KBr windows extend the range to 25 μm (~400 cm⁻¹), but this material is hygroscopic with some attendant handling problems. Using this monochromator system, the base mode of operation is to record the intensity of the reflection spectrum both before and after adsorption and thereby extract the difference; clearly this places significant demands on the stability of source, sample geometry and optics as well as the atmosphere in the components outside the UHV chamber. Significantly better performance has often been achieved using wavelength or polarisation modulation. Polarisation modulation is effective because, using an unpolarised source, the absorption at the sample is only in the p-polarised component whereas in the surrounding gas phase both s- and p-polarisation components are absorbed equally. Typical detectors are liquid-nitrogen-cooled mercury cadmium telluride (MCT) photodiodes or liquid-helium-cooled bolometers.

The alternative approach, shown in Fig. 6.5(b), using a Fourier transform infrared (FT-IR) spectrometer, is favoured in the great majority of modern studies. It offers advantages in stability and speed of data collection and can benefit from the advances in commercial FT-IR instruments designed for more conventional IR absorption spectroscopy. As in the scanning monochromator approach, the spectrometer, detector and optical components are external to the UHV chamber and must be maintained in a suitable partial vacuum or purged gas environment.

Notice that, in common with other photon-in photon-out techniques, RAIRS is not constrained to investigate surfaces only in UHV. As such the UHV chamber shown in Fig. 6.5 may be the main chamber of a standard multi-technique surface science instrument, but alternatively it may be a small side-arm into which the sample can be transferred and isolated from the main chamber to allow exposure at much higher partial pressures of the reactant gases.

By far the most studied molecular adsorbate using RAIRS is CO, in large part because it gives intense absorption bands and is easily handled in a UHV system. However, there is also continuing interest in its important catalytic chemistry, such as in the water–gas shift reaction (CO + $H_2O \rightarrow CO_2 + H_2$) as a means of producing hydrogen from coal gasification, and in the 'three-way' catalysts used in automobile exhaust systems to oxidise CO and residual hydrocarbons and reduce nitrogen

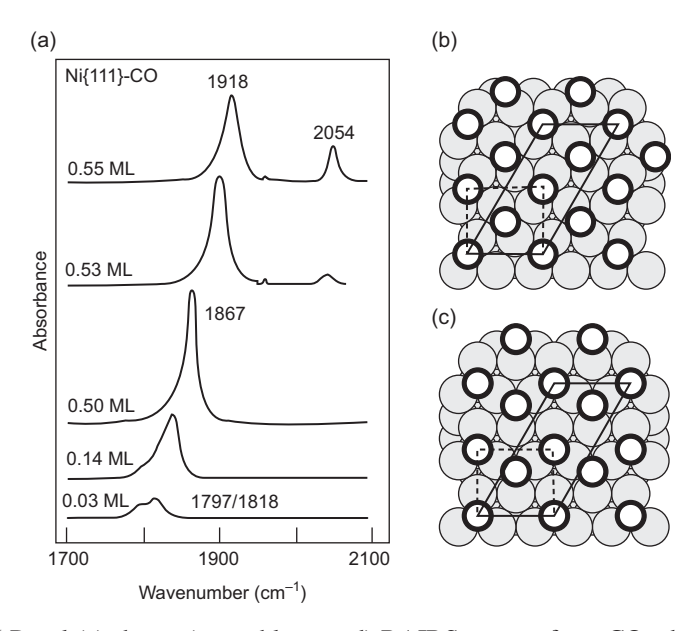


Fig. 6.6 Panel (a) shows (smoothly traced) RAIRS spectra from CO adsorbed on Ni{111} at various estimated coverages. Adapted from Chen *et al.* (1990) with estimated coverages based on Surnev *et al.* (1988). Also shown are two alternative models of the 0.50 ML c(4×2) structure for this system based on (b) bridging and (c) hollow sites. The c(4×2) unit mesh is shown by the full lines; the broken lines show the primitive $(2 \times \sqrt{3})$ rect. unit mesh.

oxides. A few results from these CO adsorption and reaction studies serve to illustrate some of the main aspects of the RAIRS technique.

Figure 6.6(a) shows RAIR spectra recorded from a Ni{111} surface with increasing coverages of adsorbed CO, adapted from the paper of Chen et al. (1990) but with coverage estimates taken from Surnev et al. (1988); the two publications show closely similar results, albeit with some differences in peak energies, particularly at 0.50 ML for which Surnev et al. report a value of 1903 cm⁻¹. Some features of these spectra are quite typical of results from CO adsorbed on different low-index metal surfaces, namely the occurrence of more than one peak at certain coverages and the shift of peak energies to higher energies with increasing coverage. All these peak energies are broadly consistent with a C-O stretching vibration with the CO in different bonding environments. Coveragedependent shifts of this vibrational band when CO molecules retain the same local substrate adsorption site are known to arise from two factors, dynamic dipole coupling and a so-called chemical shift. The first mechanism is simply the result of a shift in the normal mode of a collection of identical dynamic dipoles perpendicular to a surface as they are moved closer together; this always results in an upward shift of the energy with increasing coverage. The 'chemical' effect arises from a modification of the electronic bonding of the individual molecules as the coverage increases; this can cause either an upward or a downward shift. The two effects can be distinguished by RAIRS studies of a mixture of two different CO isotopes (the different masses give different vibrational frequencies for the isolated molecules), using different relative and absolute coverages. In particular, in the limit of a very dilute component of one isotope there is no dynamic dipole coupling of these molecules with the molecules of the second (majority-coverage) isotope; in this case any shift in the frequency associated with the minority species due to changes in the total coverage can arise only from the electronic or chemical effect. The underlying theory of these mixed isotope studies was developed by Hammaker *et al.* (1965), and its exploitation was described by Crossley & King (1977, 1980).

In interpreting the different coexistent states that must give rise to multiple C=O stretching frequencies in the same spectrum, results from coordination compounds in which CO is known to be coordinated to different numbers of metal atoms have provided an important benchmark. This approach was first used by Eischens and coworkers (see Eischens & Pliskin, 1958) in their (transmission-IR) studies of CO adsorption on oxide-supported metal particles but was then adopted in later RAIRS studies of adsorption on single-crystal surfaces. A review of these studies by Sheppard & Nguyen (1978) led to a definition of three spectral regions for the C=O stretching frequency, namely ~2130–2000 cm⁻¹ for (singly coordinated) atop sites, ~2000–1880 cm⁻¹ for (doubly coordinated) bridging sites and ~1880–1650 cm⁻¹ for (multiply coordinated) hollow sites.

On this basis, the RAIR spectra from CO on Ni{111} were interpreted as indicating that a fractional coverage of hollow sites may occur at low coverage, but then only bridging-site occupation occurs up to a coverage of 0.50 ML, with partial atop-site occupation appearing at the highest coverage. At 0.50 ML coverage a $c(4\times2)$ ordered phase is seen in LEED and a rather elegant model of this structure, based on the occupation of two rotationally inequivalent bridge sites (see Fig. 6.6(b)), was proposed that was fully consistent with this interpretation of the RAIRS data. The same structural phase, and comparable RAIRS data (albeit with less clear-cut frequency benchmarks) also observed for NO on this surface, were interpreted in the same way. However, Aminpirooz et al. (1992) noticed that the LEED pattern for the Ni $\{111\}c(4\times2)$ -NO phase showed missing diffracted beams characteristic of a glide symmetry that is inconsistent with the model of Fig. 6.6(b) and proposed, instead, the model of Fig. 6.6(c) in which the NO molecules occupy the two inequivalent hollow sites, directly above a second-layer Ni atom (an 'hcp site') and directly above a third-layer Ni atom (an 'fcc site'). Subsequently, scanned energy mode photoelectron diffraction results from the Ni $\{111\}$ c(4×2)–CO phase provided clearly quantitative evidence that this same 'mixed-hollow' structure (Fig. 6.6(c)), and not the bridge-site model of Fig. 6.6(b), is the true structure (Schindler *et al.*, 1993; Davila *et al.*, 1994). An independent quantitative LEED analysis (Mapledoram *et al.*, 1994) led to the same conclusion. The fact that a C–O stretching band at ~1900 cm⁻¹ could be due to hollow-site adsorption clearly highlights the need for caution in the application of simple site assignments based on coordination compounds, presumably because of a strong coupling shift in this specific system.

Despite this caveat in the interpretation of RAIR spectra in terms of specific local adsorption sites, it is a technique that remains of particular value in studying surface reactions, particularly under gas-phase reaction conditions. As remarked above, one motivation for the study of CO (and NO) adsorption on certain transition metal surfaces is to gain a better understanding of the important reaction of NO and CO over an appropriate catalyst in an automobile exhaust system to produce N₂ and CO₂. The reaction is known to occur at appropriate surfaces, a key step being the dissociation of NO into atomic N and O, with N atoms coming together to give off N2 gas and adsorbed O and CO reacting to produce gas-phase CO₂. This process has been identified, for example, over Pt{100}. The detailed mechanisms are complex, not only involving the varied mixing of reacting species on the surface but also, under certain conditions, a structural phase transition of the Pt{100} surface. Specifically, the outermost layer of the equilibrium clean Pt{100} surface undergoes reconstruction to a close-packed hexagonal layer (the 'hex' phase) but, with sufficient adsorbates present, this 'unreconstructs' to a (1×1) phase. At temperatures below that required for NO dissociation (~400 K) the (intact) NO is adsorbed more weakly than CO and exposing a NO-covered surface to CO leads to the CO displacing the NO on the surface even in the continued presence of a partial pressure of NO, as shown by the FT-RAIR spectra of Fig. 6.7(a). With NO alone in the gas phase the spectrum shows only the N-O stretching frequency around 1640 cm⁻¹, characteristic of NO bonded to atop sites. When the CO partial pressure is introduced, this N–O peak is attenuated at the expense of two new peaks, C-O stretching modes of CO in bridging and atop sites at ~1870 and 2060 cm⁻¹, respectively. Notice that the N–O peak shows a significant coverage-dependent shift, as seen in the C-O peak in Fig. 6.6 on Ni{111}. The data shown in Fig. 6.7(a) were recorded with a sample temperature of 390 K, but essentially the same behaviour is seen at 300 K. Repeating this experiment at 410 K, however, when NO dissociation can now occur, leads to very different results, as seen in Fig. 6.7(b). In this case introducing the CO leads to very little change in the RAIRS, which remains dominated by the N-O stretching mode although a weak feature with the appearance of a doublet can be seen at around the expected spectral range of an atop C-O stretching frequency. This is accompanied by a sharp rise in the CO₂ partial pressure, which shows a weak damped oscillation with time. At the lower temperature, the adsorbing CO simply replaces adsorbed NO and leads to an equilibrium state.

At the higher temperature, NO dissociation leads to a mechanism for removing any CO that adsorbs, and in this case the final state is not an equilibrium state but that of a steady-state reaction.

The weak modulations in the CO₂ production rate seen in Fig. 6.7(b) are consistent with the fact that in this temperature range the reaction is known to display spontaneous oscillations in the kinetics; in fact these oscillations are both temporal and spatial (cf. the spatial patterns in CO oxidation seen using PEEM on Pt{110} and displayed in Fig. 4.33(a)). Because of this the RAIRS data of Fig. 6.7 (b) are almost certainly a result of some spatial average over an inhomogeneous surface. Some further insight into the underlying time-dependent reaction mechanism using RAIRS has been achieved by applying a weak temperature modulation to produced forced, rather than spontaneous, oscillations. In this way one may expect the spatial variations to be significantly weaker. The use of forced

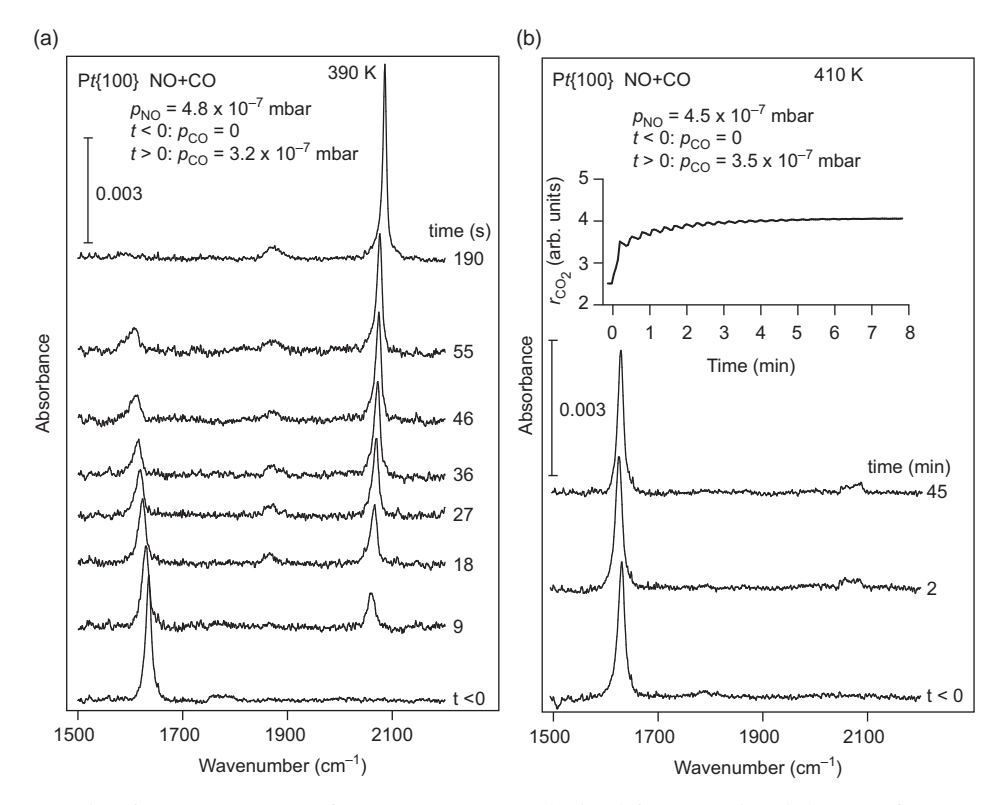


Fig. 6.7 (a) Sequence of FT-RAIR spectra obtained from a Pt{100}(hex) surface initially exposed to 4.8×10^{-7} mbar of NO at 390 K, following introduction to the chamber of CO at a partial pressure of 3.2×10^{-7} mbar. (b) Results from essentially the same experiment but at a sample temperature of 410 K. The inset in (b) shows the corresponding relative CO₂ production rate as a function of time. Reprinted from Miners *et al.* (2003), copyright 2003, with permission from Elsevier.

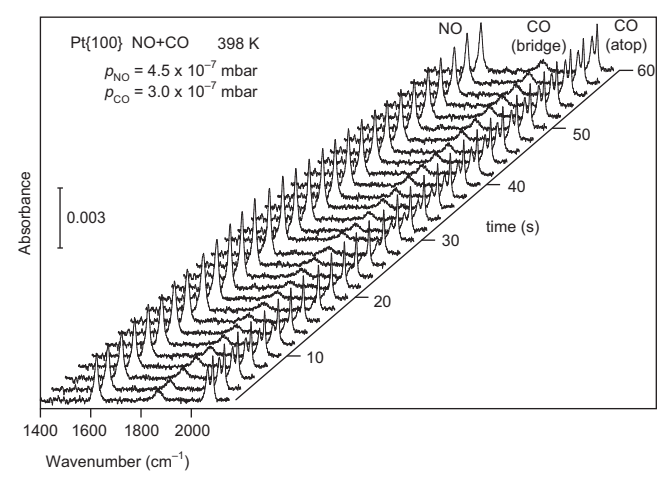


Fig. 6.8 FT-RAIR spectra recorded from Pt{100} exposed to an NO–CO gas mixture through the oscillatory surface reaction, forced by an imposed temperature modulation of 2.5 K. Reprinted with permission from Miners *et al.* (2004). Copyright 2004 American Chemical Society.

oscillations also ensures that the exact frequency and phase of the oscillations is known, so data averaging over multiple cycles can allow results for enhanced spectral and temporal resolution to be obtained. An example of data collected in this way is shown in Fig. 6.8. Specifically, a peak-to-peak temperature modulation of 2.5 K with period 1 minute was applied to a Pt{100} sample at a nominal temperature of 398 K while exposed to a 1.5:1 NO: CO gas phase mixture at a total pressure of 7.5×10^{-7} mbar; FT-RAIR spectra were recorded at intervals of 250 ms, over multiple cycles, the spectra recorded at the same relative time within each cycle then being added. In order to enhance the data quality further, blocks of eight successive spectra were also summed, leading to 30 final spectra at 2 s intervals within the temperature oscillation. Mass spectrometer measurements made at the same time showed strong modulations in the CO₂ production rate and related fluctuations in the NO partial pressure. The RAIR spectra show the presence of N-O and C-O stretching frequencies consistent with atop NO, bridge CO and atop CO at all times within the cycle, with some modulation of the intensity of the atop NO and bridging CO. Most striking, however, is that there are clearly two absorption bands in the energy range, attributable to atop CO at ~2065 cm⁻¹ and ~2085 cm⁻¹, but, while the amplitude of the former of these peaks is strongly modulated, that of the latter is essentially unchanged. These two bands were assigned to CO intermixed with NO, and to CO in pure CO islands (leading to an upward energy shift due to vibrational coupling). The fact that the atop NO band was observed at 1628 cm⁻¹, rather than ~1640 cm⁻¹ as seen for pure NO islands in Fig. 6.7(a), is also consistent with the atop NO in Fig. 6.8 being

intermixed with CO rather than in pure NO islands. Evidently it is in these intermixed islands that a reaction takes place between the CO and NO as it dissociates. Detailed comparison of the relative phases of the variations of partial pressures and RAIRS peaks within the cycles provides more detailed information on the exact reaction mechanism.

One feature of the RAIRS technique that should be evident from these examples is the rather high resolution of the technique; the peaks are narrow relative to the total spectral range recorded, and subtle effects due to small shifts can be distinguished. Indeed, one can detect not only large frequency shifts that distinguish the same molecular species in different bonding sites but also much smaller shifts due to differences in local environment, such as whether other equivalent molecules that can induce dipole coupling shifts are nearby. There are also many studies of stepped surfaces showing that adsorption at step-edge sites and even kink sites can be distinguished from adsorption at terrace sites. The spectra shown in Fig. 6.7 and 6.8 were recorded with an instrumental resolution of 2 cm⁻¹, but achieving a somewhat higher resolution is relatively straightforward. It is notable, though, that the actual linewidths of the C-O and N-O stretching vibrations are not so narrow as to be limited by this instrumental resolution indeed, in the spectra presented here, peak widths of ~20 cm⁻¹ or more are seen although, using an infrared diode laser, a linewidth (FWHM) as low as 2.3 cm⁻¹ has been reported for the atop C-O stretching band of CO on Pt{111} at a sample temperature of 100 K (Sutcu et al., 1991). The fundamental limitation on the linewidth δE in a vibrational band is determined by the lifetime of the excited state τ , through the uncertainty principle:

$$\delta E = \hbar/\tau \tag{6.9}$$

For an isolated molecule in the gas phase this lifetime is $\sim 10^{-8}$ s, leading to a predicted linewidth $\sim 5 \times 10^{-4}$ cm⁻¹. In reality gas-phase measurements show very much larger values of the linewidth (~ 0.1 cm⁻¹ or more), owing mainly to the combined effects of intermolecular collisions and Doppler broadening. For molecules adsorbed on a surface, the situation is significantly different. In particular, the intrinsic lifetime of the excited state is very much shorter than in the gas phase, which can be attributed largely to coupling to phonons in the underlying solid; this provides a rapid decay route not available in the gas phase. Picosecond time-resolved experiments can measure this lifetime and in the case of the c(4×2) phase of CO on Pt{111} at 150 K, such measurements yielded a value of ~ 5 ps (Beckerle et al, 1990), which would lead to a linewidth of ~ 1 cm⁻¹. Evidently other effects must lead to further broadening in practice, and the main contribution is believed to be from 'dephasing', a process in which a phonon scatters elastically off a vibrating molecule, disrupting its phase without changing its energy. In some cases the

dephasing is dominated by a single adsorbate vibrational mode at lower frequency, which is strongly damped by the coupling to substrate phonons. In the case of CO adsorption on Ni{100} and Ru{100}, Persson *et al.* (1986) showed that the experimentally observed broadening of the C–O stretching frequency can be accounted for in this way through coupling to a (much lower frequency) frustrated rotational mode of the adsorbed molecule. Of course, further broadening can also result from an inhomogeneous surface; for example, the adsorbed molecules may have varying numbers of neighbouring molecules.

6.1.3 High-Resolution Electron Energy Loss Spectroscopy

An alternative approach to investigating the vibrational modes of adsorbed molecules on surfaces, which has some similarities in selection rules to RAIRS, is the technique of high-resolution electron energy loss spectroscopy (HREELS). In this method monochromatic low energy electrons (generally with energies less than ~10 eV) are directed at a surface and the scattered electrons (mainly in the specular direction) are energy analysed; peaks are detected in the energy loss spectrum associated with the excitation of vibrational states on the surface. In some ways the commonly used name of the technique is something of a misnomer, because the spectral resolution achievable in HREELS is significantly worse than in RAIRS (so that some researchers prefer the acronym VEELS, where the 'V' stands for vibrational), but the term 'highresolution' is relative to that obtained by the use of electron energy loss spectroscopy (EELS) to study electronic, rather than vibrational, energy losses. In particular, EELS is used in transmission electron microscopy to study energy losses associated with core-ionisation events in a sample. Relative to other forms of electron energy loss spectroscopy, therefore, HREELS is high-resolution, and indeed the need to resolve vibrational energies that may be separated by only a few meV means that the experiment requires the use of two dispersive electron energy analysers, one operated in reverse to produce a monochromatic electron beam from a typical thermionic electron source with natural energy spread ~0.5 eV. A simple schematic diagram of an HREELS experiment is shown in Fig. 6.9.

The partial similarity of HREELS and RAIRS in vibrational spectroscopy arises because they share a common dipole-excitation mechanism. When an electron approaches the surface, the electric field of the electron exerts a force on dipole-active oscillators. For the same reason as in RAIRS, this electric field is practically normal to the surface, so the same selection rule regarding the orientation of the surface dipole oscillator applies. Because of the long-range nature of the Coulomb field, the main contributions to the total interaction arise during the time when the electron is still far from the surface, on an atomic scale. The field is therefore nearly homogeneous on the atomic scale, so it is mostly long-wavelength surface waves that

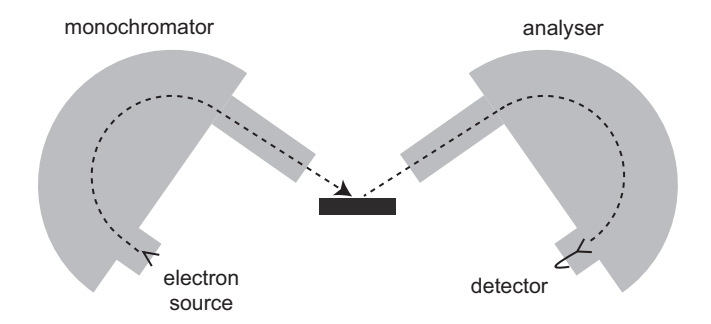


Fig. 6.9 Schematic diagram of the key components of an HREELS experiment. Two dispersive electron energy analysers are used, one operating in reverse as an electron monochromator. Concentric hemispherical analysers are shown here, but other designs are also commonly used.

are excited. As the electron approaches the surface, the lateral extension of the electric field, being a function of the distance from the surface, decreases and for this reason a continuous distribution of surface wavevectors is excited, unlike in RAIRS. In RAIRS the field is periodic in time, so only the fundamental frequency of a harmonic oscillator is excited (higher harmonics can be excited if the oscillator is anharmonic). By contrast, in HREELS the total interaction time is very short (only of order an oscillator period), so the oscillator experiences forces at all frequencies. This means that multiple excitations are possible, with a Poisson distribution in the excitation probabilities. In practice, though, for a single adsorbate layer the intensities of these multiple excitations are often too weak to be detected.

A quantum mechanical treatment of the inelastic scattering of electrons from an ordered surface lattice in the dipole scattering regime was first presented by Evans & Mills (1972). On the basis of their results Ibach (1977) gave the intensity of the energy loss, normalised to the elastically scattered intensity, for the case of specular reflection to be

$$S = 8\pi \widehat{E}_0^{-1} \widehat{p}_\perp^2 \widehat{N} \cos^{-1} \theta_i F(\alpha, \theta_i)$$
 (6.10)

Quantities labelled by a caret are in atomic units, E_0 and θ_i are the energy and polar angle of the incident electrons, p_{\perp} is the perpendicular component of the dipole moment and $F(\alpha, \theta_i)$ is an angular term given by

$$F(\alpha, \theta_i) = \left[\left(\sin \theta_i - 2\cos^2 \theta_i \right) / \left(1 + \alpha^2 \right) \right] + \left(1 + \cos^2 \theta_i \right) \ln \left(1 + 1/\alpha^2 \right)$$
(6.11)

with

$$\alpha = \theta_{\rm E}/\theta_{\rm c}, \ \theta_{\rm E} = \hbar\omega \ /2E_0$$
 (6.12)

where θ_c is the acceptance angle of the electron spectrometer (out of the exact specular direction), which is assumed to have a circular aperture. In practice, this is the angle where the intensity of the elastic peak has fallen to half its maximum value. It is possible to show that the relative intensity S is given by

$$S = 4\pi \left(1836\hbar\widehat{\omega}\widehat{E}_0\right)^{-1}\widehat{N}\left(\widehat{e}^{*2}/\widehat{\mu}\right)\cos^{-1}\theta_i F(\alpha, \theta_i)$$
 (6.13)

The previous result is found to apply when specular reflection is sharp, which occurs when the surface lattice is well ordered. For disordered lattices, and for coverages at which a full regular surface lattice is not complete, the situation is more complicated. As a consequence the intensities of the peaks in HREELS are not simply linear in the coverage, even if e^* is independent of coverage.

As remarked above, the incident electrons excite surface phonons with a continuous distribution of wavevectors, and the distribution is different parallel and perpendicular to the plane of incidence. The angular distribution of the scattered energy-loss electrons around the specular angle therefore depends on both the polar angle θ and the azimuthal angle ψ relative to this specular direction. The angular dependence of the differential cross-section averaged over ψ is given by

$$\frac{\overline{\mathrm{dS}}}{\mathrm{d\Omega}} \propto \frac{(1 + \cos^2 \theta_{\mathrm{i}})}{\cos \theta_{\mathrm{i}}} \vartheta \frac{(\vartheta^2 + \gamma^2 \vartheta_{\mathrm{E}}^2)}{(\vartheta^2 + \vartheta_{\mathrm{E}}^2)^2} \tag{6.14}$$

where $\gamma^2 = 2 \sin^2 \theta_i / (1 + \cos^2 \theta_i)$ and Ω is the solid angle.

These averaged cross-sections, normalised to the values at $\theta=0$, are plotted as a function of $\theta/\theta_{\rm E}$ in Fig. 6.10. It can be seen that $\overline{\rm d}S/{\rm d}\Omega$ falls rather rapidly to begin with and tails off smoothly for higher θ . The broken lines indicate the acceptance limits for typical spectrometer conditions ($\theta_{\rm c}=1.5^{\circ}$, $E_0=5$ eV) corresponding to inelastic phonon energy losses of 100 and 300 meV. Notice that the angular distribution around the specular beam is narrower at increasingly grazing-incidence conditions. When $\theta_{\rm c}>\theta_{\rm E}$, most of the inelastic intensity is accepted by the analyser. If the surface is disordered, this spreads both the elastic and inelastic intensity by approximately the same factor, and the ratio S of equation (6.13) remains essentially unchanged. However, if the condition $\theta_{\rm c}>\theta_{\rm E}$ is not fulfilled then S for disordered surfaces will be larger than the value given by this equation.

In contrast with the small-angle inelastic scattering, associated with the farfield dipole excitation mechanism, that is detected in a relatively narrow lobe around the specular (elastically scattered) beam, a quite different mechanism leads to large-angle inelastic scattering. This 'impact scattering' mechanism

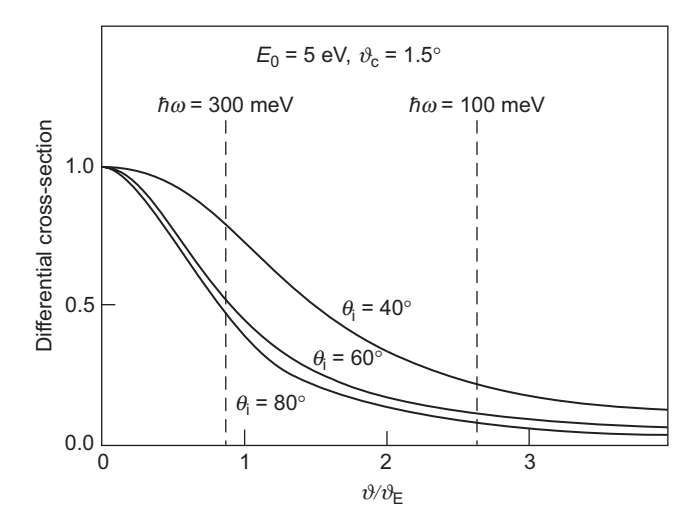


Fig. 6.10 Differential cross-section (normalised to the values at $\theta/\theta_{\rm E}=0$) for the inelastic phonon scattering of electrons from a metal surface, averaged over the azimuth, versus $\theta/\theta_{\rm E}$. The broken lines indicate the acceptance angle limits for typical spectrometers at different values of the phonon energy loss. After Ibach (1977).

involves the local interaction of the electrons and surface atoms in a similar fashion to that of elastic scattering in LEED, but the instantaneous local disorder induced by the surface vibrations causes the electrons to be scattered out of the diffracted beams into the thermal diffuse background. The theoretical treatment of this process, which requires explicit consideration of the local atomic potentials and the effects of multiple scattering (as in LEED theory), was first presented by Tong *et al.* (1980), who found that the probability that the electron scatters into a solid angle $d\Omega$ is given by

$$\frac{\mathrm{d}P}{\mathrm{d}\Omega} = \frac{mE_0}{2\pi^2\hbar^2} \frac{\cos^2\theta_s}{\cos\theta_i} S |M(\mathbf{k}_i, \mathbf{k}_s; Q_{||j})|^2$$
(6.15)

where θ_s is the scattered polar angle, S is the surface area and M is the matrix element describing the scattering of the electron from \mathbf{k}_i to \mathbf{k}_s by a phonon of wavevector Q_{\parallel} and polarisation in the surface layer j. To illustrate some features of this theory these authors calculated the energy and angular dependence of the impact scattering probability from two different vibrational modes of a model system, namely CO adsorbed on Ni{100}. These two modes are the C–O stretching mode perpendicular to the surface (also dipole active and detected in RAIRS, as described in the previous section, at ~250 meV) and, at a much lower energy (< ~20 meV), the frustrated translational mode of the CO molecule parallel to the

surface. The predicted angular dependences are shown in Fig. 6.11 for incidence angle 30° with detection in the plane of incidence that contains the surface normal. The angular dependence of the scattering from the (non-dipole-active) mode parallel to the surface actually shows zero intensity in the specular direction ($\theta_s = 30^\circ$); this is a symmetry-dictated zero, arising from the combination of time-reversal symmetry and reflection symmetry in a plane perpendicular to the scattering plane. The excitation of the dipole-active mode perpendicular to the surface also differs markedly from that due to dipole excitation, but the impact mechanism is estimated to lead to an intensity that is two orders of magnitude smaller than the dipole mechanism; so, for this mode, impact scattering contributes only a broad weak background to the narrow dipole lobe of Fig. 6.10. One notable feature of equation (6.15) is that the probability of impact-mode scattering increases with increasing incident energy. This contrasts with the situation for dipole scattering, for which higher energies lead to reduced intensity (equation 6.13). Therefore HREELS experiments measured in the specular direction and

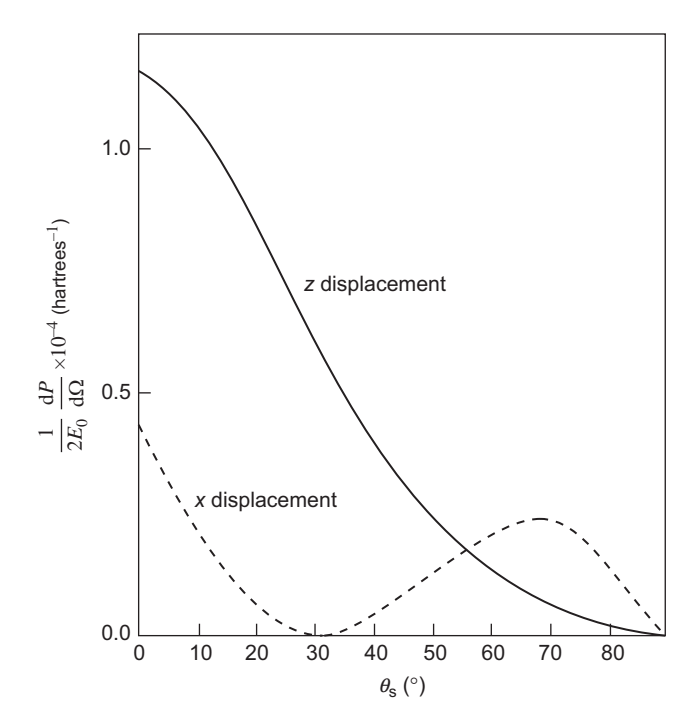


Fig. 6.11 Calculated angular dependence of CO vibrational modes, perpendicular and parallel to a Ni $\{100\}$ surface (involving z and x displacements respectively), due to impact-mode scattering with an incident angle of 30° . Reprinted with permission from Tong *et al.* (1980). Copyright 1980 by the American Physical Society.

detecting the dipole-active modes are typically conducted at incident energies ~5–10 eV, whereas the off-specular detection of impact scattering may use much higher energies (up to ~200 eV). Of course, the fact that impact scattering involves coherent multiple scattering processes similar to those in LEED means that the incident energy dependence of the intensity of these modes does not vary monotonically but shows strong modulations similar to those of LEED intensity–energy spectra. As in LEED, these modulations contain structural information, although the potential to develop this aspect of HREELS has not been pursued extensively. A slightly later paper by Tong *et al.* (1981) provided a more extensive evaluation of the selection rules for impact scattering from molecules on surfaces, also discussed in the book devoted to the HREELS technique by Ibach & Mills (1982).

A relatively simple example of the way in which specular (dipole) and off-specular (impact mode) HREEL spectra can provide information on the nature and geometry of an adsorbed molecule on a surface is provided by an investigation of the reaction of formic acid (HCOOH) with a Ni{110} surface by Jones *et al.* (1989). Formic acid deprotonates on many metal surfaces to form a formate (HCOO) species (see the top right diagram in Fig. 6.12) and a range of experiments have shown this to be the case for Ni{110}. Figure 6.12 shows some data from this study, which included spectra recorded from both HCOOH and the deuterated DCOOH; the isotope shift of vibrational modes involving the hydrogen atom aided identification of the observed spectral peaks. All the spectra shown in Fig. 6.12 are from the deuterated species, recorded using incident energy 14 eV and incident angle 50°. The off-specular data were recorded at emission angle 60°.

The specular HREEL spectrum (recorded in the $[1\overline{1}0]$ azimuth) shows the main dipole active modes, and these are labelled on the spectrum. As shown in Fig. 6.13 the observed modes correspond to those expected to have a dynamic dipole moment perpendicular to the surface, for a formate species bonded to the Ni substrate symmetrically through the two O atoms and with the molecular plane perpendicular to the surface. By contrast the off-specular spectrum recorded in the same azimuthal direction shows additional peaks, most notably the asymmetric COO stretching mode, v_a (COO), which has a dynamic dipole moment parallel to the surface and so is not dipole active, together with some combination and overtone modes. As remarked in the previous section, overtone modes are not dipole active if the vibrations are harmonic but are detected in the impact mode. The $v_a(COO) + \delta(C-D)$ band is a combination of two modes with dynamic dipole moments parallel to the surface, which thus are not separately dipole active, but this combination of the two is dipole active and has been seen in RAIRS from formate on Cu{110}, albeit greatly enhanced in intensity through Fermi resonance with another dipole-active band at a very similar energy; further details of this

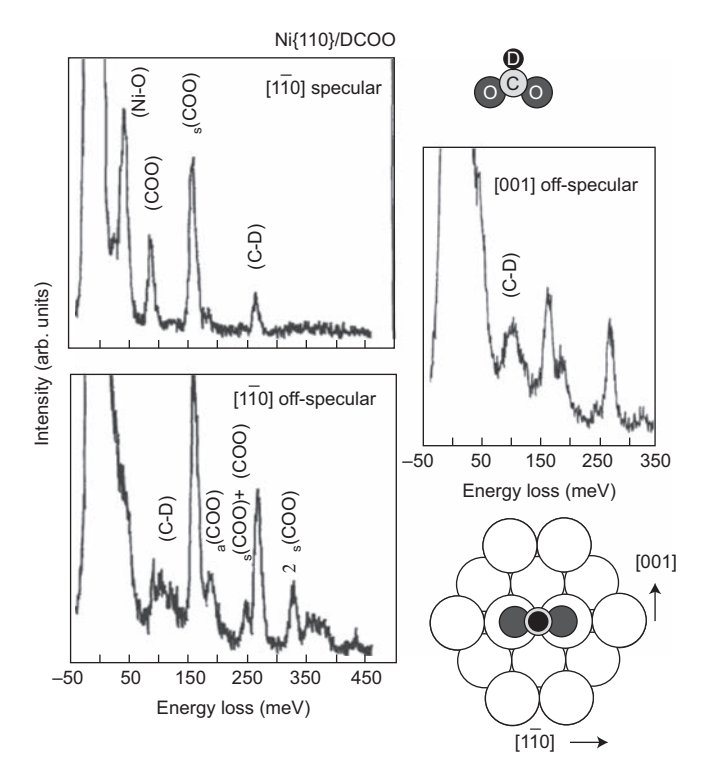


Fig. 6.12 HREELS data recorded from the deuterated formate species on Ni{110}. Reprinted with permission from Jones *et al.* (1989). Copyright 1989, AIP Publishing LLC. A schematic diagram of the local adsorption geometry found for this system, also giving the azimuthal directions on the surface, is shown in the lower right part of the figure.

effect and its observation were provided by Hayden *et al.* (1983). Evidently its observation here is enhanced by the impact mode.

Some further information on the molecular orientation can be extracted from the selection rules for the impact scattering modes. Specifically, if the scattering plane corresponds to a symmetry plane of the adsorbate + substrate structure then vibrations that are asymmetric with respect to this plane are impact-forbidden. Thus, observation of the $\delta(C-D)$ mode and absence of the $\pi(C-D)$ mode in the off-specular spectra recorded in the $\begin{bmatrix} 1\overline{1}0 \end{bmatrix}$ azimuth, with the opposite appearance of these modes in the $\begin{bmatrix} 001 \end{bmatrix}$ azimuth, was taken to imply that the molecular plane lies in the $\begin{bmatrix} 1\overline{1}0 \end{bmatrix}$ azimuth. Indeed, on the basis of the assignment of the weak feature at 29 meV in the specular HREELS to a nickel surface phonon, Jones *et al.* argued that this mode could only be dipole active if the formate species occupies the short-bridge site on the Ni{110} surface, as shown in Fig. 6.12. Further details of these arguments are given in Jones *et al.* (1989).

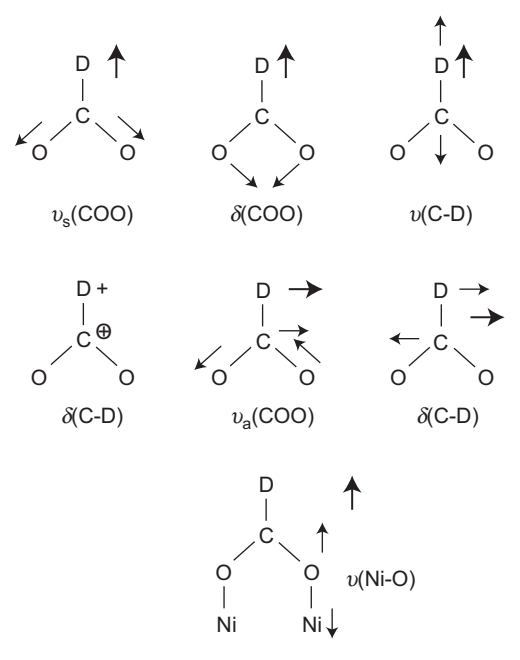


Fig. 6.13 The six normal modes of vibration of the free (deuterated) formate ion, together with one mode of vibration involving the bonding to the Ni substrate. The + symbol implies motion out of the plane of the diagram. The bold arrows and crossed circle identify the direction of the dynamic dipole moment.

While the dominance of the dipole-active $v_s(COO)$ mode in the specular spectra is unsurprising, it is striking that this peak also dominates the off-specular spectrum recorded in the $[1\overline{1}0]$ azimuth but not the off-specular spectrum recorded in the [001] azimuth. Further investigation of this effect led to the discovery that this off-specular enhancement of this mode was strongly dependent on the incident electron energy, as shown in Fig. 6.14, which shows the incident electron energy dependence of the intensity of the $v_s(COO)$ loss, normalised to that of the $\delta(COO)$ loss, for both off-specular and specular spectra. While the spectra recorded in the specular geometry show an energy dependence fully consistent with the prediction for dipole excitation, the off-specular data show a strong enhancement, peaking at \sim 14 eV.

This effect is a manifestation of a third excitation mechanism, so-called resonance scattering, in which the excitation of the vibrational mode is strongly enhanced by the creation of a negative ion resonance at a particular excitation energy. The transient negative ion state leads to a similarly transient modification of the molecular geometry (in the present case of the C–O bond lengths) and thus the strong excitation of an internal vibrational mode. These negative ion resonances are well known in the gas-phase scattering of electrons from molecules,

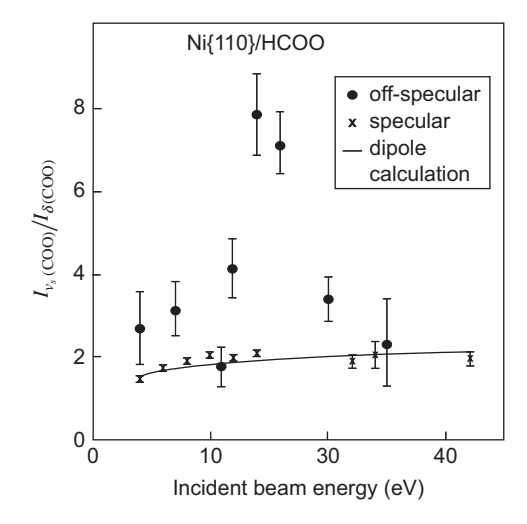


Fig. 6.14 Incident electron energy dependence of the excitation of the $v_s(COO)$ loss, normalised to that of the $\delta(COO)$ loss, for formate (HCOO) on Ni{110}, measured in specular and off-specular geometries. Also shown is the predicted energy dependence for dipole excitation. Reprinted with permission from Jones *et al.* (1989). Copyright 1989, AIP Publishing LLC.

and their effects in adsorbed molecules were reviewed by Palmer and Rous (1992). In the case of the Ni{110}–formate system Jones and Richardson (1988) argued that the resonance seen in Fig. 6.14 corresponds to the σ -symmetry-shape resonance seen in NEXAFS from adsorbed formate shown in Fig. 3.55 (in which a core electron is excited into this scattering resonance state). They further proposed that the observed angular dependence in HREELS can be related to the conditions for optimal excitation of this shape resonance. Notice that the width of the resonance in Fig. 6.14 would imply a lifetime for the resonant ion state of $\sim 10^{-14}$ s.

Evidently the techniques of RAIRS and HREELS offer significant complementary benefits. Both techniques allow one to obtain spectra dominated by dipole selection rules, but HREELS offers the possibility to also detect modes that are not dipole active and to vary the experimental conditions to separate these two modes. The HREELS technique allows one to cover a wide range of vibrational energies including those below ~125 meV (~1000 cm⁻¹), typically corresponding to molecule–substrate vibrations, which becomes increasingly difficult in standard RAIRS studies owing to the problem of finding suitable transparent windows (although these far-IR studies have been successfully pursued in a window-less fashion using synchrotron radiation). However, HREELS is intrinsically a UHV technique whereas RAIRS studies can be conducted in relatively high ambient gas pressures, which is especially relevant to studies of surface catalytic reactions. Moreover, the spectral resolution achievable in RAIRS is substantially higher than

in HREELS. In RAIRS it is common to operate with a resolution of 1–2 cm⁻¹ (although the actual peak widths may be as much as an order of magnitude larger, as discussed above). By contrast, most HREEL spectra have been recorded with spectral resolutions of only ~10 meV (~80 cm⁻¹) or worse. Building HREELS instruments capable of much higher resolution is challenging, but Ibach and coworkers achieved a resolution of ~1 meV (~8 cm⁻¹); the book by Ibach (1991) addressed the many issues associated with such advanced instrumental designs.

6.1.4 Other Optical Probes of Surface Vibrations

An alternative optical probe of molecular vibrations that is extensively used in the study of molecular systems is Raman spectroscopy. This technique involves the inelastic scattering of photons, typically derived from a laser operating in or close to the visible optical range, in which the inelastically scattered photons have energies equal to that of the original photon plus or minus a rotational or vibrational energy of the scattering centre. The lower energy scattered radiation, corresponding to a vibrational energy loss, is referred to as Stokes radiation, while the higher energy scattered radiation, in which a vibrational energy gain has occurred, is referred to as anti-Stokes radiation. The technique involves somewhat different selection rules from those of conventional infrared spectroscopy, notably being dependent on the polarisability, rather than the dynamic dipole moment, of the molecule. Because the effect is relatively weak, however, conventional Raman spectroscopy from submonolayer coverages of molecules on single-crystal (flat) surfaces is not a generally viable method. However, on certain surfaces, particularly rough or nano-structured surfaces of Ag and Au, huge enhancements (exceeding the cross-sections in conventional gas-phase spectra by many orders of magnitude) of the Raman signal have been observed, leading to a technique referred to as surface-enhanced Raman spectroscopy (SERS) (e.g. Stiles et al., 2008). Although some aspects of the underlying theory continue to be debated several decades after the first observation of the effect by Fleischmann et al. (1974), it is generally accepted that a key factor is excitation by the incident radiation of surface plasmon modes in the near-surface region of the support, leading to a strong enhancement of the local electric field. This enhancement, however, relies on the plasmon oscillations having a component perpendicular to the surface, a requirement that accounts for the need to have a rough surface or a nanoparticulate structure. Coincidentally, it is surface roughening, often induced in electrochemical cells, that appears to account for the common observation of SERS at electrochemical electrode interfaces. The resulting huge enhancements of the Raman spectra have led to SERS being widely exploited to perform the routine spectroscopy of molecular systems, using nanostructured substrates typically involving Ag or Au or, for example, nanoparticles of gold embedded in filter paper. The technique is claimed to be capable of detecting single molecules in some cases. However, although it relies on a surface phenomenon, studies of molecular adsorbates on flat single-crystal surfaces do not show these large enhancements, so SERS cannot be used routinely for the vibrational spectroscopy of such surfaces.

Quite different optical probes of surfaces are provided by two non-linear processes, namely sum frequency generation (SFG), in which simultaneous illumination by two different frequencies of light, ω_1 and ω_2 , can lead to the emission of light at frequency $\omega_{\rm sfg} = \omega_1 + \omega_2$ and second-harmonic generation (SHG), effectively the same process but with the two incident light frequencies the same. A key property of both processes is that they can occur only under the electric-dipole approximation at sites that lack inversion symmetry. As the bulk structures of most crystalline solids do possess inversion symmetry (a notable exception is III-V semiconductors with the zinc blende structure, such as GaAs), these non-linear processes do not occur in most bulk solids but they can occur at the free surface of such materials or at interfaces between them, where the inversion symmetry is lost. This lack of inversion symmetry thus renders the techniques surface (or interface) specific.

Both techniques have been used in surface studies, but while the SHG signal does provide a surface-specific signal that changes when changes occur at a surface, the information regarding the particular nature of these changes is very limited. By contrast SFG, using a fixed visible light beam and a variable-frequency infrared beam, does offer the ability to detect surface vibrational modes, the SFH signal being enhanced when the IR beam is in resonance with a surface vibrational mode. Notice that the SFG process involves both energy conservation and also momentum conservation parallel to the surface, so the direction of the emitted SFG radiation is determined by the condition

$$\mathbf{k}_{\text{sfg}}^{\parallel} = \mathbf{k}_1^{\parallel} + \mathbf{k}_2^{\parallel} \tag{6.16}$$

The fact that the emitted direction of the SFG radiation differs from that of the specularly reflected incident radiation is important, as it somewhat simplifies the detection of this weak signal in the presence of the intense reflected incident radiation. Generating a significant SF signal requires the use of intense incident radiation and it can be shown that the output is proportional to $1/\delta t$, where δt is the laser pulse width. Short (ns or ps) or ultrashort (fs) pulses are therefore favoured. Typically the IR laser pulse is achieved through down-conversion of the part of the high-power visible pump laser that is typically restricted to wavelengths of ~2–10 μ m (i.e. ~5000–1000 cm⁻¹). Longer-wavelength (lower-vibrational-energy)

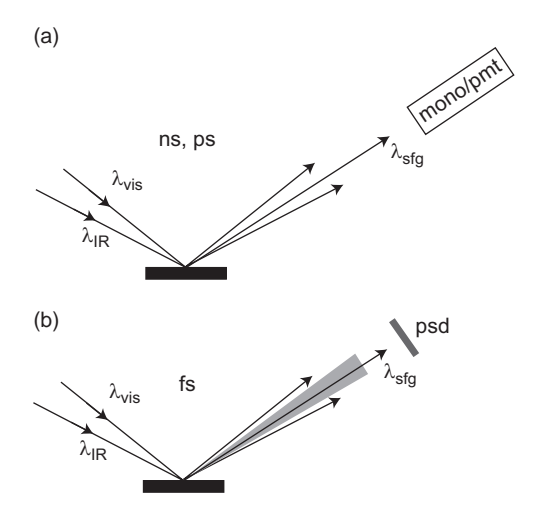


Fig. 6.15 Schematic diagram showing the different SFG detection schemes used with (a) incident IR radiation pulses (scanned through the spectral range of interest) on the ps-to-ns length scale corresponding to a spectral width of $< \sim 10~{\rm cm}^{-1}$ and (b) fs incident pulses of fixed wavelength, having a much larger spectral width.

experiments are generally not possible with 'table top' systems but can be performed through the use of IR free-electron lasers (FELs). Of course, the duration of the IR laser pulse has some bearing on the bandwidth and thus the associated resolution. A bandwidth for ns pulses of less than ~1 cm⁻¹ increases to ~20 cm⁻¹ for ps pulses and to ~100 cm⁻¹ for 100 fs pulses. Utilisation of these shortest pulses leads to a different detection strategy. The SFG emission from the longer pulses is detected sequentially using a filter monochromator (spectrometer) and photomultiplier, scanning the IR laser wavelength (Fig. 6.15(a)). However, with the shortest pulses one can use a fixed central wavelength of the IR laser in the energy range of interest, and exploit the fact that the emitted SFG radiation is intrinsically dispersed (according to equation 6.16), to use parallel detection of the different emitted wavelengths by a position-sensitive detector (Fig. 6.15(b)).

An example of SFG data collected from a Pt{111} surface at room temperature exposed to different doses of CO exposure under UHV conditions, measured with the method shown schematically in Fig. 6.15(a) in the spectral range around the atop C–O stretching mode, taken from a study by Klünker *et al.* (1996) is shown in Fig. 6.16. In these experiments an IR laser with pulse length ~20 ps and spectral width ~6 cm⁻¹ was used, while the visible radiation at 5320 Å was provided from laser pulses of duration ~22 ps. The SFG spectra of Fig. 6.16 clearly show the same C–O stretching mode of atop-bonded CO as those in the RAIRS spectra of Fig. 6.7 on Pt{100}, while the upward frequency shift with increasing coverage is

consistent with the expected qualitative behaviour due to dynamic dipole coupling, as seen in the C–O stretching mode of the bridging CO on Ni{111} in Fig. 6.6. These spectra, however, did not show the expected weaker stretching mode associated with the partial occupation of bridging sites, previously seen in both RAIRS and HREELS (and also seen on Pt{100} (Fig. 6.7)). The SFG spectra recorded at a lower sample temperature, 150 K, *did* show this band, however. Klünker *et al.* attributed this effect to the very strong intrinsic broadening of the bridging band previously measured in RAIRS (Schweizer & Rettner, 1989), the increase being from 7.7 cm⁻¹ at 150 K to 37 cm⁻¹ at 300 K. The difficulty of observing this band in SFG can then be understood as due to the fact that the SFG signal depends inversely on the linewidth Γ .

Specifically, the SFG signal intensity can be written as

$$I_{\rm sfg} \propto \left| \chi_{\rm s}^{(2)} \right|^2 \tag{6.17}$$

where $\chi_s^{(2)}$ is the non-linear surface susceptibility, which is itself a sum of non-resonant (NR) and resonant (R) contributions:

$$\chi_{\rm S}^{(2)} = \chi_{\rm NR}^{(2)} + \chi_{\rm R}^{(2)} \tag{6.18}$$

the resonant term having the form

$$\chi_{\rm R}^{(2)} = \sum_{n} \frac{A_n}{\omega_{\rm IR} - \omega_n + i\Gamma_n} \tag{6.19}$$

with A_n the amplitude of the *n*th resonance at frequency ω_n . An increase in Γ_n by a factor 4.8 thus leads to a reduction in the SFG signal of more than one order of magnitude, sufficient to render it undetectable in these experiments.

Of course, the real benefit of the SFG technique as a means of detecting surface and interface vibrational modes is not in pure UHV experiments, for which simpler techniques are available, but in situations where the traditional UHV methods cannot be applied. In general, photon-in photon-out experiments offer the ability to study surfaces under high ambient gas pressures or, indeed, under a liquid or another solid. In the context of the surface science discussed in this book the most obvious advantage is that it can be used to study surfaces under higher pressures of reactive gases, providing a bridge of the 'pressure gap' between studies at 'high' pressures and at UHV conditions, which are found, at least in some cases, to expose quite different surface chemistry. Of course RAIRS also offers the possibility to study surfaces under higher gas pressures, although in some cases IR absorption in the reaction gases can prove to be a limitation. One demonstration of the potential of SFG to bridge this gap up to pressures of 200 mbar, using a high-pressure cell within a standard UHV surface science chamber, was provided

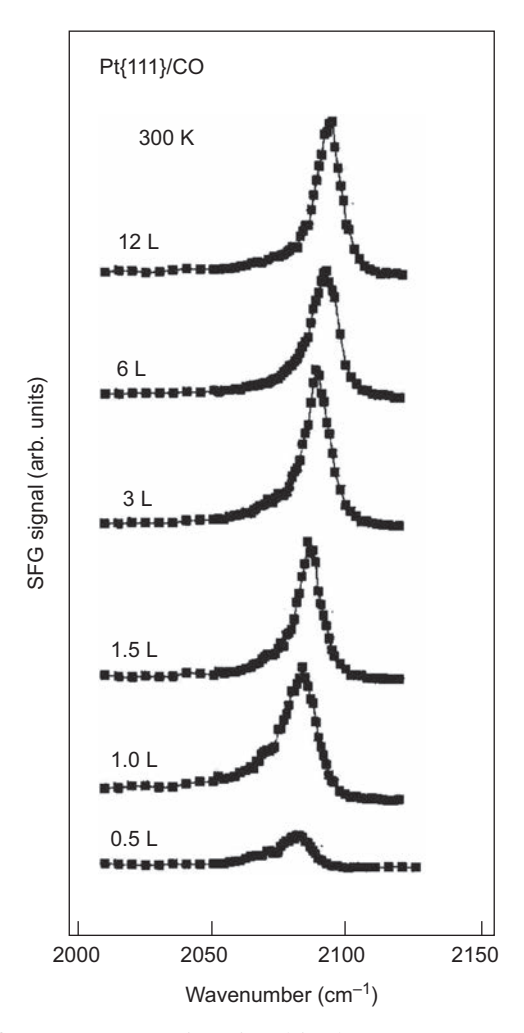


Fig. 6.16 Sum frequency generation signal in the energy range of the atop C–O stretching frequency recorded from a Pt{111} surface at room temperature. Reprinted from Klünker *et al.* (1996), copyright 1996, with permission from Elsevier.

by Rupprechter *et al.* (2001), who investigated the interaction of CO with Pt{111} and Ni{100} surfaces over this pressure range. However, some indication of the weakness of the SFG signal was also given by this study, the authors noting that incident pulses of 10^{14} – 10^{15} photons (using visible and IR pulses of 2 mJ and $10~\mu J$, respectively) yielded only 'a few counts' in the SFG signal.

A more recent example of the application of SFG to investigate an adsorbate surface under UHV conditions by Gladh *et al.* (2015) exploited the alternative mode of data collection shown schematically in Fig. 6.17. Specifically, 50 fs

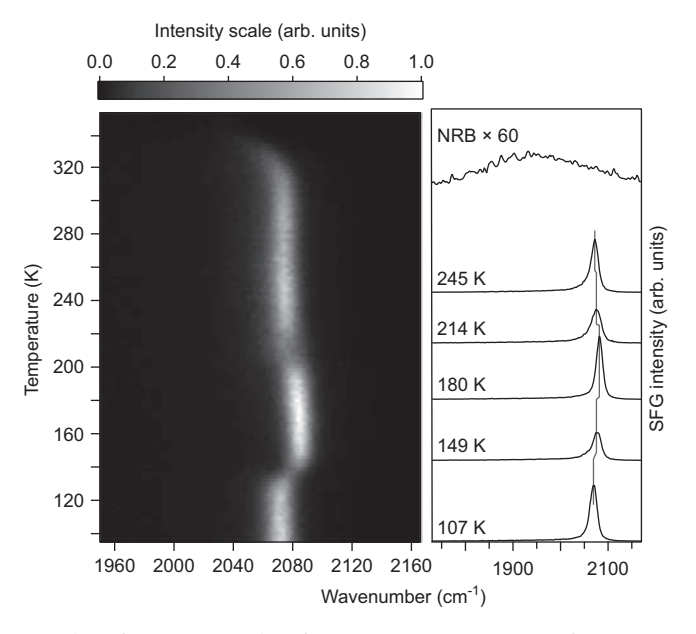


Fig. 6.17 Results of an SFG study of a $Ru(0001)(2\times1)$ -O surface exposed to CO and subsequently heated to successively higher temperatures. The spectra show the C–O stretching mode associated with the CO adsorbed in atop sites. On the left is shown a map of the complete set of spectra with intensity represented on a linear grey scale (courtesy of Henrick Öström). On the right, a subset of the data is shown as conventional spectra. Adapted from Gladh *et al.* (2015).

pulses of IR radiation were used centred on 2000 cm⁻¹ (5 µm wavelength) with a bandwidth of ~250 cm⁻¹, the signal being detected with a spectrograph fitted with an intensity-amplified CCD camera. This arrangement was used to study the evolution of the C-O stretching frequency band for atop CO adsorbed on an $Ru(0001)(2\times1)$ —O surface as the sample was heated from 107 K to above room temperature. The resulting experimental spectra are shown in Fig. 6.17. On the left, the many spectra, recorded continuously during heating, are shown with the intensity represented on a linear grey-scale map. On the right a subset of these data is shown in a more conventional spectral mode, together with the (weak) nonresonant background (the broad peak reflecting the energy spectrum of the incident IR pulses). A striking feature of the results is that, while the C-O stretching frequency clearly shifts during the heating cycle, these shifts include discontinuous changes where the SFG intensity falls sharply. These discontinuities are attributed to structural transitions in the overlayer, and in particular to the switching of the CO between different states. In the transition regions there is partial coverage of CO in the different states and the drop in SFG intensity can be understood through the form of equation (6.17), namely that the intensity depends on the square of the

non-linear surface sensitivity, which itself depends linearly on the coverage in each state. In contrast with what would be seen in RAIRS, the SFG signal very clearly distinguishes between a continuous shift of frequency in a narrow temperature range and a discontinuous change in frequency associated with a structural transition. A more complete discussion of these data and the theoretical treatment, including the role of adsorbate—adsorbate coupling, is given in the original publication of Gladh *et al.*

Of course, while these examples of CO adsorption on a single-crystal metal surface provide a good basis for comparison with the RAIRS and HREELS techniques, it is important to stress, as mentioned above, that even for studies of molecules on free surfaces it is the ability of SFG to be applied at higher ambient pressures (and not only to CO!) that is its greatest strength. One example of such a study is that of the photocatalysis of methanol over TiO₂ thin films, at total gas pressures in the 100 mbar range, by Feng *et al.* (2015).

6.1.5 STM and Inelastic Electron Tunnelling Spectroscopy

A rather different technique for studying the vibrational modes of adsorbed molecules that offers some exceptional advantages, but is far less routine in its application, is inelastic electron tunnelling spectroscopy (IETS) in STM. The original IETS technique, based on tunnelling through thin film structures, predates STM by almost 20 years and was first discovered in studies of a metal-oxide-metal junction by Jaklevic & Lambe (1966), the tunnelling spectra showing features due to excitation of the vibrational modes of adsorbed molecules within the junction. The method has subsequently been used extensively to study other conductorinsulator-conductor samples with thin molecular films 'sandwiched' in the structure (e.g. Walmsley & Tomlin, 1985). The upper part of Fig. 6.18 shows a schematic diagram of the tunnelling process for both elastic and inelastic events, while below are shown the consequences of the inelastic loss of energy $\hbar\omega$ on the tunnelling current I and its first and second derivative with respect to the voltage difference V. In the standard IETS experiments the tunnelling barrier occurs due to the presence of the oxide (and adsorbed molecular) layer, but essentially the same diagram applies if the barrier is associated with a vacuum gap. Indeed, this diagram is very similar to that used to describe the STS process in Chapter 5; however, the much weaker change in the tunnelling current associated with the inelastic loss means that to detect the effect it is necessary to measure not simply the conductance G (which equals dI/dV) but also the derivative of the conductance, dG/dV (or d^2I/dV^2). Of course, if IETS is conducted using a scanning tunnelling microscope then the special advantage of this method is that the vibrational spectrum obtained is spatially resolved (with atomic-scale resolution). This technique was pioneered

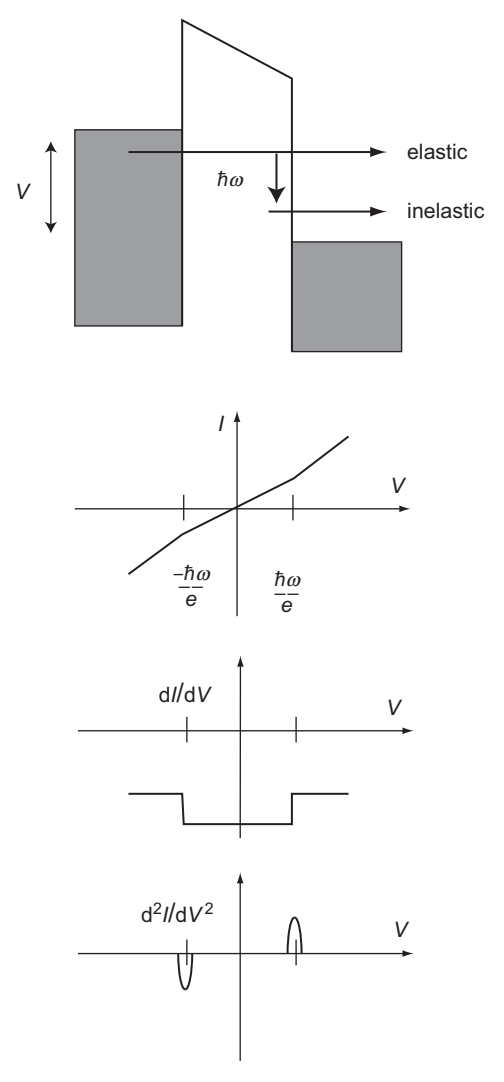


Fig. 6.18 Schematic diagram of the IETS process and the associated dependences of the tunnelling current I and of dI/dV and d^2I/dV^2 on the tunnelling voltage V.

by the group of Wilson Ho, who reported the first results in a study of acetylene (C_2H_2) adsorbed on $Cu\{100\}$ (Stipe *et al.*, 1998).

Figure 6.19 shows a composite of results from these early experiments by Ho and his colleagues including some for partially and completely deuterated acetylene. In this figure are shown conventional constant-current STM images of the three different molecular species adsorbed on Cu{100}. As might be expected, it can be deduced that the images are uninfluenced by partial or complete deuteration, as the electronic structures of the three different isotopes are essentially

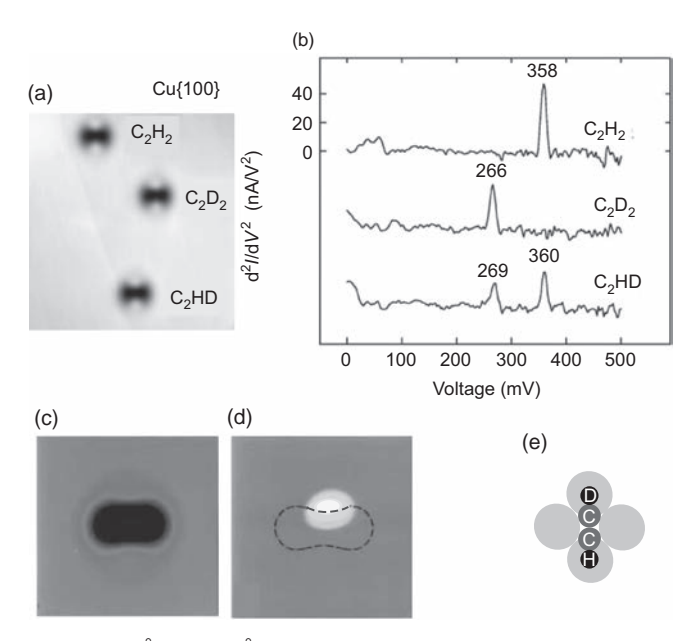


Fig. 6.19 (a) A 52 Å \times 56 Å constant-current STM image of three different acetylene isotopes adsorbed on Cu{100}. (b) STM-IET spectra obtained with the tip centred over each of these molecules. Panels (c) and (d) show 17 Å \times 17 Å images of the C₂HD species in conventional constant-current STM and in differential conductance at 269 meV. Panel (e) is a schematic diagram showing the molecular orientation, the grey shading indicating schematically the electronic orbitals. Reprinted with permission from Stipe *et al.* (1999). Copyright 1999 by the American Physical Society. Note that the original images of (c) and (d) were presented in calibrated false-colour mode; the conversion of monochrome leads to a non-linear scale and (d) has been arbitrarily modified to reflect the qualitative features of the colour original.

identical. The IET spectra obtained by localising the tip above the three different isotopes are shown in Fig. 6.19(b); above C₂H₂ the spectrum shows a clear peak corresponding to the C–H stretching mode at an associated energy of 358 meV, while above C₂D₂ a peak due to the C–D stretching mode at 266 meV is seen. Above, C₂HD peaks due to both the C–H and C–D stretching modes are seen, with small upward energy shifts. Evidently the STM-IETS data show single-bond sensitivity in the detected vibrational modes. The IET spectra were obtained by placing the tip over the centre of each molecule at a constant vertical position and applying an rms modulation voltage of 5 mV at 200 Hz as the bias voltage was scanned. Each spectrum shows the average of 16 scans, each lasting 2 min.

In Fig. 6.19(c) is shown an enlarged conventional STM image of the C_2HD molecule, while Fig. 6.19(d) shows a differential conductance image, recorded at the same time at a bias voltage of 269 mV (the voltage of the C–D stretching mode

vibrational excitation). The broken line in (d) corresponds to the outer contour of the conventional STM image and the strong enhancement of the C–D energy loss is found to be localised above the C–D bond. Figure 6.19(e) shows schematically the associated orientation of the C_2HD molecule in these images.

One obvious question that arises in understanding and applying the STM-IETS technique as a probe of the vibrational properties of adsorbed molecules is, what are the selection rules? Does one excite only, or preferentially, modes with dynamic dipole moments perpendicular to the (metal) surface, as in RAIRS, or can one excite other modes, as in the impact mode of HREELS? One might reasonably expect that the local electron interaction means that the situation is more similar to HREELS than to the far-field interaction of RAIRS. In conventional IETS it seems to be established that both IR and Raman-active vibrational modes can be detected, together with some modes that are forbidden in both these techniques although overtone and combination modes are generally weak. In effect there are no very general selection rules, although 'propensity' rules that may identify the most active modes have been discussed (e.g. Troisi & Ratner, 2006).

The first attempt to develop a theory specific to STM-IETS, and in particular to try to understand why in the Cu{100}/acetylene experiments only the C-H or C-D stretching modes were detected, was by Lorente & Persson (2000). They specifically concluded that the long-range dipole coupling is negligible but extended the s-wave tip-elastic-scattering model of Tersoff & Hamman (1983) to include inelastic scattering. Using this model they calculated relative changes in the tunnelling current associated with excitation of not only the C-H and C-D stretching modes but also the C-C and C-metal stretching modes and the C-H bending mode; while all these modes are predicted to be observable in principle, the predicted conductance changes associated with the C-H and C-D stretching modes are roughly an order of magnitude larger than the other modes, and are thus the only reasonably detectable ones. For this adsorption system, Lorente et al. (2001) did subsequently identify some symmetry propensity rules, specifically showing that the measured signal from adsorbed C₂D₂ is from the antisymmetric stretching mode. These calculations also revealed that in some cases partial cancellation between inelastic and elastic contributions to the tunnelling current may mean that some modes are not detected. Other more subtle system-specific effects, such as those in atomic hydrogen adsorption on Cu{100}, have also been identified (Paavilainen & Persson, 2006). A review of the theoretical approaches to the STM-IETS technique is included in the paper by Morgenstern et al. (2013), although attempts to gain a broader understanding of which vibrational modes may be detected in which molecular systems are continuing; for example, a theoretical study of STM-IETS of the formate (HCOO-) and benzoate (C₆H₅COO-) species on Cu{111} identifies just one (C-H stretching) detectable mode in formate but none in benzoate, the difference being attributed

to the spatial extension of the tunnelling-active electronic states away from the interface atoms (Burema *et al.*, 2012). This appears to extend the previously identified initial criterion that the symmetry of the molecular orbital into which the tunnelling electron first enters determines which vibrational modes may potentially be excited (Kawai *et al.*, 2004).

The ability to probe the adsorption and reaction properties of single adsorbed molecules using internal spectroscopic, as well as imaging, capabilities demonstrated by these early experiments clearly opens up the potential for a wide range of elegant surface science experiments to probe these properties, and a few of the resulting applications were reviewed by Ho (2002). However, it is important to recognise that these are challenging experiments. The very small tunnelling-conductance changes that must be detected and the need for extreme image stability require very low levels of electronic and vibrational noise in the instrumentation as well as low temperatures (generally less than 10 K). Most of the pioneering experiments have been performed using purpose-built (rather than commercial 'off-the-shelf') instruments.

One important feature of the ability to selectively excite specific vibrational modes in isolated molecules is not only that this provides a means to identify and characterise the adsorbed molecule but also that the excitation of vibrational modes can trigger modifications and reactions. In the case of adsorbed acetylene, for example, exciting the C-H and C-H vibrations can trigger azimuthal rotation of the adsorbed molecule, and indeed the most detailed results from this system, which required a stable static molecule, were obtained from the (more massive) deuterated species for which the probability of exciting this rotation is lower. As such, these tunnelling excitations underpin many aspects of atomic and molecular manipulation in STM (e.g. Morgenstern et al., 2013). Some examples of atomic and molecular manipulation, including the triggering of molecule formation by bringing reactive fragments together, have already been presented in Chapter 4 (section 4.1.3). Some further examples of vibrationally mediated surface chemical transformations in STM, referred to by Kawai and coworkers as 'action spectroscopy', may be found in the review by Kim et al. (2015).

6.1.6 Inelastic Helium Scattering

A very different way in which surface vibrational information may be obtained is through the study of the inelastic scattering of atoms or molecules, most commonly helium atoms, at a surface. The HAS technique using the elastic scattering (diffraction) of helium atoms from surfaces to investigate surface structure has already been described in Chapter 3 (section 3.1.6.1). The inelastic HAS (iHAS)

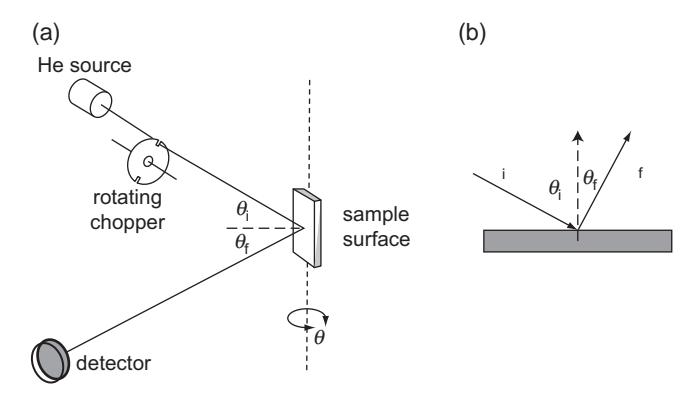


Fig. 6.20 (a) Schematic diagram showing the main components of an inelastic atom scattering experiment. (b) The associated wavevector diagram.

experiment is closely similar, but in this case the energy of the scattered atoms is analysed using a time-of-flight detector. The basic arrangement of the experiment is shown in Fig. 6.20(a) and comprises a He atom beam source (as used in HAS), a rotating chopper to pulse the beam and a detector at the end of a flight tube. A key requirement, of course, is that the initial beam is highly monoenergetic and with the use of supersonic nozzles one can, for example, achieve an energy spread of ~0.1 meV in a beam with an average energy in the range ~8–120 meV rather routinely, while far higher resolution (below 1 μ eV) can also be obtained in some instruments. Notice, of course, that the largest energy loss detectable is set by this primary beam energy, so in general this technique is focussed on low energy losses (much smaller than, for example, the C–O or C–H stretching frequencies described in some examples in the previous sections).

Figure 6.20(b) shows the wavevectors of the incident and scattered He atoms, and the conservation of energy and momentum require that the frequency ω of a detected vibrational loss is given by

$$\hbar\omega = \frac{\hbar^2}{2m} \left(k_{\rm i}^2 - k_{\rm f}^2 \right) \tag{6.20}$$

while the associated (surface phonon) momentum is

$$\Delta \mathbf{k} = \mathbf{k}_{\text{f}||} - \mathbf{k}_{\text{i}||} = k_{\text{f}} \sin \theta_{\text{f}} - k_{\text{i}} \sin \theta_{\text{i}}$$
 (6.21)

Because the instrumentation – notably the He source and the time-of-flight detector – are physically large, these experiments are conducted using a fixed angle between the incident and scattered beams; however, by rotating the crystal the incidence (and detection) angles can be changed in order to explore different surface phonon momenta.

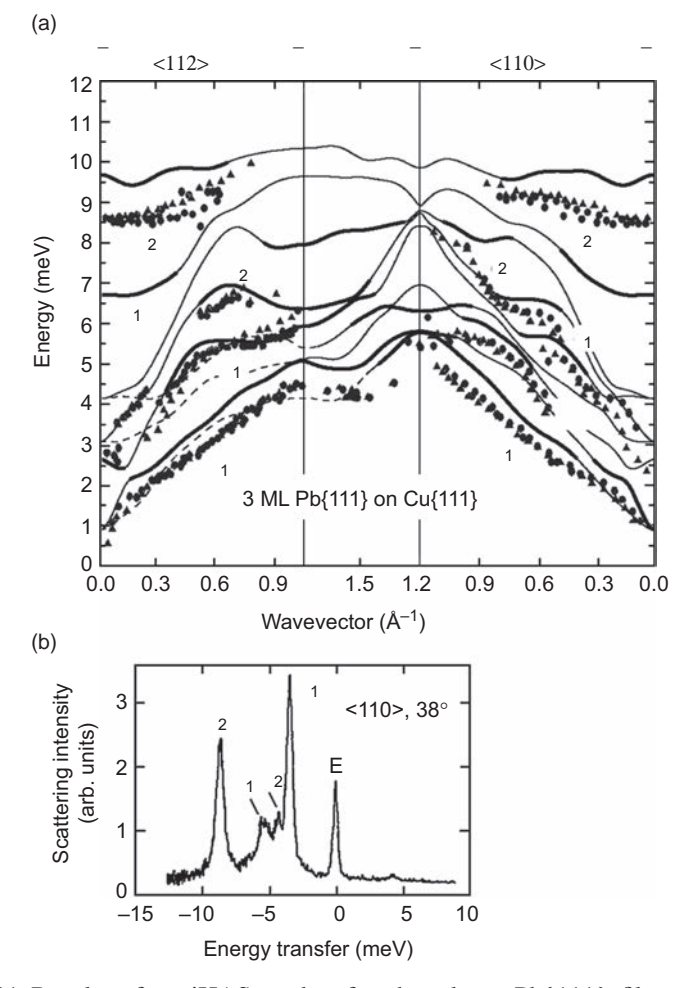


Fig. 6.21 Results of an iHAS study of a three-layer Pb{111} film grown on Cu{111}. Panel (a) shows the theoretically predicted phonon bands as full lines with the experimental data points superimposed. Panel (b) shows a representative iHAS time-of-flight spectrum for one specific geometry. The labelling of the individual bands is explained in the original publication. After Benedek *et al.* (2014), reproduced with permission from the PCCP Owner Societies.

Evidently the significant strength of this technique is its ability to map surface phonon bands, a capability not shared by most other vibrational techniques described in the foregoing sections (although such measurements are possible and have been undertaken using HREELS by exploring the angular distribution of the loss spectra).

As an example of the application of the iHAS technique, Fig. 6.21 shows some results taken from an investigation of ultrathin epitaxial Pb{111} films grown on Cu{111} by Benedek *et al.* (2014). Figure 6.21(b) shows an individual

time-of-flight spectrum in one particular scattering geometry; in addition to the elastic peak (labelled E) are several loss peaks associated with the excitation of different phonon modes in the film. Notice that the TOF spectrum also shows a weak peak at energy gain ~4 meV, which is also associated with coupling to the α_1 phonon (such energy gain peaks can be more prominent in some cases). Figure 6.21 (a) shows the result of transferring the energies and Δk values of the peaks in spectra recorded in many different geometries onto a phonon band structure, together with the results of theoretical calculations of these bands. Evidently the iHAS technique can lead to a rich source of surface phonon band information. Of course, in general one expects to see only surface phonons in iHAS spectra, and the coupling to a range of subsurface phonons in the multilayer film is, at first sight, surprising. Indeed, in standard elastic HAS the technique is generally regarded as having extreme surface specificity, detecting the properties of the electronic corrugation outside the surface. However, the authors of this iHAS study concluded that the quasi two-dimensional electron gas of the metal film can transmit the extremely small mechanical vibrations in the subsurface layers to the surface, where they can be detected in iHAS. The related theoretical calculations indicate that this coupling of the impinging He atoms to the subsurface phonon modes is due to the electron-phonon interaction, the intensity of the loss peaks being related to the strength of the electron-phonon coupling of the individual modes. The particular interest in electron-phonon coupling in Pb films arises from the fact that Pb is a superconductor.

Within the context of using vibrational spectroscopy to identify molecular adsorbates on surfaces, iHAS is not strictly relevant, of course, because this type of spectral fingerprinting depends on detection of the internal vibrational modes of molecules that have energies much higher than the typical impact energies (< ~20 meV) of the helium atoms in iHAS. Low energy vibrational modes of adsorbed molecules do exist, however, and are related to the movement of the molecule relative to the surface – frustrated translational and rotational modes. These can be roughly characterised as stretching (S) modes and translational (T) modes. The molecule-surface stretching modes are, of course, characteristic of the nature and geometry of the molecule-surface bonding but are also generally too high in energy to be detectable with iHAS; coincidentally, they are also generally too low in energy to be detected in standard RAIRS experiments because the windows used in such experiments generally are not transparent in the far-IR spectral range. These S modes are most commonly detected in HREELS. The very low energy T modes, however, are accessible to iHAS and are often difficult to detect by other methods. In principle, they can be detected in HREELS, but only with very high resolution instruments that offer the possibility of detecting loss peaks only a few meV from the (very much larger) elastic peak. For example, typical energies

of T-mode vibrations, of adsorbed CO molecules parallel to the surface, in the energy range ~3-8 meV have been detected using iHAS on a range of different metal surfaces; measurements of this kind were reviewed by Graham (2003). Of course, an ordered adsorbate layer gives rise to well-defined dispersion of these vibrational modes, which can be measured using iHAS. For example, this was seen in CO adsorbed on Cu{100} (Ellis et al., 1995) but also more recently for the methyl species (CH₃ and also CD₃) on Si{111}) by Brown et al. (2014). Insofar as the T modes of adsorbate atoms and molecules are frustrated translational modes, they provide some information on the potential wells in which the atoms or molecules are trapped and thus on the shape of the bottom of the barrier to surface diffusion. However, more explicit information on surface diffusion is also available through the iHAS technique in the energy broadening of the scattered He atoms. This technique, generally referred to as quasi-elastic (QE) HAS by analogy with quasi-elastic neutron scattering, was first demonstrated by Frenken et al. (1988) in a study of the Pb{110} surface, and a number of measurements of adsorbate diffusion rates and associated energy barriers were reviewed by Graham (2003).

6.2 Electronic Spectroscopies

As discussed in the previous sections, vibrational spectroscopies provide a valuable spectral fingerprint of molecular character. Although somewhat less rich in the number of spectral features in the detected energy range, valence-electron spectroscopies also offer a means to identify and characterise adsorbed molecules through their molecular orbital energy levels. Indeed, core-level spectroscopy also provides some spectral fingerprinting. In particular, XPS 'chemical shifts' of atoms of the same element located in different functional groups, discussed in section 5.5.1.2, can provide an indication of molecular character. The early characterisation of C 1s photoelectron binding energies in different molecules by Shirley (1973), shown in Fig. 5.27, illustrates this effect very clearly. Valence-electron spectroscopy, however, provides a more direct measure of the molecular character of an adsorbate.

The technique of ultraviolet photoelectron spectroscopy (UPS) has already been described in section 5.1, together with examples of its use in the study of clean solid surfaces, particularly in its angle-resolved (ARPES) mode. The technique allows one to determine the binding energies of the occupied valence-energy levels that give rise to characteristic peaks in the emitted energy spectrum, while ARPES allows one to map the associated valence-band structure. In the same way, if a molecule is adsorbed onto a surface, the UPS spectrum shows additional peaks that are characteristic of the molecular orbital energies.

An early investigation by Demuth & Eastman (1974), shown in Fig. 6.22, illustrates this approach rather clearly. The experiment was designed to investigate the adsorption of benzene (C_6H_6) on a Ni{111} surface. In the uppermost panel of the figure is shown the UP spectrum obtained from the clean Ni{111} surface using He I (hv = 212.2 eV) incident radiation and also from this same surface after an exposure of 3.2×10^{-6} mbar per second of benzene at room temperature. Evidently the adsorbed benzene leads to new peaks in the UP spectrum and, in the second panel, a difference spectrum is shown that highlights these changes: namely, increased emission associated with photoemission from occupied orbitals of the adsorbed molecule together with some attenuation of the main peaks in the clean Ni{111} spectrum close to the Fermi level, corresponding to emission from

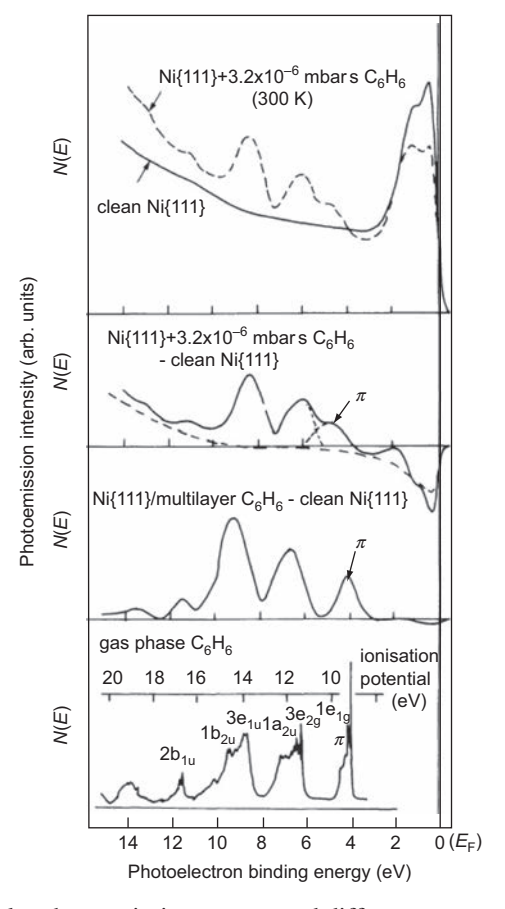


Fig. 6.22 Ultraviolet photoemission spectra and difference spectra from gas-phase benzene and benzene adsorbed on Ni{111} in monolayer and multilayer amounts. Reprinted with permission from Demuth & Eastman (1974). Copyright 1974 by the American Physical Society.

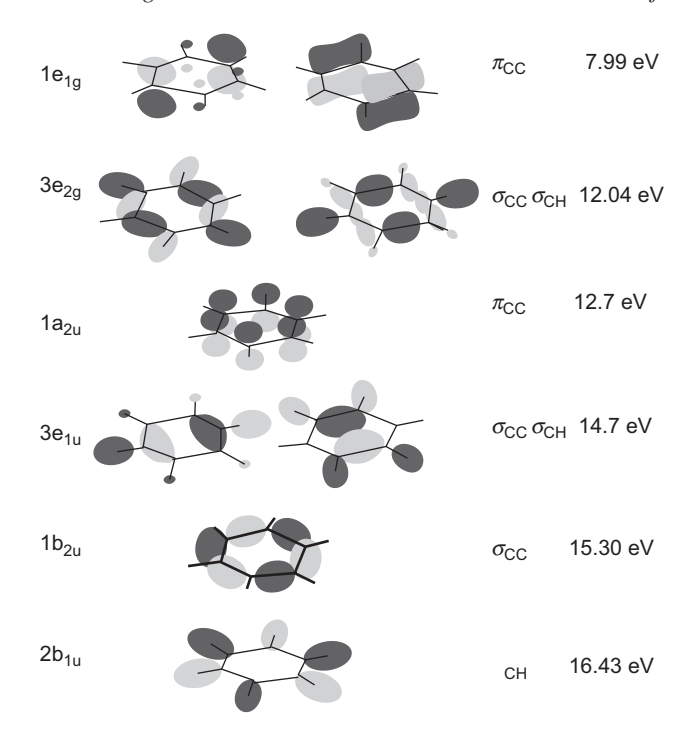


Fig. 6.23 Schematic diagram of the highest occupied orbitals of the benzene molecule. The dark and light shadings correspond to wavefunctions of opposite phase. Also shown are the occupation and symmetry assignments of these orbitals, simplified assignments indicating the local character of the orbital and the calculated gas-phase ionisation energies according to Jorgensen & Salem (1973).

the Ni 3d band. Below this is shown a similar difference spectrum obtained by subtracting the clean surface UP spectrum from one obtained after deposition of a (condensed) multilayer of benzene on the surface. In the bottom panel of the figure is a similar UP spectrum obtained from gas-phase benzene reported by Turner *et al.* (1970). Notice that the gas-phase spectrum shows much higher intrinsic spectral resolution and includes fine structure associated with vibrational excitations, but the main peaks are labelled according to the contributing orbitals.

The spatial distribution of these orbitals is indicated in Fig. 6.23, where they are identified by their full symmetry notation and are also labelled as σ or π according to their local character. Computed gas-phase ionisation energies are also shown as a guide to the approximate energies and ordering. Apart from the obvious difference in spectral resolution there is a clear correspondence of the gas-phase spectrum and the multilayer difference spectrum, after aligning the energy scales to account for the fact that the spectra recorded from the gas phase are referenced to the vacuum level whereas the surface spectra are referenced to the Fermi level. There is also a clear correspondence in the spectra recorded from the benzene

monolayer and multilayer apart from a relative shift in the highest occupied molecular orbital (HOMO) with respect to the other peaks. One may therefore draw two conclusions. Firstly, that the adsorbed species in the monolayer is intact molecular benzene but also that the relative shift of the HOMO indicates that it is this orbital that is primarily involved in the bonding to the surface through hybridisation with the metal valence electrons. In addition, however, the fact that this HOMO is of π symmetry, with the associated electron charge density lying outside the molecular plane, clearly indicates that the molecule must lie essentially flat on the surface. The basic distinction in localisation of σ - and π -orbital states is illustrated in the diagram of some of the benzene orbitals in Fig. 6.23. Evidently benzene is not the simplest of examples but in general a σ -orbital is symmetric about the main plane (or axis) of the molecule, while π -orbitals are antisymmetric about this plane. This antisymmetry implies a node in the wavefunction in this plane and thus antinodes out of the plane. By contrast the σ -states have antinodes in the plane and so possess maximum electron densities in the plane. Bonding of the molecule to the surface through σ -orbitals would therefore imply an end-on configuration for benzene, which would, of course, reduce the symmetry of the molecule and lead to complications due to the loss of degeneracies.

A second system studied by Demuth & Eastman (1974), provided further evidence of the value of UPS for spectral fingerprinting of the character of molecular adsorbates. Specifically, they showed that if ethylene (C_2H_4) was adsorbed on Ni{111} at room temperature then the UP spectrum was very different from that obtained if adsorption was at 100 K but that the room temperature spectrum was identical to that obtained by adsorbing acetylene (C_2H_2) at either 100 K or room temperature. The clear implication, reinforced by comparison of the energies of the spectral peaks with the molecular orbital energies of the two molecules, is that at room temperature (actually at temperatures above ~230 K) ethylene partially dehydrogenates to adsorbed acetylene on Ni{111}, thus providing a direct demonstration of a simple catalytic reaction at the surface.

These two examples illustrate rather vividly the potential power of UPS as a method of studying the adsorption, dissociation and reaction of molecules on surfaces. Nevertheless, some limitations should also be stressed. In the laboratory, UPS is most commonly conducted using He I incident radiation, for which the range of kinetic energies of photoelectrons emitted ($hv - \phi$ where ϕ is the work function) is only ~ 16 eV and, as there is a steeply rising background at low kinetic energies due to inelastic and secondary electrons, only about 10 eV of the spectrum contains useful information. Furthermore, the molecular orbital photoemission peaks typically have widths ~1 eV. The small value of the ratio of the spectral range and the individual peak widths contrasts sharply with the much larger value in vibrational spectroscopies such as RAIRS and HREELS. In UPS, therefore,

these spectral 'fingerprints' can only be recognisable and unique if the number of contributing orbitals is small, implying that the adsorbed molecules themselves must be small, or that there are no more than about two different species, or that both these conditions hold.

A classic example of ambiguities that may arise in identifying the appropriate molecular orbitals in UPS of molecular adsorbates is provided by studies of the adsorption of CO on a range of transition metal surfaces, which triggered some significant debate in the 1970s. This superficially simple system provides a useful example of the additional information that can be exploited in the valence-state photoemission of adsorbed molecules.

Figure 6.24 shows the hybridisation scheme leading to the molecular orbital states of the free CO molecule, together with schematic diagrams of the electron wavefunction distribution of the three shallowest occupied states. Notice that the labelling of the orbitals starts with the much more strongly bound 1σ and 2σ states (not shown), which have predominantly O 1s and C 1s character. The calculated

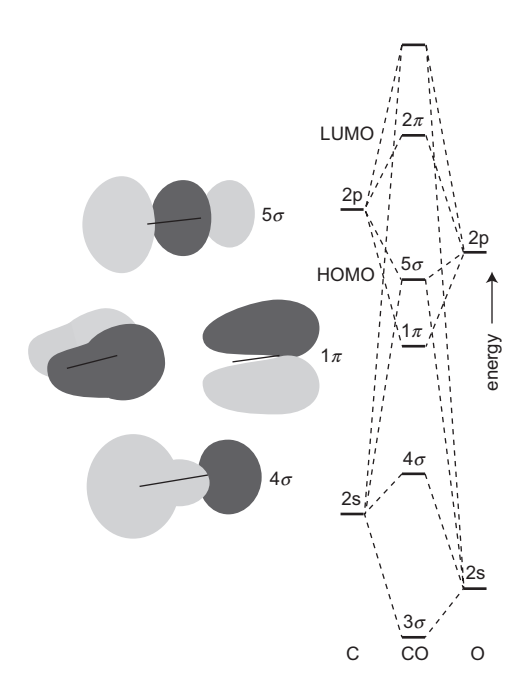


Fig. 6.24 Schematic diagram of the highest occupied orbitals of the CO molecule. The dark and light shadings correspond to wavefunctions of opposite phase. Also shown is a schematic of the hybridisation of the C and O 2p and 2s electrons to form the molecular orbitals. The highest occupied orbital is the 5σ state while the lowest unoccupied orbital is the (antibonding) 2π state. The simplified orbitals and the relative gas-phase ionisation energies are based on the published results of Jorgensen & Salem (1973).

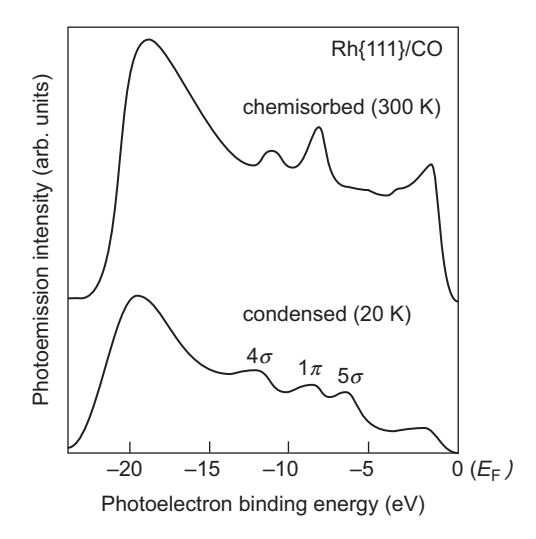


Fig. 6.25 Ultraviolet photon spectra, recorded using synchrotron radiation with hv = 27.5 eV in p-polarisation, from chemisorbed CO on Rh{111} and from a condensed multilayer of CO on the same surface. Adapted from Braun *et al.* (1978).

ionisation potentials of the 5σ , 1π and 4σ orbitals in the gas phase reported by Jorgenson & Salem (1973) are 14.01 eV, 16.91 eV and 19.72 eV respectively, so one would expect these three orbitals to lead to three peaks in the UPS spectrum of CO adsorbed on a metal surface. However, as first shown by Eastman & Cashion (1971) in a study of CO adsorption on Ni films, only two adsorbate-induced peaks are seen. Subsequent studies on a range of single-crystal metal surfaces led to the same result. An example of a later study, of CO adsorption on Rh{111} by Braun *et al.* (1978), which included measurement of the UP spectrum of a condensed layer of CO ~150 Å thickness, is shown in Fig. 6.25. The spectrum from the condensed phase clearly shows the three peaks expected from the isolated CO molecule while only two peaks are seen from the submonolayer chemisorbed phase.

The first convincing evidence of the correct assignment of the two peaks in these CO chemisorption spectra was provided by Gustafsson *et al.* (1975), who compared the photon energy dependence of the spectra (from CO adsorbed on Ni and Pd films) with the photon energy dependence of the three clearly resolved peaks in gas-phase photoemission spectra. They concluded that the molecule bonds to the metal surface through the C atom (as is also found in metal carbonyl molecules) in such a way that the 5σ hybridises strongly with the metal valence electrons and so is shifted down in energy to overlap with the energy of the 1π orbital. The higher kinetic energy peak is thus due to overlap of the 5σ and 1π levels, while the lower kinetic energy peak is from the 4σ orbital. However, the

differing orbital symmetries of these states means that an alternative approach to reaching these assignments is possible.

Specifically, the use of symmetry selection rules has already been outlined in section 5.1 as a means of determining initial band symmetries in studies of photoemission from a substrate band structure. The same methods can be applied to an adsorbed CO molecule provided that the adsorption does not destroy its symmetry properties. The basic idea is most simply illustrated by an 'oriented molecule' approach; i.e. by considering a free CO molecule that has an orientation assumed to be fixed in space by the surface. As illustrated in Fig. 6.24, the occupied molecular orbital states of the CO molecule, which has perfect axial symmetry (point group C_{ϕ}), have either σ (symmetric) or π (antisymmetric) symmetry relative to the molecular axis. Consider the geometry of Fig. 6.26 in which z is defined along the molecular axis, plane-polarised light is incident in the zy plane, characterised by an angle θ_A between the A vector and the z axis. Photoemission is detected in the direction defined by the wavevector **k** with polar and azimuthal angles θ and ϕ . Consider first emission from the σ -states; these are symmetric under reflection in any plane containing the z axis, while if $\theta_A = 90^{\circ}$ (s-polarisation) then the dipole component of the matrix element is antisymmetric about the xz plane. In this plane, therefore, the matrix element for a transition into symmetric final states is zero, so that no σ -emission is seen in this mirror plane, i.e. for any value of θ , if $\phi = 0^{\circ}$. In the case of emission from π -states the symmetry arguments lead to a clear result for emission along the z axis ($\theta = 0^{\circ}$). Specifically, if $\theta_A = 0^{\circ}$ (p-polarisation) then the dipole part of the matrix element is symmetric relative to the emission direction, while the π initial state is antisymmetric, so no emission is seen from such an initial state in this direction. Evidently these considerations provide a simple method of distinguishing emission from initial σ -states and from initial π -states for this simple axial molecule. In the specific case of the two observed emission peaks from adsorbed CO, the lower kinetic energy (higher binding energy) peak is found to vanish if measured in s-polarisation in the xz plane, which is consistent with its assignment to a σ -orbital. The higher kinetic energy (lower binding energy) peak is still present under these conditions but it is also present using p-polarisation in normal emission, consistently with the overlap of the two states, 5σ and 1π , of opposite symmetries. The fact that the energies of these two contributing states are not identical, however, does mean that in the s-polarisation geometry, which suppresses emission from the 5σ orbital, the peak shows a small energy shift because only the 1π contribution is visible in this geometry.

In fact further information on molecular orientation can be obtained by a quantitative determination of the angular dependence of photoemission from different molecular orbitals in an oriented molecule. This angular variation can arise purely from initial-state effects, being a consequence of the fact that the

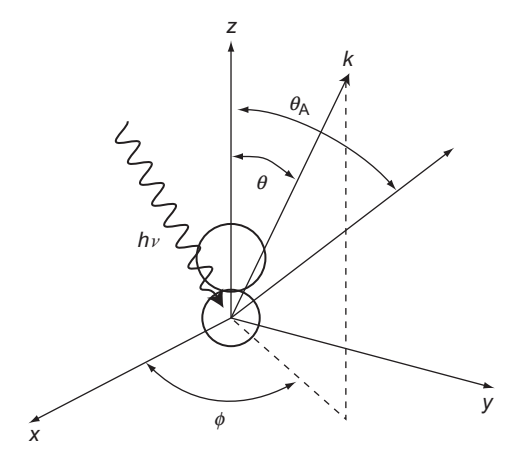


Fig. 6.26 Schematic diagram of the geometry of an angle-resolved photoemission experiment on a CO molecule oriented along the z axis, showing the definitions of the angles referred to in the text.

molecular orbitals are distributed over several atomic centres and the emission from the contributing centres is coherent. Additional contributions to the angular dependence arise from the scattering of the photoelectrons by nearby atoms in the final state. As discussed in section 3.2.1 this scattering of core-level photoelectrons in the final state, particularly from substrate atoms, can be extremely important at somewhat higher kinetic energies (~50–300 eV), and forms the basis of the structural technique of photoelectron diffraction. At the lower energies typically used in studies of molecular orbital photoemission, substrate scattering effects have often not been included in calculations. This scattering from nearby substrate atoms may well be quite strong, but it is possible that the long photoelectron wavelengths may lead to weaker angular effects. This issue will be considered again later in this section.

If one considers only the (isolated) oriented molecule approach, one can calculate the contributions to the angular dependence of the photoemission of molecular orbitals including final-state scattering *within* the molecule, as well as the initial-state effects. Using this approach, Davenport (1976, 1978) showed that, for a cylindrically symmetric molecule such as CO, the angular dependence of the emission from any state may be written as

$$\frac{d\sigma}{d\Omega} = A(\theta)\cos^2\theta_A + [B(\theta) + C(\theta)\cos 2\phi]\sin^2\theta_A + D(\theta)\sin\phi\sin\theta_A\cos\theta_A$$
(6.22)

where the functions of θ , A, B, C and D must be determined by calculation. As the final states for such a molecule, like the initial states, must have either σ - or

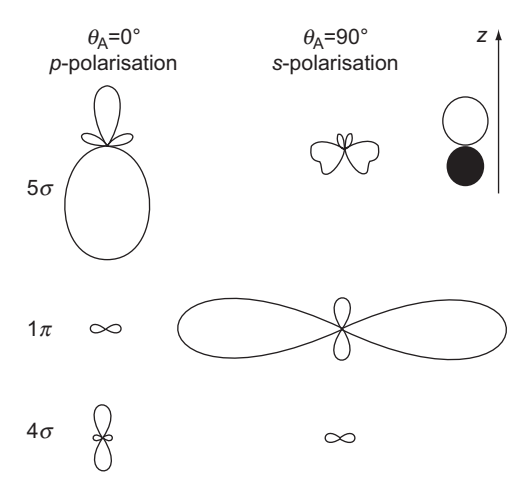


Fig. 6.27 The results of calculations of the angular dependence of photoemission (hv = 21 eV) from the three most weakly bound molecular orbitals of an oriented CO molecule with two different polarisation directions. Reprinted with permission from Davenport (1978). Copyright 1978, AIP Publishing LLC.

 π -symmetry, the first two terms in equation (6.22) arise from the squares of the amplitudes of emission into these two channels independently, while the third term gives the interference between the two channels. Much of the same structure is seen in the emission intensity from a core level of angular momentum l into the two final-state channels of angular momentum l-1 and l+1. Some rather simple remarks can be made about the values of the coefficients A, B, C and D on the basis of symmetry. In particular, for $\theta = 0$ (emission along the molecular axis) there can be no azimuthal (ϕ) dependence, so C(0) = D(0) = 0. Also, using the discussion of symmetry selection rules above, if the initial state has π -symmetry then with $\theta_A = 0$ the matrix element vanishes along the axis, so A(0) = 0. Finally, for an initial σ -state with $\theta_A = 90^\circ$, the matrix element vanishes in the $\Box = 0$ plane, so that $B(\theta) = -C(\theta)$; i.e. for emission from an initial σ -state

$$\frac{d\sigma}{d\Omega} = A(\theta)\cos^2\theta_A + B(\theta)\sin^2\phi\sin^2\theta_A + D(\theta)\sin\phi\sin\phi_A\cos\theta_A \qquad (6.23)$$

The results of calculations by Davenport (1978) for the specific system of the three most weakly bound molecular orbitals of an oriented CO molecule are shown in Fig. 6.27. These results clearly show quite strong variations in the angular dependence of the different orbitals, particularly those of different initial-state symmetry for which zero emission intensity in certain directions is consistent with the symmetry selection rules described above. Notice, of course, that while performing an experiment in *s*-polarisation can be achieved using normal incidence (even with unpolarised light), it is not strictly possible to achieve true *p*-polarisation with the

A vector perpendicular to the surface, as this would require incidence at a grazing angle of zero. In practice experiments are therefore performed at some less-grazing angle, producing components with both p- and s-polarisation, although these incident geometries are often referred to as p-polarisation. Of course, this intermediate value of θ_A leads to angular dependences that lack the symmetry of those shown in Fig. 6.27. However, calculations for different orientations of a CO molecule, performed for the true experimental conditions, were shown to be consistent with experimental data for CO adsorbed with its axis perpendicular to a Ni{100} surface by Smith et al. (1976). These authors also showed that for this orientation the intensity of the 4σ emission in s-polarisation in the mirror plane of the experiment is zero, as predicted by the symmetry selection rules. Evidently the availability of polarised light is of considerable value in identifying the orbital symmetries and orientation of adsorbed molecules, and this is one of the several benefits of using synchrotron radiation. It is possible, however, to construct quite simple polarisers, based on multiple grazing-incidence reflections from suitable mirrors, for laboratory-based experiments using He I and other gas-discharge sources.

In addition to the use of UPS to explore the occupied valence orbitals of adsorbed molecules, there have been a few experiments using inverse photoemission to identify the lowest unoccupied orbital levels. An illustration of the results of such a study is shown in Fig. 6.28 for CO, NO and N₂ adsorption on Ni{100}, taken from the work of Johnson & Hulbert (1987). The hybridisation schematic of Fig. 6.24 shows that the lowest unoccupied state (LUMO) of CO is the 2π level, which is antibonding. A key issue thought to influence the surface chemistry of CO is the location and occupation of the lowest unoccupied antibonding level. This state is unoccupied in the gas phase but partial occupation of this state, which may be induced by bonding to a surface, leads to weakening of the C-O bond and thus increases the possibility of chemistry based on this C-O bond scission. A similar role is played by the 2π -state of the isoelectronic molecule N_2 , dissociation of the N-N bond being relevant to the chemically important process of NH₃ production. There have been a number of studies of the occupied states using ARUPS and metastable He atom spectroscopy that have claimed to observe partial occupation of this level but IPES offers the possibility of observing the unoccupied part of it, which might be expected to clarify the situation. In fact, as shown in Fig. 6.28, IPES measurements indicate that the main weight of this level for several adsorption systems lies several eV above the substrate-metal Fermi level, and the significance of this has been the subject of a debate that lies beyond the scope of this book. However, a key question is the extent to which IPES measures the ground-state energies of the system. The NO spectrum of Fig. 6.28 highlights this point: NO has one more electron than CO or N_2 , so the antibonding 2π level is

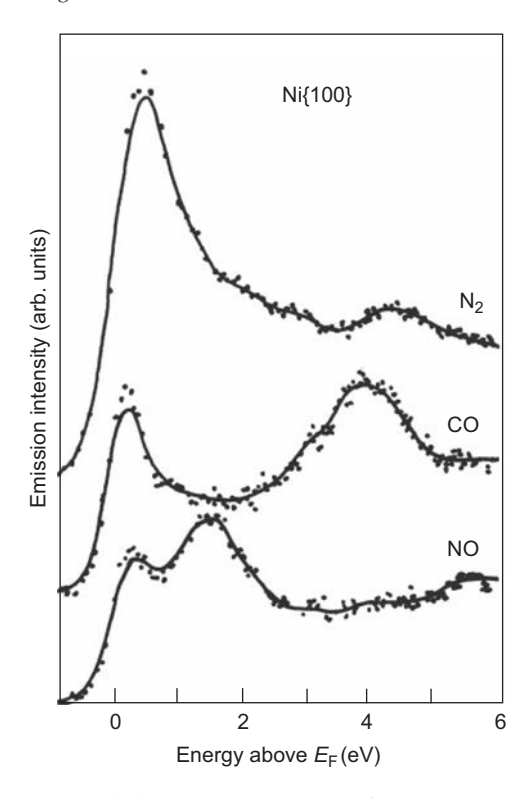


Fig. 6.28 Inverse photoemission spectroscopy data for N_2 , CO and NO adsorbed on Ni{100}. Each spectrum shows a peak just above $E_{\rm F}$ associated with transitions to the unoccupied part of the Ni d-band, and a higher energy peak associated with transitions to the 2π level of the adsorbed molecule. Reprinted from Johnson & Hulbert (1987). Copyright 1987 by the American Physical Society.

partially occupied in the free molecule. This would lead us to expect this level to form a resonance straggling the Fermi level when NO is adsorbed on a metal surface. However, the IPES peak associated with this level for NO adsorbed on Ni{100} is centred significantly (1.5 eV) above the Fermi level. Formally, of course, no spectroscopy (which always measures the difference in energy between two states of the system, at least one of which is not the ground state) can provide a direct probe of the ground state. In PES one removes an electron, and in IPES one adds an electron, so there is clearly a significant perturbation in both techniques. The most obvious manifestation of this is the so-called relaxation shift in the observed energy level, which was discussed in the context of core-level photoemission (XPS) in section 5.5.1.2, but this effect must also occur in valence levels if they involve spatially localised energy states, as is clearly the case for an adsorbate molecular orbital state. A further important consideration in the case of adsorbed molecules, however, is that by adding an electron to the molecule

(as in IPES) the technique actually measures the affinity level, which is displaced upwards in energy relative to the true ground-state orbital energy. Further discussion of this problem can be found elsewhere (e.g. Smith, 1988; Smith & Woodruff, 1987), but it is clear that not only is the interpretation of IPES data from adsorbed molecules potentially complex but also combined IPES and UPS studies of the unoccupied and occupied states are clearly of value in order to understand the problems as well as the answers!

An alternative method of gaining information on empty electronic states is nearedge X-ray absorption fine structure spectroscopy (NEXAFS), also known as Xray absorption near-edge spectroscopy (XANES). In this case significantly higher photon energies are used, sufficient to remove an electron from an atomic core level within the surface, and the absorption of the X-rays is monitored as the photon energy is scanned through the threshold for this photoionisation. Peaks in this absorption spectrum correspond to electronic transitions from the core level to the unoccupied states above the Fermi level, so the spectrum is also characteristic of the unoccupied electronic states of an adsorbed molecule. Of course, this technique also involves an excited final state, as an electron is added to the unoccupied bound (or unbound) states, but now in the presence of a core hole. The NEXAFS technique is described in more detail in section 3.2.2 in the context of the structural information that can be obtained from the application of polarisation (dipole) selection rules. The presence of peaks in the NEXAFS spectra for transitions to unoccupied molecular states of well-defined (π and σ) symmetry also provides a spectral fingerprint that may be characteristic of the molecular species. For example, if a surface is exposed to an aromatic molecule, the integrity of at least one carbon ring in the adsorbed species is characterised by a sharp π -resonance close to the C K-edge; the absence of such a peak implies that dissociation of the ring has occurred.

The application of angle-resolved UPS or ARPES to investigate the orbitals of molecular adsorbates on surfaces has more recently attracted renewed interest through the so-called 'orbital tomography' technique, first proposed by Puschnig et al. (2009). A key assumption that underpins this technique is the validity of the plane-wave approximation, i.e. the idea that an outgoing photoelectron that is detected outside the surface can be approximated by a plane wave rather than the mixture of spherical waves that provides the exact description. This approximation was first introduced by Gadzuk (1974a, 1974b, 1975) in the early development of the theory of ARPES, in the belief that the main source of the angular dependence of the photoemission would be the character of the initial state, not the final state. As discussed in section 2.2.3 the general form of the photoemission matrix element is $\langle f|\mathbf{A}\cdot\mathbf{p}|i\rangle$, where \mathbf{A} is the vector potential of the field and \mathbf{p} is the momentum operator. If one exploits the Hermitian character of the operator, which allows it to

Fig. 6.29 Schematic of the sexiphenyl molecule.

be applied to the final state, and if the final state is represented by a plane wave $\exp(i\mathbf{k}\cdot\mathbf{r})$ of wavevector \mathbf{k} , one obtains the simple result that the angle-resolved photoemission current is proportional to the square of the product of the Fourier transform of the initial-state wave function and the factor $\mathbf{A}\cdot\mathbf{k}$. This implies that the spatial distribution of an initial-state molecular orbital wave function can be obtained from a Fourier transform of the angular (photoelectron wavevector) dependence of the photoemission from this orbital state. This inversion has been referred to as orbital tomography and clearly has the potential to greatly aid the identification of different orbital peaks in a UP spectrum if the spatial distribution of the wavefunction can be mapped.

An example of the use of this procedure in an investigation of the sexiphenyl molecule (Fig. 6.29) on an Al{110} surface by Offenbacher *et al.* (2015) is given in Fig. 6.30. On the left are shown parallel-momentum maps constructed from the ARPES measurements on several molecular orbitals with for comparison simulations of these maps derived from Fourier transforms of the orbitals, as calculated with DFT. On the right the tomographic reconstructions obtained from the ARPES maps are given together with the results of DFT calculations of the wavefunctions. Notice that to achieve the reconstruction of the wavefunctions it is necessary to recover the phase lost in the measurements of the photoemission intensity (as opposed to amplitude), and this is achieved by an iterative procedure, described in detail in the original publication, in which an applied constraint is that the wavefunctions are localised on the molecule.

Despite the considerable success that has been achieved in this orbital tomography approach, it is important to recognise that the underlying plane-wave approximation is not, in general, valid; this was recognised quite early in the development of ARPES, and indeed was clearly understood by Puschnig *et al.* Most obviously, the **A·k** factor, which implies that the intensity of photoemission must always be zero in a direction perpendicular to the polarisation vector of the incident radiation, is inconsistent with the simple symmetry selection rules described above (Richardson, 1983). For example, in the case of CO bonded perpendicular to the Ni{100} surface, if the **A** vector is parallel to the surface (*s*-polarisation) the plane-wave approximation implies that photoemission from *all* orbital states must have zero intensity along normal emission (and at any emission angle within the mirror plane perpendicular to **A**). By contrast the symmetry selection rules described above show that, in these directions, one will not observe

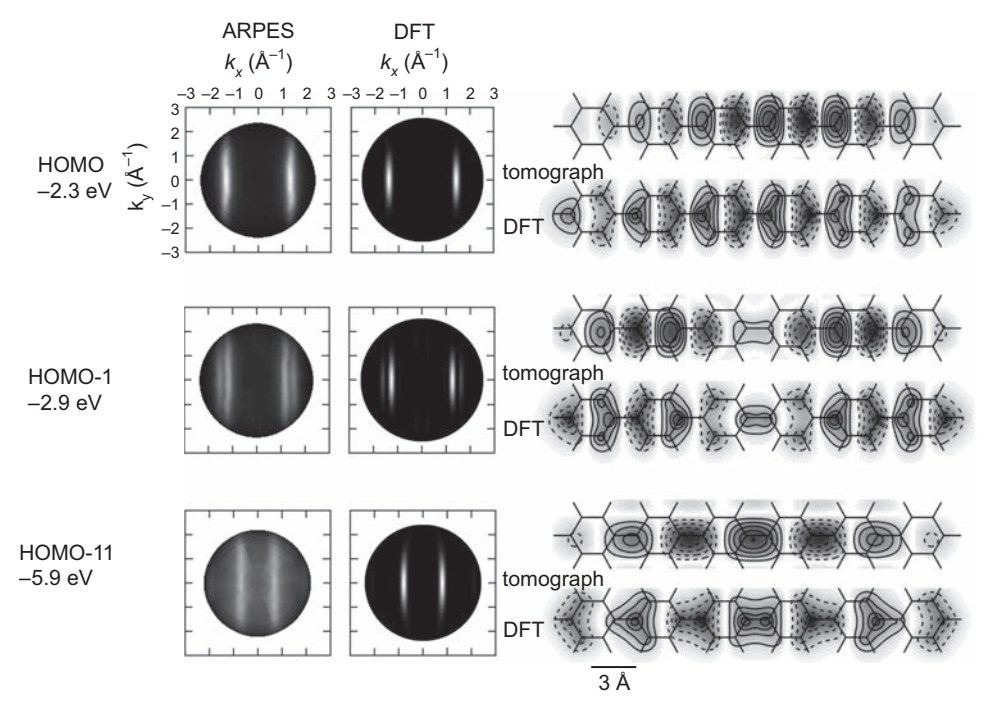


Fig. 6.30 On the left are shown experimental ARPES momentum maps from the two most weakly bound, and the most strongly bound, occupied orbitals of the upper π -band of sexiphenyl adsorbed on Al{110} with for comparison simulations of these maps based on DFT calculations of the orbitals. On the right, tomographic reconstructions obtained from the ARPES data (superimposed on the molecular framework) are given together with representations of these orbitals obtained from DFT calculations, the solid and broken contours indicating opposite phases. After Offenbacher *et al.* (2015). Monochrome figures courtesy of Michael Ramsey and Daniel Lüftner.

emission from the σ -states but one *will* observe emission from the 1π state, consistently with the predictions of Davenport shown in Fig. 6.28, and with the experimental measurements of Smith *et al.* (1976). One reason for the apparent success of the orbital tomography approach is that so far the applications have been based on ARPES measurements made only in emission directions that are close to those in which **A** and **k** are perpendicular; indeed, it is notable that, for measurements made with **k** parallel to **A**, the plane-wave approximation leads to exactly the same result as the correct spherical-wave theory, although in practice using the parallel detection mode of a modern dispersive electron energy analyser means that not all measured directions do satisfy this condition. One might also wonder why the neglect of final-state scattering both within the adsorbed molecules and from the substrate atoms below seems not to be important. The apparent absence of significant intramolecular scattering effects probably lies in the fact that the method

has so far been applied only to large essentially flat pi-conjugated organic molecules in which almost all the constituent atoms are of low atomic number and thus weakly scattering. The apparent absence of strong substrate scattering (photoelectron diffraction) effects is probably due to the fact that these molecules are large relative to the unit mesh of the underlying substrate, leading to emission from a large number of inequivalently located local atom centres within the molecule (Bradshaw & Woodruff, 2015).

Of course, while the direct inversion of ARPES data is visually very attractive, the identification of orbital states of adsorbed molecules through comparison with theory can be achieved by other means. One approach, also reliant on the plane-wave approximation, is to compare the Fourier transforms of theoretically computed orbital wavefunctions with momentum maps obtained from ARPES measurements. An alternative approach that does not rely on the plane-wave approximation, used extensively by Ueno and coworkers, is to compare the experimental momentum maps with theoretically computed maps using the so-called independent atomic centre (IAC) approach, in which the proper spherical-wave final state, and indeed in some cases also the intramolecular scattering, are included (Liu *et al.*, 2014).

An entirely different way to obtain real-space images of adsorbate molecular orbitals is by using STM or AFM. As discussed in Chapter 4, the quantitative interpretation of these images is only possible with extensive theoretical modelling. However, in combination with STS it is possible to obtain a clearer understanding of the images and their relationship to specific molecular orbitals. Figure 6.31 shows an example of results from such an investigation of the molecule PTCDA (3,4,9,10-perylene tetracarboxylic dianhydride), ordered on a graphene film grown on Pt{111}, by Martínez-Galera *et al.* (2014). The arrangement of the atoms of C and O (darker circles) in this molecule is shown in Fig. 6.31 (a). Figure 6.31(b) shows the ST spectrum that clearly identifies the HOMO and LUMO states, while Figs. 6.31(c), (d) show constant-current STM images recorded at bias voltages corresponding to these two orbital states, together with visualisation of these orbitals obtained from DFT calculations.

6.3 Desorption Techniques

6.3.1 Thermal Desorption and Reaction Spectroscopy

A very different way of identifying molecular adsorption states on surfaces is by desorbing them from the surface and detecting the desorbed species. One method of achieving this, using incident ion bombardment, leads to the technique of SIMS described in section 2.5, but as described there the interpretation of the data

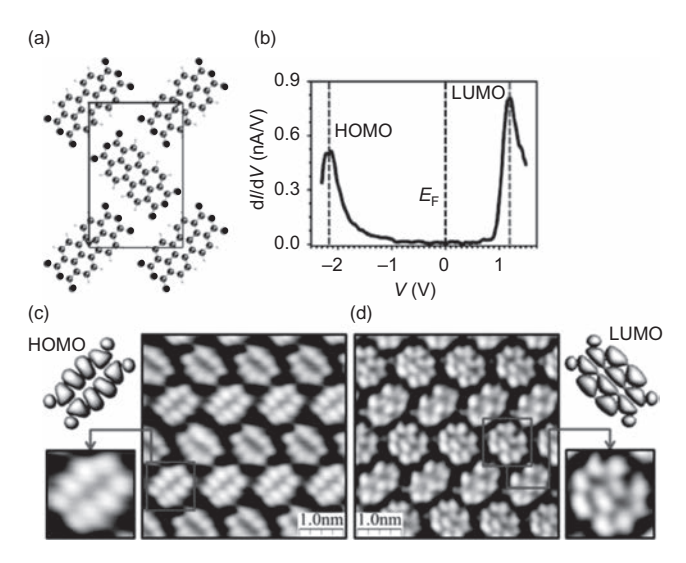


Fig. 6.31 STM and STS results from a study of PTCDA on graphene monolayers on Pt{111}. Panel (a) shows a schematic diagram of the molecular ordering (O atoms are shown as darker circles). Panel (b) shows the ST spectrum, identifying the HOMO and LUMO orbital energies. Panels (c) and (d) show STM images recorded at bias voltages of -2.3 V and +1.24 V corresponding to the HOMO and LUMO energies, together with the results of DFT calculations of these orbitals. Adapted with permission from Martínez-Galera *et al.* (2014). Copyright 2014 American Chemical Society.

obtained from this method is far from straightforward. A much simpler approach is to desorb the adsorbed molecules by thermal excitation. Any adsorbed species must be bound to the surface with some specific amount of energy and will desorb at a rate determined by a Boltzmann factor. Heating the surface will increase this desorption rate, and the desorbing species may be detected in the gas phase by conventional mass spectrometers such as those commonly installed on UHV surface science chambers to monitor the partial pressures of different residual or reactant gases in the vacuum. A study of the temperature dependence of the rate of desorption can therefore lead to information on the binding energy states of the adsorbate (or, more strictly, on the desorption energies), and indeed on the number of desorbed molecules, through suitable calibration experiments. Of course, the binding energy states investigated will relate to those occupied at the temperature at which the rate of desorption is substantial; these may not be the same as the states occupied at lower temperatures. Indeed, it is possible that an adsorbed molecule may dissociate during heating, so that any desorbed species may correspond to molecular fragments; monitoring this process can also provide valuable information on surface reactions, as described more fully below.

The pressure rise P in a continuously pumped chamber of volume V during a sample heating cycle depends on a balance between the rate of desorption and the pumping speed S:

$$dN/dt = (V/Ak_BT_g)[dP/dt + (S/V)P]$$
(6.24)

where N is the surface coverage (molecules per unit area), A the surface area and $T_{\rm g}$ the gas temperature. A significant simplification arises if the ratio of the pumping speed and chamber volume is large, because in this case $dP/dt \ll (S/V)P$, leading to a linear dependence of the pressure rise on the desorption rate. In early thermal desorption studies, in which the sample was often a polycrystalline wire, so-called flash filament experiments involved very high heating rates, which led to much more rapid pressure rises, but single-crystal studies invariably use the lower heating rates that are consistent with a linear relationship of desorption rate and pressure. The 'flash' terminology remained for some years, the technique being referred to as flash desorption, but subsequently it has been more commonly referred to as temperature programmed desorption (TPD) or thermal desorption spectroscopy (TDS), the heating rate generally being arranged to be give a linear time dependence of the temperature. This superficially very simple technique is not without its pitfalls. If the heating rate is too slow, re-adsorption of molecules from a weakly adsorbed state into a more strongly adsorbed state can occur, while the mode of heating and sample mounting can lead to significant temperature variations across the sample during the heating cycle. A further problem is the influence of desorption from the sample supports or the heating filaments; the effect of this can be minimised by ensuring that the mass spectrometer is positioned close to the sample with direct line-of-sight and by interposing some kind of simple gas collimating tube. Specific arrangements designed to optimise this condition are referred to as line-of-sight mass spectrometry (LOSMS) and have recently been reviewed by Hessey and Jones (2015).

The rate of desorption from a species in state i on the surface is given by

$$-dN_i/dt = v_i N_i^{x_i} \exp(-E_i/RT)$$
(6.25)

where x_i is the reaction order for desorption, v_i is a frequency factor, E_i is the activation energy for desorption and N_i is the population, all from the state i. The reaction order in thermal desorption depends on the nature of the surface species leading to the desorption. For the desorption of a molecule adsorbed intact on a surface the rate of desorption will depend linearly on the number of surface species available for desorption, leading to a first-order desorption rate $(x_i = 1)$. If a diatomic molecule is dissociatively adsorbed but desorbs re-associatively (e.g. H_2 or even CO) then a requirement for desorption is that there are two suitable

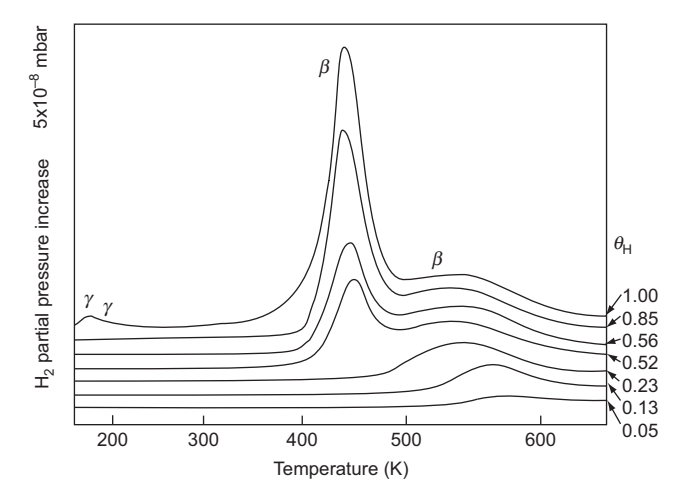


Fig. 6.32 Thermal desorption spectra obtained from increasing initial exposures of W{100} to molecular hydrogen at ~100 K. The initial hydrogen coverages in monolayers, $\theta_{\rm H}$, are shown. After Yates & Madey (1971).

adsorbed atoms adjacent to one another, the probability for which depends on the square of the surface concentration of the atoms. This is an example of a second-order reaction ($x_i = 2$).

An early example of thermal desorption spectra is shown in Fig. 6.32 for the case of hydrogen adsorption on W{100}. The crystal surface was initially subjected to increasing exposures of molecular hydrogen at ~100 K and then heated at approximately 16 K s⁻¹ (the spectral data are plotted on a linear time scale that is not quite linear in temperature). Two distinct peaks are seen for most exposures, assumed to correspond to two distinct adsorption states, labelled β_1 and β_2 . A striking feature of these spectra is that the temperature corresponding to the β_1 desorption is almost completely independent of coverage, whereas the peak corresponding to the β_2 state shifts to lower temperature with increasing coverage. The β_1 and β_2 peaks thus show the behaviour expected of first-order and second-order desorption, respectively. This might be thought to imply that the β_1 state corresponds to molecular adsorption and the β_2 state to atomic (dissociative) adsorption. In fact this proves not to be the case: both states correspond to dissociative adsorption. Indeed, HREELS measurements established that in both states the adsorption H atoms are in local bridging sites (Barnes & Willis, 1978), but at the very high coverages leading to the β_1 desorption peak (0.25-1.0 ML) the availability of near-neighbour H atoms is such as to produce first-order desorption. The β_2 desorption peak, corresponding to $\theta_{\rm H}$ < ~ 0.25 ML, displays the second-order desorption more typically expected for an initial dissociative adsorption state. Very weak γ desorption peaks, seen at

low temperature following the highest exposures, presumably do correspond to molecular adsorption. In fact understanding the superficially simple W{100}/H system has proved to be rather complicated, in part because not only can sufficient H coverage produce a $c(2\times2)$ -H ordered reconstruction but also the clean W{100} surface was found to have a different $c(2\times2)$ reconstruction (King & Thomas, 1980).

One of the main objectives of the TPD technique is to provide a means of determining the desorption energies of the different states identified by the various peaks in the spectra. A relatively simple result emerges for the case of first-order desorption using a linear temperature ramp ($T = T_0 + \beta t$), where β is the rate of increase in temperature; this result is obtained by noting that the rate of change of the desorption rate goes to zero at the top of a peak, so if one differentiates equation (6.25) with respect to time then the condition $d^2N_i/dt^2 = 0$ corresponds to the temperature of the desorption peak, $T = T_p$. This leads to the result

$$E_i/RT_{ip}^2 = (v_i/\beta)\exp(-E_i/RT_{ip})$$
(6.26)

As pointed out by Redhead (1962), the relationship between E and T_p is linear to within $\pm 1.5\%$ for values of v_i/β in the range 10^8 to 10^{13} K⁻¹, which leads to a particularly simple result:

$$E_i/RT_p = \ln(v_i T_{ip}/\beta) - 3.64$$
 (6.27)

Figure 6.33 shows this relationship plotted for the case $v = 10^{13}$ and for several values of β in the range 1 to 1000 Ks⁻¹. Evidently it provides a very simple and convenient way to extract values of desorption energies from TPD data and has been widely used for this purpose; the value of v is generally taken to be 10^{13} . Of course, without proper determination of the value of v (which can potentially vary by several orders of magnitude) the resulting value of E_i is no more than an estimate, but the fact that equation (6.27) depends only on the logarithm of v does somewhat ameliorate this problem. Of course, in the underlying derivation it is assumed that the desorption is first order, but even for second-order desorption (for which T_{ip} depends on coverage) a reasonable estimate can be obtained by using the TPD spectrum for a low coverage of the adsorbate.

A range of more complex procedures have been explored in order to go beyond this very simple approach (King, 1975; de Jong & Niemandsverdriet, 1990). These are still based on equation (6.25) but it is no longer assumed that E_i and v_i are independent of coverage. Whereas the simple approach based on Fig. 6.34 can be applied to a single TPD spectrum, more exact methods rely on there being a larger number of such spectra recorded at different initial coverages. For the simplest case, that of a desorption spectrum containing only a single peak, the so-called

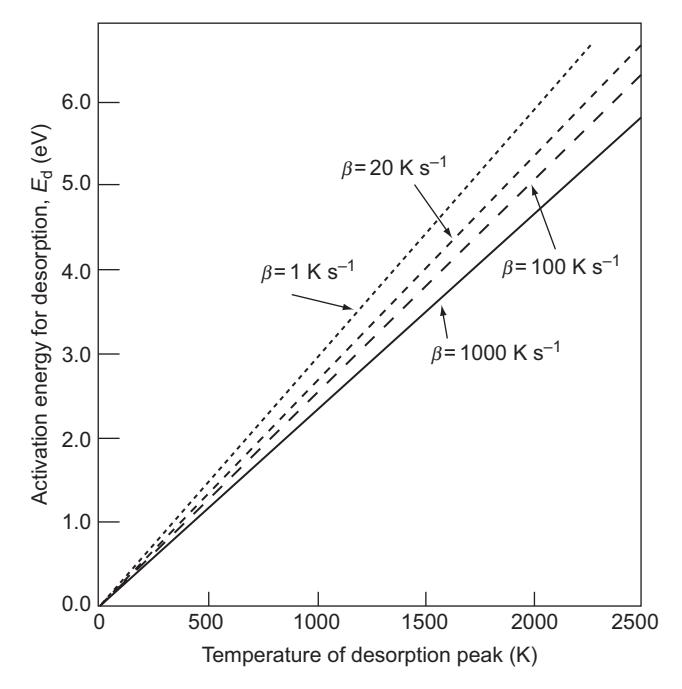


Fig. 6.33 The relationship of the desorption energy and the temperature of the corresponding desorption peak, for a range of different linear heating rates, according to equation (6.27), for the case $v = 10^{13}$. After Redhead (1962).

'complete' analysis exploits the fact that if $dP/dt \ll (S/V)P$ then by integrating equation (6.24) one obtains the coverage at a time t after starting the heating cycle:

$$N_t = \frac{S}{AkT_g} \int_{t}^{\phi} P dt \tag{6.28}$$

From a set of desorption spectra at different initial coverages it is then possible, using this equation, to construct a set of curves of the dependence of N_t on t (and thus also on T). As the pre-exponential factor of equation (6.25) (vN^{x_t}) is constant for a particular value of N_t (independently of the values of v and x) it is then possible to create an Arrhenius plot of the logarithm of the desorption rate against 1/T at constant N_t . The gradients of a family of these plots thus provide E(N) as a function of N. Moreover, the intercepts of these Arrhenius plots yield values of $\ln v(N) + x \ln N$. If v is independent of N then a plot of these intercepts as a function of $\ln N$ is linear, with gradient x and intercept v. If this plot is not linear then one must try alternative values of x to determine v(N), leading to some ambiguities.

Alternative approaches involve fitting the complete set of desorption spectra by computer modelling for different coverage dependences of E and v. An evaluation

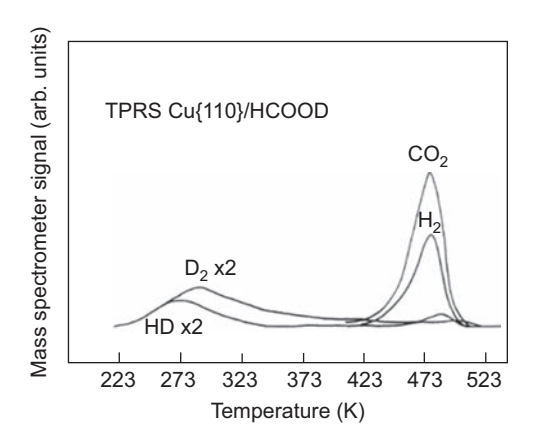


Fig. 6.34 Temperature programmed reaction spectra for the products evolved from a Cu{110} surface exposed to HCOOD (with a small amount of HCOOH) at 200 K. Reprinted from Madix (1979). Copyright 1979 with permission from Elsevier.

of ten different procedures was performed by de Jong & Niemandsverdriet (1990) using simulated data for which the true solutions were therefore known; perhaps unsurprisingly they concluded that the 'complete' methods involve a lot more effort but are more reliable than the simple methods. Notice that with proper analysis of TPD data it is possible not only to determine activation energies for desorption but also to gain information on adsorbate—adsorbate interactions. A further important feature is the ability to determine absolute surface coverages of desorbed species, subject to some calibration of the instrumentation for a system of known coverage.

One limitation of the TPD technique already mentioned is that the state of a molecular adsorbate may differ, at the temperature of desorption, from its state at lower temperatures, owing to thermally induced transitions during the heating cycle. However, this aspect of the technique can also be exploited to considerable benefit in a variant of the method generally referred to as temperature programmed reaction spectroscopy (TPRS). An early example of this technique is provided by an investigation of the desorbing reaction products following the adsorption of formic acid on a Cu{110} surface (Madix, 1979), the results of which are shown in Fig. 6.34. In order to understand more fully the nature of the surface interaction the surface was exposed to isotopically labelled formic acid in which the acid hydrogen had been deuterated (i.e. to HCOOD, although a lesser amount of undeuterated HCOOH was also present). As shown in Fig. 6.34, the TPR spectrum shows desorption of D₂ and HD at ~273 K and coincident desorption of H₂ and CO₂ at ~473 K. On the basis of this information one may infer that the low temperature hydrogen (D₂ and HD) desorption must result from deprotonation of the acid,

implying that this leaves a surface formate species (HCOO) on the surface. This formate then dissociates into CO_2 and hydrogen at the higher temperature; i.e.

$$\begin{split} & HCOOD_{(a)} \to \ HCOO_{(a)} + D_{(a)}, \ \ 2D_{(a)} \to D_{2(g)} \\ & HCOO_{(a)} \to H_{(a)} + CO_{2(g)}, \ \ 2H_{(a)} \to H_{2(g)} \end{split} \tag{273 K}$$

where the suffices (a) and (g) correspond to the adsorbed and gas-phase species respectively.

Note that the coincidence of the H_2 and CO_2 desorption peaks at 473 K indicates that the desorption of these species is limited by the dissociation of the formate species itself and not by the activation energy for desorption of adsorbed H, or H_2 , and CO_2 . Indeed, both these species, if adsorbed separately on $Cu\{110\}$, desorb at much lower temperatures. However, on the basis of these data, the lower temperature desorption of D_2 and HD could be due either to the acid deprotonation occurring at ~273 K or to this deprotonation occurring at a lower temperature and the associated desorption of the D_2 then being activated at ~273 K. Vibrational and electronic spectroscopic methods have provided clear identification of the (inferred) adsorbed formate as a reaction intermediate (e.g. the NEXAFS data of Fig. 3.55), but they also show that the D_2 or HD emission is reaction limited rather than desorption limited.

A more recent example of the adsorption of a different carboxylic acid shows both similarities and difference from the case of formic acid. The tartaric acid molecule shown in Fig. 6.35 is chiral, having two different forms that are mirror images of one another but are not equivalent; effectively they are left-handed and right-handed versions of the same combination of functional groups. Interest in the surface studies of chiral molecules is motivated, in part, by the need to synthesise one particular form (one of the alternative 'enantiomers') of these molecules, particularly those used in pharmaceuticals where one enantiomer may be very beneficial but the another very harmful. Enantioselective heterogeneous catalysts could be of great benefit in producing only the intended enantiomer. Many investigations of tartaric acid on surfaces have been directed to exploring chiral effects, although in the experiment reported here the chirality of the molecule is not particularly relevant. As shown in Fig. 6.35, tartaric acid contains two carboxylic acid (-COOH) groups linked by two COH2 groups, the C atoms of these latter groups being chiral centres (as indicated by the asterisks in the diagram); the molecule studied in this experiment had the arrangement of bonding at these centres denoted as S,S-tartaric acid.

In the TPRS spectra three peaks in the mass spectrum were monitored during the heating cycle, corresponding to 2 amu (H_2) , 28 amu (CO) and 44 amu (CO_2) ; the peak corresponding to 18 amu (H_2O) was also monitored but desorption of these

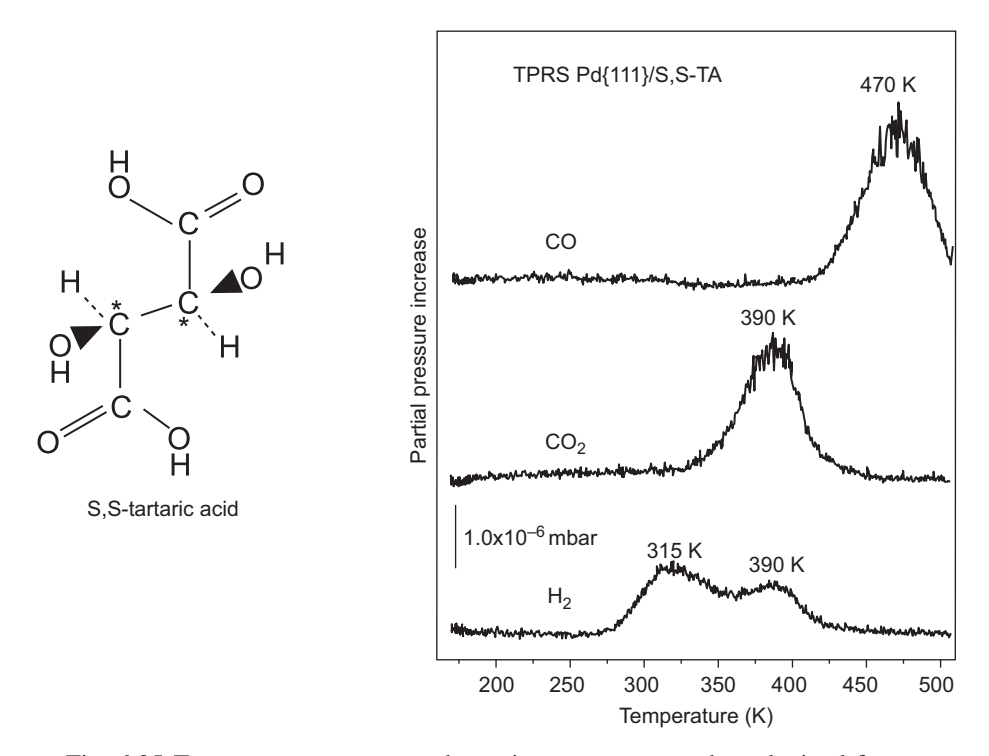


Fig. 6.35 Temperature programmed reaction spectroscopy data obtained from a low coverage of S,S-tartaric acid (the molecule is shown on the left) on Pd(111). Reprinted from Mahapatra & Tysoe (2014). Copyright 2014 with permission from Elsevier.

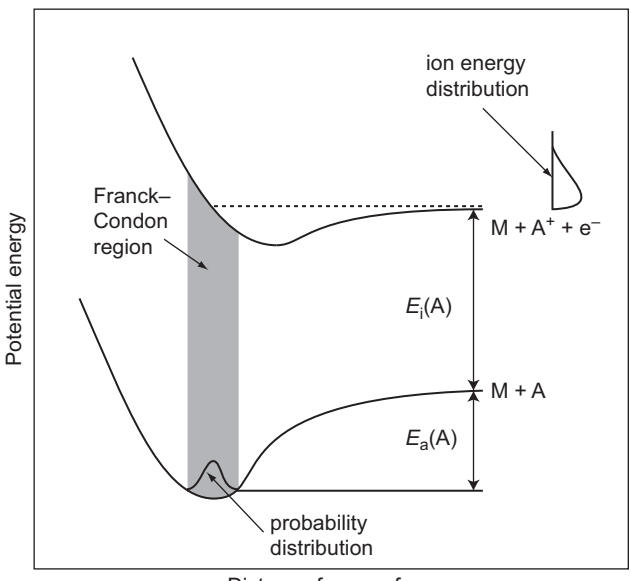
species was only seen at much higher initial coverages of the molecule. The qualitative behaviour of the H₂ and CO₂ desorption is similar to that arising from formic acid seen in Fig. 6.34 and can be interpreted similarly; the lower temperature H₂ peak is assigned to the consequence of deprotonation of the acid hydrogen, leaving a carboxylate (-COO) species on the surface, while the higher temperature peaks, of H₂ and CO₂, occurring at the same temperature, can be attributed to dissociation of this carboxylate. In addition, however, a CO desorption peak is seen at a significantly higher temperature. The temperature associated with this desorption is the same as that seen for CO adsorbed on a clean Pd(111) surface, so one may conclude that this is a desorption limited peak, the CO being produced in the dissociation at ~390 K but initially remaining adsorbed on the surface. The CO₂ production presumably results from detachment of the carboxylate COO, while the CO results from fragmentation of the COH₂ groups. As tartaric acid contains two carboxylic acid groups, an interesting question is whether the initial acid deprotonation (leading to the lower temperature H₂ desorption peak) is of only one of these groups or of both, producing a reaction intermediate that is either a monotartrate or a bitartrate respectively. While the answer to this question can be obtained from vibrational or electronic spectroscopy, the more complete TPRS data of this experiment also provide a strong clue. In particular, TPRS data recorded from higher initial exposures of tartaric acid show a smaller H₂ desorption peak at lower temperature and an enhanced higher temperature H₂ desorption peak. The implication is that at low coverages both acid groups are deprotonated, leading to bitartrate species, whereas with increasing coverage further adsorption leads to an increased coverage of monotartrate species. Indeed, the reduction in intensity of the lower temperature H₂ desorption peak with increased coverage implies that at least some initial bitartrate species are reprotonated to create monotartrate adsorbates. Exactly this behaviour had previously been found for tartaric acid adsorption on Cu{110}, and indeed a structural study of the reaction intermediates by photoelectron diffraction shows that the bitartrate 'lies down' on the surface (bonded by all four COO oxygen atoms) while the monotartrate 'stands up', bonding to the surface by the two O atoms of the one carboxylate group (Duncan et al., 2012b).

6.3.2 Electron and Photon Stimulated Desorption

An entirely different way of desorbing atoms and molecules (and molecular fragments) from a surface is by bombarding the surface with incident electrons or photons. This effect has been pursued mostly using incident electrons, with energies of no more than a few tens to low hundreds of eV, leading to the technique of electron stimulated desorption (ESD). It is easy to show that the mechanism for this process is *not* the transfer of energy and momentum from the incident electrons by direct impact onto an adsorbed atom. As shown in section 2.4 in the context of ion scattering, the conservation of energy and of momentum lead to the result that the recoil atom energy E_2 relative to the incident particle energy E_0 is given by equation (2.14):

$$\frac{E_2}{E_0} = \frac{4A}{(1+A)^2} \cos^2 \theta_2$$

where A is the ratio of the mass of the scattered (recoiling) particle and the mass of the incident particle, and θ_2 is the angle between the incident particle trajectory and the recoiling particle trajectory. For an incident electron of mass m_e , striking an atom of mass M, the value of A is very large (> ~2000), so the largest energy transfer, corresponding to $\theta_2 = 0$, is $\approx 4E_0m_e/M$, which even for the smallest possible mass, that of an H atom, leads to an energy transfer from a 100 eV electron of ~0.2 eV, far smaller than a typical binding energy of a chemisorbed



Distance from surface

Fig. 6.36 Schematic potential energy curves for the interaction between a surface M and an atom A, and between M and the ion A^+ . A possible electronic transition resulting in the electron stimulated desorption of A^+ is indicated by the shaded region.

H atom on a surface of a few eV. For only slightly heavier atoms, such as C, N and O, the energy transfer is an order of magnitude less.

It is therefore clear that the mechanism in ESD (and PSD, photon stimulated desorption) is through an electronic excitation. Mechanisms for ESD based on the models for electronic excitation and dissociation of gaseous molecules were first proposed by Menzel & Gomer (1964) and Redhead (1964) and the general model has come to be known as the Menzel–Gomer–Redhead or MGR model. These mechanisms (and the Knotek–Feibelmen mechanism discussed below) have as their basis the Franck–Condon principle, which states that, during an electronic transition in a molecule, the nuclear separation and relative velocity are essentially unchanged; that is, the electronic transition takes place quickly compared with the time scale of vibrational and rotational modes of the molecule.

By analogy with a diatomic molecule, the potential energy of interaction between a metal substrate surface M and an adsorbate atom A can be represented by a potential energy curve such as that shown in Fig. 6.36. This curve represents the lowest bound state of the metal–adsorbate system; $E_a(A)$ is the adsorption energy of the atom A. The upper curve represents the state $M + A^+ + e^-$; at large distances from the surface, the curves are separated in energy simply by the ionisation potential of the free atom $E_i(A)$. Following bombardment with

electrons, transitions may occur from the bonding M + A curve to the repulsive part of the upper curve. The range of possible internuclear separations in the ground state is represented by the width of the shaded area, while the probability of a particular internuclear separation is the modulus squared of the wavefunction for the ground-state M-A oscillator. The Franck-Condon principle states that the range of internuclear separations allowed for the M-A system is unchanged immediately after the transition, and the final states on the upper curve are distributed over the Franck-Condon region. The A⁺ ions formed at the repulsive part of the $M + A^{+} + e^{-}$ curve may desorb with a range of kinetic energies, as indicated in the figure. The actual yield of positively charged ions, and indeed the energy distribution, will, however, be modified by reneutralisation. In particular, charge exchange can occur by either Auger or resonance neutralisation as discussed in section 2.4.2. Reneutralisation of the ion results in a transition back to the bonding M + A curve. Depending on the kinetic energy gained by the ion before neutralisation, the atom A may be trapped in a vibrationally excited electronic ground state or may desorb as a neutral atom. Indeed, there are also other possible routes to the electron-stimulated desorption of neutral atoms; Franck-Condon transitions can occur from the ground state to a fully repulsive antibonding state or to an excited atom state that may be repulsive at the M-A separation of the ground state.

In fact, a simple theory based on excitation to a repulsive ionic state, plus the possible effects of reneutralisation, can account for *most* of the basic observations of ESD. These are that: (i) generally many more neutrals than ions are observed; (ii) the cross-sections for neutral desorption are usually orders of magnitude smaller than for comparable gas phase processes, while the cross-sections for ionic desorption are correspondingly even smaller; (iii) different modes of bonding of electronegative adsorbates exhibit different ESD cross-sections; (iv) ESD is not observed for metallic adsorbates on metal substrates.

Referring to Fig. 6.36, excitation from the ground state to the repulsive part of the ionic state is followed either by desorption as an ion or by reneutralisation. If neutralisation occurs before some critical distance x_c , recapture results. If, however, reneutralisation occurs after the ion has passed x_c then the neutral thus formed will have sufficient energy to escape.

The probability of the desorption of an ion formed by electronic excitation of an adsorbed neutral species at a distance x_0 from a surface is given by (cf. equation (2.26))

$$P_{\rm I}(x_0) = \exp\left[-\int_{x_0}^{\phi} \frac{R(x)}{v} \, \mathrm{d}x\right]$$
 (6.29)

where R(x) is the rate of neutralisation of the ion at a distance x and v is the component of the velocity of the ion perpendicular to the surface. The velocity of the ion at x is

$$v = \left\{ 2[V(x_0) - V(x)]/m \right\}^{1/2} \tag{6.30}$$

where V(x) is the excited-state potential function and m is the mass of the ion. Combining these two equations gives

$$P_{\rm I}(x_0) = \exp\left(-m^{1/2} \int_{x_0}^{\phi} \frac{R(x) dx}{\left\{2[V(x_0) - V(x)]\right\}^{1/2}}\right)$$
(6.31)

Alternatively, the total probability of desorption, regardless of mode, is given by

$$P_{\rm T}(x_0) = \exp\left\{-m^{1/2} \int_{x_0}^{x_{\rm c}} -\frac{R(x) dx}{\left[V(x_0) - V(x)\right]^{1/2}}\right\}$$
(6.32)

where x_c is the critical capture distance for the ion excited at x_0 .

It is clear from the last two expressions that $P_{\rm T}(x_0)\gg P_{\rm I}(x_0)$ and that more neutrals than ions are expected in ESD, as supported by direct experimental evidence. Moreover, the dependence of the (more easily detected) ion fraction on $m^{1/2}$ means that different isotopes of the same adsorbed species should have different ion yields (because their escape velocities differ), an effect confirmed experimentally by Madey *et al.* (1970). Although the basic mechanism of ESD is the same for free molecules and for atoms and molecules adsorbed on surfaces, the ion yields for desorption from (mainly metal) surfaces are very much lower owing to the much higher efficiency of reneutralisation at a metal surface, with its highly delocalised valence electrons, the valence energy levels being broadened into bands a few eV wide. Early measurements of the absolute ESD ion yields, tabulated in the review of Madey & Yates (1971), fall in the range 10^{-28} – 10^{-22} m² while the total yields (including neutrals) are typically 2–3 orders of magnitude larger.

As is evident from Fig. 6.36, it should, in principle, be possible to determine the adsorption energy of the desorbing ions from a measurement of the threshold energy required in the incident electrons for the production of a detectable yield. In practice, this is not really possible. Firstly there is some ambiguity regarding the final states of the incident electron and of the electron removed from the adsorbed neutral atom (or molecule). If both these electrons are assumed to have a final state of zero kinetic energy in the vacuum then the threshold energy for ESD is simply $E_i(A)+E_a(A)$, but if one or both these electrons have a final state at the Fermi level then the threshold energy is reduced by either the work function or twice the work

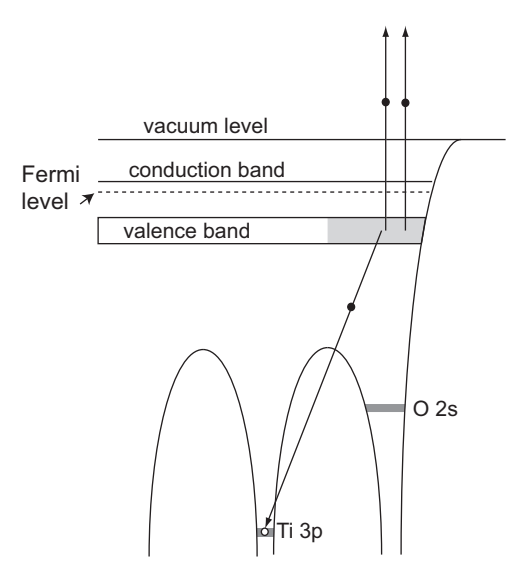


Fig. 6.37 Energy level diagram showing the Knotek–Feibelman (1978) mechanism of O^+ ESD from a TiO_2 surface. Initial ionisation of the Ti 3p state leads to an interatomic Auger transition, the O^{2-} ion being converted to O^+ , which is ejected from the surface by a Coulomb explosion.

function. A second problem is that, as discussed in section 2.3.1 in the context of Auger electron spectroscopy, electron ionisation cross-sections are very low at threshold, rising only as the incident energy increases to values well above threshold. Threshold ESD signals are therefore expected to be extremely weak.

A fundamentally different mechanism for ESD was proposed by Knotek & Feibelman (1978) to account for the ESD of O⁺ ions from several transition metal oxide (TiO₂, V₂O₅, WO₃) crystal surfaces. These authors noted that ESD was extremely weak for incident electron energies below about 20 eV, a condition that should lead to ESD according to the MGR model, but that a dramatic increase in yield occurred, with incident electron energies corresponding to the highest lying atomic core levels of the metal atoms, in the range ~25–35 eV. Figure 6.37 shows the relevant energy levels and the proposed ESD mechanism for the case of TiO₂. A key result from ESD studies of this ionic oxide material is that the O atoms are in a negative ion state, generally regarded as O²⁻, yet the ion species detected in ESD is O⁺. This implies that the desorption process must be capable of removing three electrons from the O ions in the solid surface. The proposed mechanism involves initial electron ionisation of the Ti 3p state (33.6 eV below the conduction band), which is then refilled by an Auger transition. However, because the Ti atoms in the solid are stripped of their valence electrons to produce Ti⁴⁺ ions, this filling of the Ti 3p core hole must occur by an interatomic Auger transition, with the

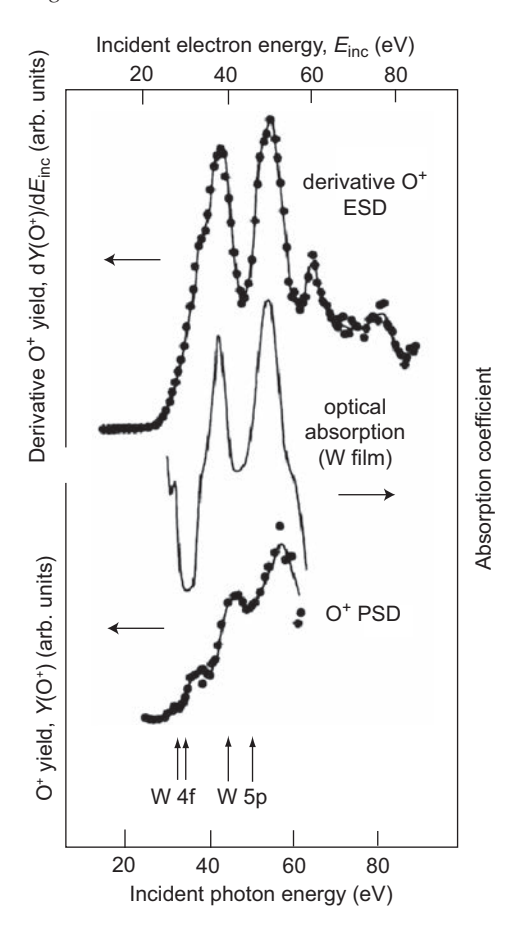


Fig. 6.38 Photon stimulated yield curve of O⁺ emission from O adsorbed on W{100} shown for comparison with the energy derivative ESD from the same surface and with the optical absorption spectrum of a W foil. All curves are normalised to constant incident photon or electron flux, while the ESD is offset in energy by 5 eV as an approximate work function correction to give the same excitation energy relative to the Fermi level. The approximate binding energies of the W 4f and 5p core levels (which are dependent on the oxidation state) are also shown. Reprinted from Woodruff *et al.* (1981). Copyright 1981, with permission from Elsevier.

consequence that the ${\rm O}^{2-}$ ion can be converted to an ${\rm O}^{+}$ ion, which is ejected from the surface by a Coulomb explosion.

The Auger decay of an ionised core level has subsequently been shown to be an important desorption mechanism in many adsorption systems. Figure 6.38 shows the results of measurements on O⁺ desorbing from an O-exposed W{100} surface obtained using both ESD and photon stimulated desorption (PSD). Clearly the electronic excitation processes of both the MGR and Knotek–Feibelman

mechanisms should be achievable by incident photons of sufficient energy as well as by incident electrons, and many experiments, including the early work of Knotek et al. (1979) and the data presented in Fig. 6.38, have illustrated the equivalence of the two processes in threshold energies. Photon stimulated desorption has some advantage over ESD in determining threshold energies, because photoionisation cross-sections generally rise very sharply at threshold and then fall off with increasing energy while electron ionisation cross-sections rise far more slowly, as described in Chapter 2. Moreover, while electron ionisation crosssections do fall off (after peaking at about three times the threshold energy), the effect of desorption induced by the increasing number of low energy secondary electrons that result from an increased primary electron energy means that the peak in cross-section is often not reflected in the measured ion yield. While PSD yield curves show thresholds far more clearly than ESD yield curves, an electron energyderivative ESD yield can show the same fine detail, as in Fig. 6.38. Tungsten 5p and 4f core-level ionisation thresholds are clearly seen in the O+ PSD and derivative ESD yields, the effect of these levels also being seen in an optical transmission spectrum of a W foil. Notice, though, that the surface oxide is expected to show chemical shifts in these energies relative to the metallic foil. Fluorine⁺ and Cl⁺ ions from surface contaminants that were found to desorb from this surface did not show thresholds associated with the W core levels but desorbed if the photon and electron energies were above ~15 eV, presumably via an MGRtype of mechanism.

Most early ESD experiments used a magnetic-sector mass spectrometer to identify the desorbing species, detecting mainly positively charged ions but also neutrals using the ioniser of the mass spectrometer. Later studies have increasingly used quadrupole mass spectrometers. The energy distribution of the desorbing ions has typically been determined using a simple retarding field analyser such as that shown schematically in Fig. 6.39. The principle of such a device, which acts as a high-pass energy filter, was described in Chapter 1. An inner grid at the same potential as the sample ensures that there is a field-free space for the ions to travel through, while a retarding grid allows only ions with more than a certain energy, defined by the potential on these grids, to reach the detector. In early studies the incident electrons came from a filament placed in front of the sample, the filament being biased relative to the sample to define the incident electron energy. Subsequent studies replaced this filament by a simple electron gun such as those used in LEED and Auger electron spectroscopy. Figure 6.39 also shows a modification of this arrangement in which the collector must be removed (or replaced by a grid), allowing the ions to impact onto a microchannel plate (MCP) amplifier behind which may be mounted a fluorescent screen or a position-sensitive detector. In this configuration one can also measure the ESD ion angular distribution (ESDIAD),

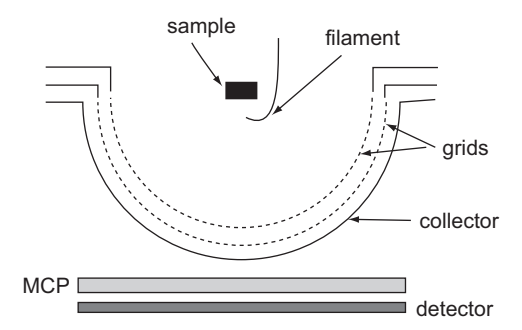


Fig. 6.39 Compound schematic diagram showing the main components of different instrumental arrangements that have been used to determine the energy distribution of desorbed ions in ESD, and to measure their angular dependence.

the information content of which is described in more detail below. Combination instruments, incorporating both a quadrupole mass spectrometer and a retarding field analyser (with a small hole in the grids and collector to allow some ions to reach the mass spectrometer), permit both the identity and the energy spectrum of the desorbed ions to be determined.

A quite different approach was demonstrated by Traum & Woodruff (1980), who used a standard dispersive cylindrical mirror analyser (see Chapter 1) to determine both the energy spectrum of the desorbed ions and their mass-to-charge ratio. The energy spectra were obtained using the analyser in its standard dispersive mode at a fixed pass energy of 78 eV but, in addition, by pulsing the incident electron beam they were also able to measure the time of flight of the ions through the analyser. The flight time at a known ion energy in the analyser also allowed the mass-to-charge ratio to be detected. The results obtained in this way for the desorption of several species from a slightly contaminated W{100} surface that had been exposed to oxygen are shown in Fig. 6.40. Figure 6.40(a) shows time-offlight spectra recorded with the CMA set to accept ions at two different kinetic energies, while Fig. 6.40(b) shows the ion energy spectra recorded at the flight times corresponding to the four peaks seen in the time-of-flight spectra. This mode of ESD data collection does not appear to have been pursued subsequently although it could be used in more modern dispersive analysers fitted with multichannel parallel detections schemes, allowing the angular distributions of the ions also to be detected.

The time-of-flight method, in a rather specialised form, has been used to detect the mass (but not the energy) of desorbed ions in PSD. Almost all PSD experiments to date have been performed using synchrotron radiation, primarily because a strength of PSD lies in the potentially richer threshold energy information available using tunable radiation in the energy range above about 20 eV.

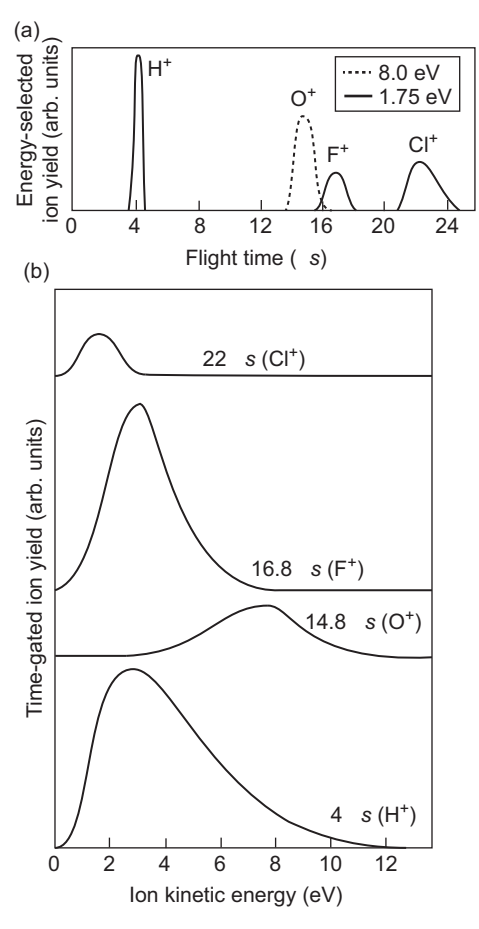


Fig. 6.40 Electron stimulated desorption data from a contaminated W{100} surface, the emitted positively charged ions being selected by a CMA with the output measured at fixed time intervals after a stimulating incident electron pulse. Panel (a) shows the time-of-flight spectrum recorded at two different pass energies corresponding to different initial ion energies. Panel (b) shows the ion energy spectra recorded at fixed time delays corresponding to different emitted species. Reprinted with permission from Traum & Woodruff (1980). Copyright (1980), AIP Publishing LLC.

One feature of synchrotron radiation is that it is intrinsically pulsed and, in the case of a single 'bunch' of electrons in the storage ring, the periodicity of the light pulses corresponds to the orbiting time of this electron bunch. This period is invariably short (\sim 1 μ s) but extremely well defined. In order to utilise this time structure to determine the masses of desorbing ions it is clear, from the discussion of the time-of-flight ESD technique above, that the ions need to be accelerated substantially in order that flight times can be comparable with the radiation cycle

time. This has been done by accelerating the ions to \sim 2–3 keV. In doing so, the initial ion desorption energy (\lesssim 10 eV) becomes negligible, so that the flight time is determined just by the mass and the imposed acceleration. Some early results using this method at the synchrotron radiation source at Stanford in the USA, which has a cycle time of 780 ns, were described by Knotek *et al.* (1979). Notice, incidentally, that time-of-flight techniques also offer a solution to the problem of detecting negative ion desorption (e.g. Johnson *et al.*, 1988). As indicated in the discussion so far, most ESD and PSD experiments have detected only positive ion desorption, but there are certainly some adsorbate systems that preferentially yield negative ion desorption. A major challenge in their detection is the huge background of electron emission in the total negatively charged particle emission, but the much lower electron mass means that electron velocities, and thus flight times, are very much shorter than those of negatively charged ions.

Although ESD and PSD can provide important insights into the nature of adsorbed species including small molecules (the examples given above all involve atomic adsorbates but the desorption of whole molecules and that of molecular fragments have also been explored), it is important to recognise that the cross-sections for ion emission from different adsorption states can vary by many orders of magnitude. There are therefore many examples where the signals seen in ESD ion emission do not represent emission from all adsorbed states of a particular species, and indeed in some cases emission is seen only from a minority state on the surface. In large part this may be due to large differences in the reneutralisation or recapture probability of emission from different sites. In systems displaying the Knotek–Feibelman mechanism it may also be the case that desorption from defect sites at oxide surface is favoured.

One interesting development of the ESD technique is the study of the detected ion angular distributions, leading to the ESDIAD technique. Figure 6.41 shows the results of the first clear demonstration of strong angular effects in the detected ion yields from ESD. The experiment was performed in a retarding field analyser such as that shown schematically in Fig. 6.39, fitted with a multichannel plate amplifier and a phosphor screen detector (without the opaque spherical-sector collector shown in this figure). The sample was a W{100} crystal dosed with oxygen to produce an approximate coverage of 0.5 ML of atomic oxygen. Previous ESD studies of this W{100}/O system had shown that at higher oxygen coverages the O⁺ cross-section decreases by a factor ~2000, but in the lower coverage range used in the ESDIAD experiment the yield is ~10⁻⁶ ions per incident electron. The ESDIAD patterns of Fig. 6.41 were recorded after briefly heating the sample to successively higher temperatures and clearly show not only a strong angular dependence, but also marked changes in this angular

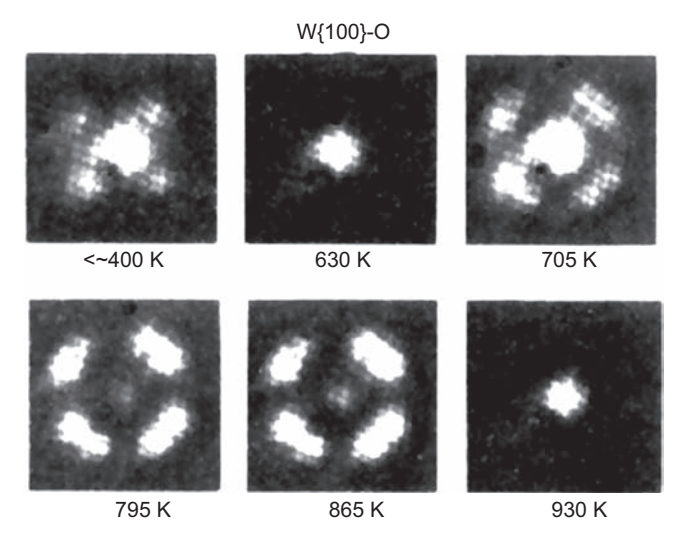


Fig. 6.41 Electron stimulated desorption angular distribution patterns for O⁺ obtained from W{100} after dosing with oxygen followed by briefly heating to an increasing range of annealing temperatures. Reprinted with permission from Czyzewski *et al.* (1974). Copyright 1974 by the American Physical Society.

dependence as a result of the different annealing cycles. The main features are the central emission peak along the surface normal and four symmetrically equivalent off-normal emission lobes in the <001> azimuths, corresponding to the close-packed directions of the surface W atoms. Although these results clearly demonstrate the existence of strong angular effects, which appear to be sensitive to the state of the surface and, presumably, the local adsorption sites, there are still no quantitative structure determinations of the associated surface phases more than 40 years after this experiment! However, many subsequent ESDIAD studies of molecular adsorbate systems have proved more easily interpretable. Although there has been a range of detailed theoretical studies (as reviewed by Ramsier & Yates, 1991), the basic conclusion emerging from these studies is that ion emission appears to occur along the direction of the bond that must be broken to release the detected ion (which may be an adsorbate–substrate bond or an intramolecular bond).

The results of an investigation of F^+ ESDIAD from PF_3 adsorbed on Ni{111}, shown in Fig. 6.42, provide a clear example of this effect. At low temperature the ESDIAD pattern shows six symmetrically equivalent off-normal emission lobes along the <110> azimuths which correspond to the two possible orientations of the PF_3 molecules that are known to adsorb atop surface Ni atoms. Of course, the Ni{111} surface is strictly only three-fold symmetric, but this lower symmetry is manifest only in the locations of the Ni atoms below the outermost layer; evidently

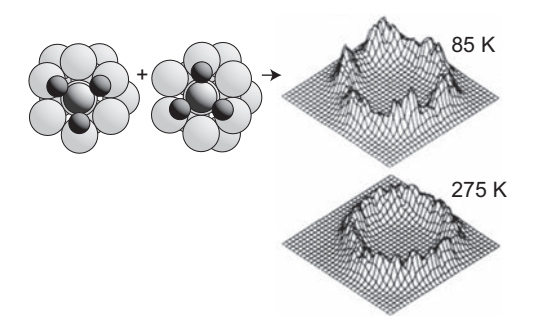


Fig. 6.42 Plan view of the structure of PF_3 on $Ni\{111\}$ together with F^+ ESDIAD patterns obtained from this surface at 85 K and 275 K with a low coverage of PF_3 . Adapted with permission from Alvey & Yates (1988). Copyright 1988 American Chemical Society.

the F atoms on the PF₃ are insensitive to the location of these lower-lying atoms. Notice that when the temperature is raised to 275 K the six-lobe pattern becomes almost circularly symmetric, indicating that the molecules become more free to rotate about the Ni–P axis perpendicular to the surface. The temperature at which this occurs provides an estimate of the activation barrier for this rotation. Notice, incidentally, that, as F is highly electronegative, one might anticipate that PF₃ would desorb F⁻ ions. Indeed, this does also occur and an ESDIAD study of F⁻ desorption from PF₃ on Ru(0001) yielded similar six-lobed patterns (Johnson *et al.*, 1988).

A further example of ESDIAD of a molecular fragment for which the emission angles can be reconciled with the directions of the broken bonds is provided by a study of the benzoate species, C₆H₅COO-, produced by deprotonation of the acid hydrogen of benzoic acid (C₆H₅COOH) through interaction with a Cu{110} surface (Lee et al., 2005). The local bonding geometry of this system (as determined by Pascal et al., 2001) is shown in Fig. 6.43(a), while the H⁺ ESIAD pattern is shown in Fig. 6.43(b). The three lobes can clearly be correlated with emission from the three hydrogen sites marked 'H' on the schematic diagram of the structure. An elegant extension of this experiment reported later by Yates (2012), shown in Figs. 6.43(c), (d), involved the use of benzoic acid deuterated at the site opposite the acid group, leading to a clear separation of the different hydrogen-desorbing contributions. Notice, though, that a number of corrections need to be applied to the polar angle of emission of the H⁺ lobes before a true correlation with the C-H bond angle relative to the surface can be achieved. One correction is purely instrumental and relates to the local electric field in the ESIAD analyser, but further corrections are required to account for the influence of image charge effects (Mi kovi et al., 1984) and reneutralisation (Mi kovi et al., 1986).

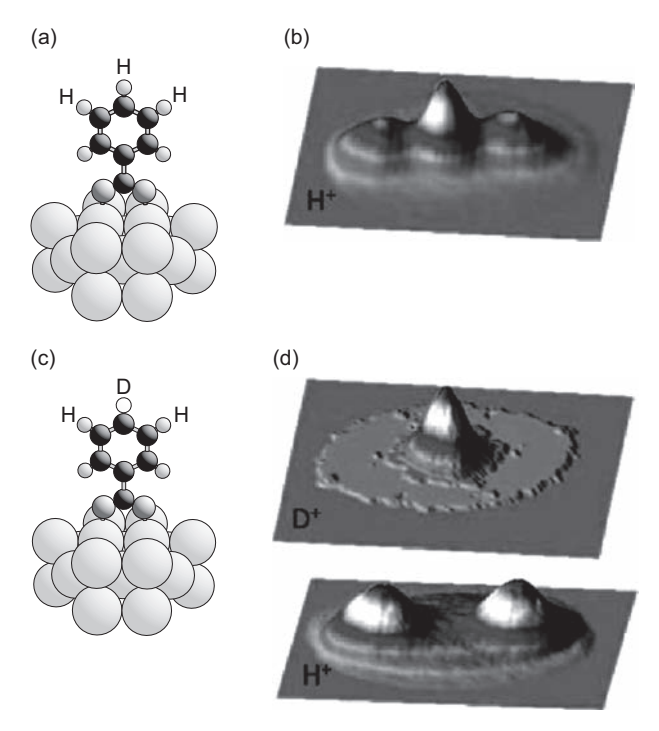


Fig. 6.43 (a) The bonding geometry of the benzoate species on $Cu\{110\}$; (b) the H^+ ESDIAD pattern obtained from this species. (c) The singly deuterated benzoate, 4-d₁-benzoate species on the surface; (d) the D^+ and H^+ ESDIAD patterns from this species. ESDIAD patterns reprinted with permission from Yates (2012). Copyright 2012 AIP Publishing LLC.

6.4 Measuring Adsorption

In the preceding sections of this chapter the emphasis has been on identifying molecular species on surfaces and gaining some insight into their properties. A rather different important question concerns the mechanisms involved in their adsorption and, of course, their adsorption energy, which may, as discussed above, be different from their desorption energy. When a molecule approaches a surface one of three things can happen: it may scatter from the surface (elastically or inelastically) back into the vacuum; it may be adsorbed into a strongly bound state (with adsorption energy much higher than kT); or it may be briefly adsorbed into a weakly bound state from which it will, after a short time, be thermally desorbed into the vacuum. These two adsorption possibilities are illustrated in Fig. 6.44, which shows simplified one-dimensional representations of the potential energy diagram seen by a molecule approaching a surface at a separation z. In general, two possible adsorption states are available, a strongly bound chemisorption state (which may be dissociative) and a weakly bound physisorption state that may be

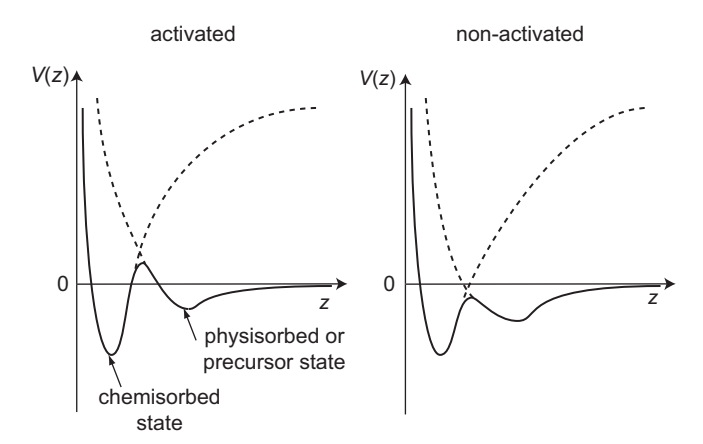


Fig. 6.44 One-dimensional potential energy curves experienced by a molecule approaching a surface at separation z; the chemisorbed state may be molecular or dissociative.

a precursor to the chemisorption state. Depending on the shape of these two potential energy curves there may be a potential energy barrier to reach the chemisorption state. If there is a barrier, transfer to the chemisorption state is activated and requires extra energy that may come from the kinetic energy of the incident molecule or the thermal energy in the solid surface. If there is no barrier, transfer to the chemisorption state is non-activated. The full details of the way in which the approaching molecule may be dissociatively adsorbed require more complex representation, for example by a two-dimensional potential energy surface that shows the dependence not only on the molecule–surface separation but also on the intramolecular distance between the dissociating fragments; a complete description requires a multidimensional surface that takes account of molecular orientation and lateral position on the crystalline surface. However, the one-dimensional description of Fig. 6.44 serves to illustrate the basic process.

The probability that the molecule is adsorbed onto the surface in a long-lived strongly bound state is referred to as the sticking probability or sticking coefficient, s, and measurements of this parameter are important in gaining an understanding of any specific molecule—surface combination. Of particular interest is the coverage dependence of the sticking probability, and information on this can be obtained by monitoring the increase in coverage with increased exposure using any technique that can determine the surface coverage in a quantitative fashion, such as XPS or AES (Chapter 2) or, indeed, TPD. The derivative of the uptake curve with respect to exposure gives the coverage dependence of the sticking probability. Converting this information into absolute values of s is more problematic. The simple kinetic theory of gases allows one to determine the rate at which molecules from the gas

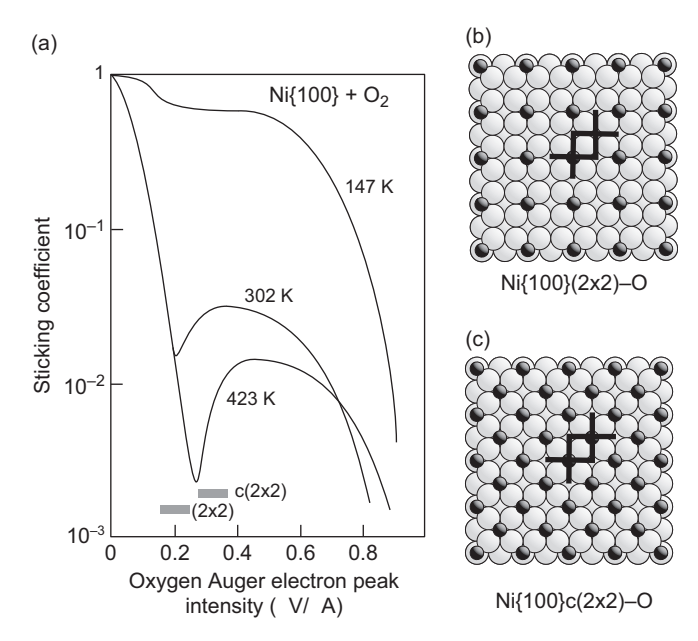


Fig. 6.45 (a) The sticking factor for molecular oxygen on Ni{100} as a function of O KLL Auger electron emission, as determined by Holloway & Hudson (1974). The smooth lines were drawn through the experimental data points. The shaded rectangles indicate the coverage ranges in which the LEED patterns of the two ordered chemisorption phases were clearest. Panels (b) and (c) are plan views of these two (atomic) chemisorption phases. The superimposed double crosses indicate the eight-site cluster found to determine the adsorption behaviour by Brundle *et al.* (1984).

phase impinge on the surface (see Chapter 1), but an accurate measurement of the partial pressure of the adsorbing gas *at the sample surface* is far from straightforward. Firstly, one needs to apply gas-species-specific sensitivity correction factors to mass spectrometer or ion gauge measurements. More significantly, if the chamber is continuously pumped to minimise the influence of contaminant desorption from surfaces within the chamber then the fact that these detectors are located at different positions in the sample chamber, relative to the position of the gas inlet, means that they will not measure the true pressure at the sample. Nevertheless, this approach can provide valuable information on the coverage dependence of *s*, if not its absolute value.

An early example of a study of this type that revealed interesting insights into surface structural influence on the sticking coefficient is provided by an investigation of the adsorption of oxygen on Ni{100} by Holloway & Hudson (1974). Specifically, AES was used to monitor the increase in oxygen surface coverage, at different sample temperatures, as a function of increasing exposure. Figure 6.45(a) shows the resulting dependence of the sticking probability on

coverage as monitored by the O KLL Auger electron emission (which is proportional to oxygen coverage in the chemisorption coverage range); the absolute values of s in this figure are based on the assumption that at zero coverage its value, s_0 is unity (as indicated by some earlier studies). A striking feature of these data is that, for sample temperatures of room temperature and above, there is essentially no temperature dependence of the low-coverage sticking probability (indicating non-activated adsorption) but its value decreases by up to three orders of magnitude as the (atomic oxygen) coverage reaches the value of 0.25 ML characterised by a (2×2) LEED pattern. At higher exposures the coverage rises again, leading to a $c(2\times2)$ LEED pattern consistent with a coverage of 0.5 ML. Figures 6.45(b), (c) show the known structure of these two phases, with oxygen atoms in four-fold coordinated hollow sites. However, a diffraction pattern consistent with the growth of NiO{100} also appears before this $c(2\times2)$ saturation coverage is reached. The results clearly indicate that a wellordered (2×2) surface phase almost completely blocks the uptake of surface atomic oxygen and thus the dissociation of these incoming molecules. This interpretation is reinforced by the fact that the sticking-coefficient dip is deeper at the higher temperature where the surface ordering should be improved and is almost absent at low temperature, where the surface order (as seen in LEED) is very poor. The fact that the sticking factor remains high at low temperature may be attributed to a molecular precursor state with sufficient lifetime for molecules to diffuse over the surface to find suitable dissociation sites rather than relying on direct impact at these favourable sites. In view of the sharp dip in sticking coefficient at 0.25 ML it was concluded that the key requirement for oxygen dissociation was that of two empty next-nearest-neighbour hollow sites. A perfect (2×2) phase (at a coverage $\theta = 0.25$ ML) has no such sites, so if adsorption requires the molecule to arrive at such sites directly from the gas phase then the sticking factor must vary with coverage as $1.0 - 4\theta$, a conclusion that is in modest agreement with the experimental data.

Subsequently, however, Brundle and coworkers (Brundle *et al.*, 1984; Brundle, 1985) showed that a significantly better description of these data can be achieved by a model in which the requirement for dissociation is an eight-site cluster (indicated by the ends of the set of lines forming crosses superimposed on the structure diagrams of Figs. 6.45(b), (c)); these clusters consist of two vacant next-nearest-neighbour hollow sites, each of which has all nearest-neighbour sites vacant. The availability of these clusters requires the presence of one oxygen vacancy on the (2×2) surface (so a perfect (2×2) surface blocks adsorption), while two nearest-neighbour oxygen vacancy sites are required in the $c(2\times2)$ surface. This same model was used by Brundle to account for the fact that the close-packed Ni{111} surface is more readily oxidised than the more open-packed Ni{100},

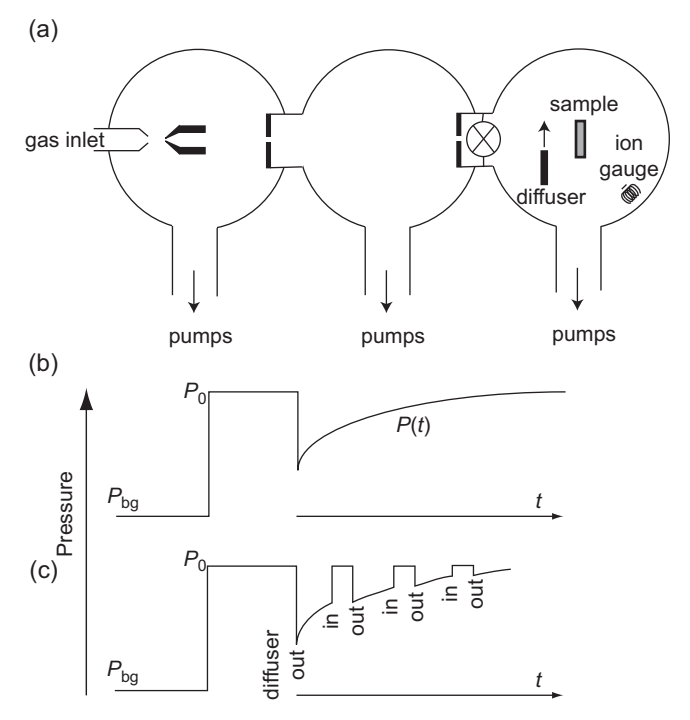


Fig. 6.46 (a) Schematic diagram of the key components of the molecular beam instrument used to measure sticking coefficients by the method of King & Wells (1972, 1974). Panels (b) and (c) show the time dependence of the sample chamber pressure for two different sequences of interposition of a diffuser into the beam.

contrary to expectations, the reason being related to the nature of the ordered chemisorption phases formed on the two surfaces.

While this example of a study of relative sticking coefficients clearly leads to considerable insight into the detailed kinetics of the uptake of molecules on a surface, there is also a need to determine absolute values; a conceptually very simple method, now widely exploited, was introduced by King & Wells (1972, 1974). The method is based on the use of a molecular beam instrument operating in essentially the same fashion as the atomic beams described in section 3.1.6.1 in the context of helium atom diffraction studies. The key ingredients of the instrumentation are shown schematically in Fig. 6.46. A succession of separately pumped chambers, separated by small defining apertures (there were five such chambers in the original instrument of King and Wells) provides the necessary differential pumping to ensure that UHV conditions can be maintained in the sample chamber and that a well-defined molecular beam is produced at the sample (with a flux of $\sim 10^{16}-10^{17}$ molecules m⁻² s⁻¹ onto a sample area of $\sim 4 \times 10^{-6}$ m²). As an alternative to the beam hitting the sample, a 'diffuser' (a glass rod in the original experiments) can be interposed that is expected to have a sticking probability of

zero. The basic experimental procedure, indicated in Fig. 6.46(b), is that the valve to the sample chamber is first opened with the diffuser in place in front of the sample, leading to an initial chamber pressure of P_0 ; the chamber pressure P(t) is then recorded, as a function of time after the diffuser is removed, when the beam hits the sample. The sticking probability is then given by

$$s(t) = [P_0 - P(t)]/(P_0 - P_{bg})$$
(6.33)

where $P_{\rm bg}$ is the background pressure in the absence of the molecular beam. Notice that the method does not require detailed knowledge of the molecular beam flux nor, indeed, of the exact calibration of the pressure gauge (as long as its response is linear in pressure). However, including a calibration of the molecular beam flux density does also allow the absolute adsorbate coverage to be determined as a function of time from the integral of s(t). The method relies on the assumptions that the pumping speed in the sample chamber is constant and that the molecules that do not adsorb on the sample produce a completely randomised contribution to the gas pressure in the sample chamber. In this regard it is important to locate the ion gauge in the chamber in a position that minimises the effect of the directional components of these scattered molecules. A slightly improved strategy for the experiment (King & Wells, 1974), illustrated in Fig. 6.46(c), involves moving the diffuser in and out of the beam a few times during the adsorption sequence to allow further readings of P_0 , a parameter that may change slightly owing to the increasing gas load on the pumping. Subsequent variants of the King and Wells method have involved not only direct detection of the reflected molecular beam using a mass spectrometer (rather than relying on the scattered molecules becoming randomised in the gas pressure measured elsewhere in the chamber) but also the use of line-of-sight mass spectrometry to monitor the gas pressure in front of the sample; this method does not require a molecular beam source (Hessey & Jones, 2015). Of course, these methods, based on time-dependent changes in partial pressures, are only effective if the sticking coefficient is reasonably large (> ~0.01); by contrast, methods based on determining the surface coverage as a function of exposure can be used to determine a much wider range of values of the (relative) sticking coefficient.

The use of molecular beams has also played an important role in a wide range of increasingly sophisticated studies of molecule–surface interactions. For example, the use of supersonic nozzles sources (see section 3.1.6.1), hot nozzles or seeding allows the translational and vibrational energies of the molecules to be varied; thus detailed investigations of barrier heights in activated adsorption systems may be obtained. The use of optical resonant-enhanced multiphoton ionisation (REMPI, see e.g. Ashfold & Howe, 1994) has also allowed the determination of the rotational and vibrational states of desorbing molecules. Using this approach,

changes in these states induced by incident beam reactions, by thermal desorption or by ESD can be found, providing exceptionally detailed information on the surface reactions. Further details of these studies are provided in the review by Hodgson (2000).

An important parameter that one would wish to measure is the adsorption energy. As remarked earlier, this is not necessarily the same as the desorption energy, because thermal desorption occurs at elevated temperatures, at which changes in the state of the adsorbed species may have occurred. Of course, TPD offers a route to measure the desorption energy only of species that desorb at accessible temperatures and, in the case of molecular adsorbates, that desorb intact. One method of gaining access to the adsorption energy is to explore the equilibrium between the rate of arrival of molecules at the surface and their rate of desorption as a function of gas pressure and surface temperature. By measuring the surface coverage θ as a function of the temperature T and pressure P, one can plot P against P at constant P, giving an isostere. According to the Clausius–Clapeyron equation,

$$\frac{\ln P}{(1/T)} = \frac{\Delta H_{\text{ads},\theta}}{R} = -\frac{q}{R} \tag{6.34}$$

The gradient of this plot, -q/R, gives the isosteric heat of adsorption, q, where R is the gas constant. This approach is generally only used to study very weakly adsorbed species, for which the adsorption-desorption equilibrium can be achieved at modest temperatures (even below room temperature); it is not generally regarded as a viable approach for determining chemisorption energies. However, an early investigation by Tracy & Palmberg (1969) showed that it could be used to study a chemisorption system, notably CO on Pd{100}. To achieve the necessary equilibrium, $P T \theta$ data were collected, using the work function as a monitor of surface coverage, in the temperature range 300-500 °C; this is the temperature range in which CO desorption is observed in this system in TPD experiments. Of course, this measurement suffers from one of the limitations of TPD itself, namely that, at the elevated temperature required for desorption (and thus surface-gas-phase equilibrium), the molecular state on the surface may differ from that into which the molecule is adsorbed at lower temperatures. The advantage of the above approach over TPD, highlighted by the authors, is that extracting the adsorption energy does not require any detailed understanding of the desorption process, such as the order of the desorption; it also circumvents the need to assume a value for the pre-exponential factor in the desorption rate, as is commonly done in many TPD studies that use the simple plot of Fig. 6.33.

Direct access to adsorption energies of even strong chemisorption, however, is provided by calorimetry, the adsorption energy being converted into heat and thus into a temperature rise. While the principle of calorimetry is simple and was applied successfully to the study of adsorption on high-area metal films and thin wires many years ago (erný, 1996), the application of this method to determine adsorption energies on single-crystal surfaces is far more challenging. The basic problem is that the surface area is small, so the total amount of heat generated by adsorption is also small, while a sample with typical thickness ~1 mm is relatively massive, leading to an exceedingly small temperature rise. Single-crystal adsorption (micro) calorimetry (SCAC), pioneered by King and coworkers and reviewed by them in the paper by Brown et al. (1998), thus has two key requirements, namely samples with a very low heat capacity relative to their surface area (i.e. very thin samples) and a very sensitive method of detecting temperature rises. The key to achieving very thin samples (initially only 200 nm thick, although subsequently 1 µm thickness has been more common) was the use of metal films grown epitaxially on NaCl, the substrate subsequently being dissolved in water while the films were cold-welded to a ring of the same material as the single crystal. This technique was developed by Jacques Chevallier at the University of Århus, who supplied these special samples for all the early SCAC experiments. In the first SCAC experiments, temperature rises due to the adsorption of small doses of adsorbate gas, delivered by a pulsed molecular beam source, were measured by detecting the emitted infrared radiation with a mercury cadmium telluride sensor (see Fig. 6.47(a)). Notice that by using a short pulse (~50 ms) of the molecular beam, striking only the central region of a few millimetres of the ultrathin sample, the lateral heat conduction away from this region is slow while the heat conduction to the back of the sample is rapid, making it possible to detect IR emission from the back of the sample. Calibration of the instrument, relating the detector signal to the amount of heat generated in the sample, was achieved by the use of a pulsed HeNe laser of known power. While the detection of emitted IR radiation provided the first convincing results of this SCAC approach to determining adsorption energies, the fact that the radiated power in a temperature rise ΔT is proportional to $T^3\Delta T$ means that it is not really viable for studies at sample temperatures below ~300 K. This method of determining the temperature rise has since been superseded by the use of pyroelectric materials in close contact with the back of the sample during measurements (Fig. 6.47(b)).

Campbell and coworkers have been responsible for a number of significant design improvements in this basic approach, including the use of metallised pyroelectric polymer detectors, and they have provided more recent reviews of the technique (Lytken *et al.*, 2008; Crowe & Campbell, 2011) as well as later details of improved detectors (Lew *et al.*, 2010) and SCAC instruments (Fisher-Wolfarth *et al.*, 2011). For a 1 µm thick Pt{111} sample this improved sensitivity led to a pulse-to-pulse standard deviation in the heat of adsorption of just 1.3 kJ/mol (i.e. 0.013 eV per molecule), with molecular beam pulses corresponding to only

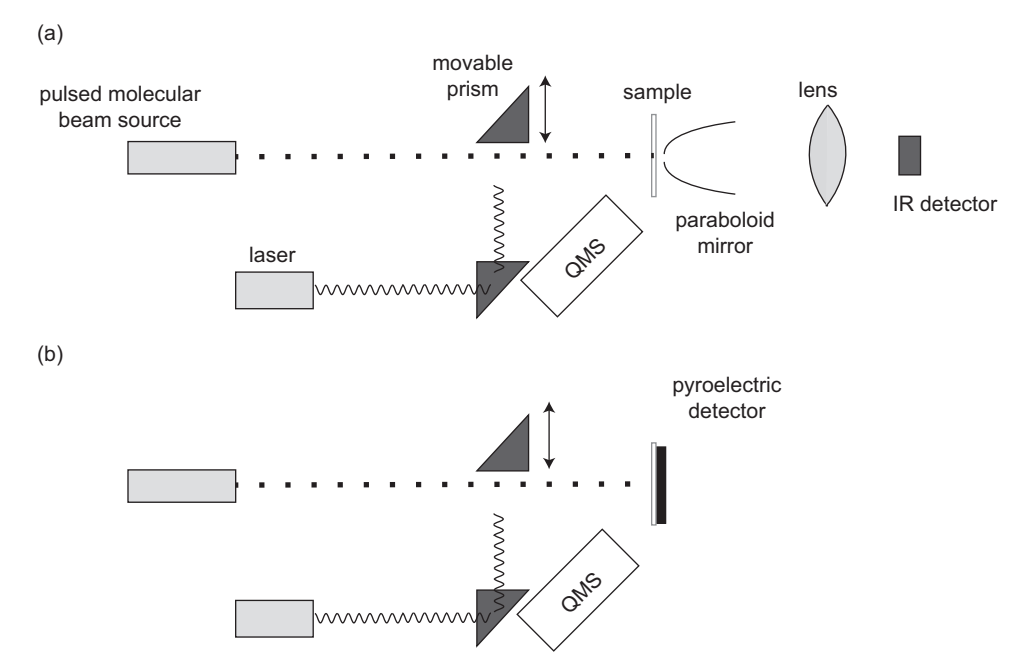


Fig. 6.47 Simplified schematic showing the key ingredients of SCAC instrumentation. (a) The IR detection system first adopted by King and coworkers; (b) the alternative pyroelectric detection approach, also adopted by King but developed and refined by Campbell and coworkers. The quadrupole mass spectrometer (QMS) is used to determine sticking factors on the basis of the King and Wells approach.

1.1% of a monolayer on the surface. Moreover, this improved sensitivity can be used to apply the SCAC technique to much thicker samples, in excess of $100~\mu m$, a thickness that can be achieved by the mechanical polishing of bulk crystals, opening the technique to a much wider range of materials.

Figure 6.48 shows examples of some results from King and coworkers (Fiorin et al., 2009) using the original IR detection scheme with 200-nm-thick Pt crystals. Results for O₂ and NO interaction with Pt{111} at room temperature may be compared with those obtained from two stepped surfaces, i.e. Pt{211} with narrow {111} terraces separated by a single atop step of {100} character, and {411} involving more {100}-character areas. The data have been plotted with the surface coverage expressed in terms of the number of molecules per unit area, because the coverages associated with 1 ML are very different for the three faces. This arises because on a stepped surface the coplanar layers have very small interlayer spacings – the actual number of surface atoms accessible to adsorbates on surfaces is significantly larger than 1 ML if defined in the usual way. A key question addressed by these data is the role of surface steps in the bonding and dissociation

of adsorbed molecules. On Pt{111}, with no steps, O₂ is known to dissociate. However, the results provide more detailed information. In particular, the adsorption heat falls quite markedly for coverages greater than 0.25 ML (0.33 \times 10¹⁵ atoms cm $^{-2}$), a value that correlates with an ordered (2×2) adsorption phase. The fall in adsorption energy is attributed to next-neighbour-oxygen lateral repulsion and is based on the fact that the drop in binding energy (per incident O₂ molecule) is from 3.10 eV to 1.55 eV, each O atom being surrounded by six next-nearest neighbours with (atomic) repulsion energy estimated to be $(3.10 - 1.55)/(6 \times 2) =$ 0.13 eV. Although this dissociation occurs readily on the {111} face at low coverage, it is notable that the initial adsorption energy is higher on the {411} face, which can be attributed to preferential adsorption on the {100}-like sites at the steps on this surface that are available at low coverage. In the case of NO adsorption, a key question is whether the adsorption is molecular or dissociative. On the {111} face it is known to be molecular, NO initially being adsorbed into the most favourable hollow site up to a coverage of 0.25 ML, corresponding to a (2×2) phase; at higher coverages adsorption occurs at the less favourable atop sites. This seems to correlate with the break in the gradient of the adsorption energy at this coverage. Earlier investigations by other techniques had led to the conclusion that NO dissociation does occur on the stepped Pt surfaces. The heat of adsorption results of Fig. 6.48 show higher values for both these surfaces than for the {111} surface, although for the {211} face the difference is quite small; nevertheless, the authors concluded that this was consistent with initial dissociation.

Single-crystal absorption calorimetry studies of this type have been conducted on a range of small molecules on transition metal surfaces and were collated by Wellendorf *et al.* (2015), who also compared the reported values of adsorption energies with the results of a range of DFT calculations.

6.5 Some Comparisons

This chapter has covered a range of different methods under the general umbrella of identifying (and investigating) molecular species on surfaces.

While elemental analysis techniques such as XPS and AES, described in Chapter 2, provide a means to determine the identity of the atoms present on a surface, they are of limited value in establishing the molecular character of surface adsorbates. Chemical shifts in XPS (discussed in Chapter 5) do provide a spectral fingerprint that can help to identify molecular components, but substantially more detailed characterisation is offered by vibrational spectroscopies. The energies of the vibrational modes of molecules and molecular fragments are far more specific, and vibrational spectroscopies typically show peaks associated with these modes that are narrow relative to the spectral range investigated. The great majority of

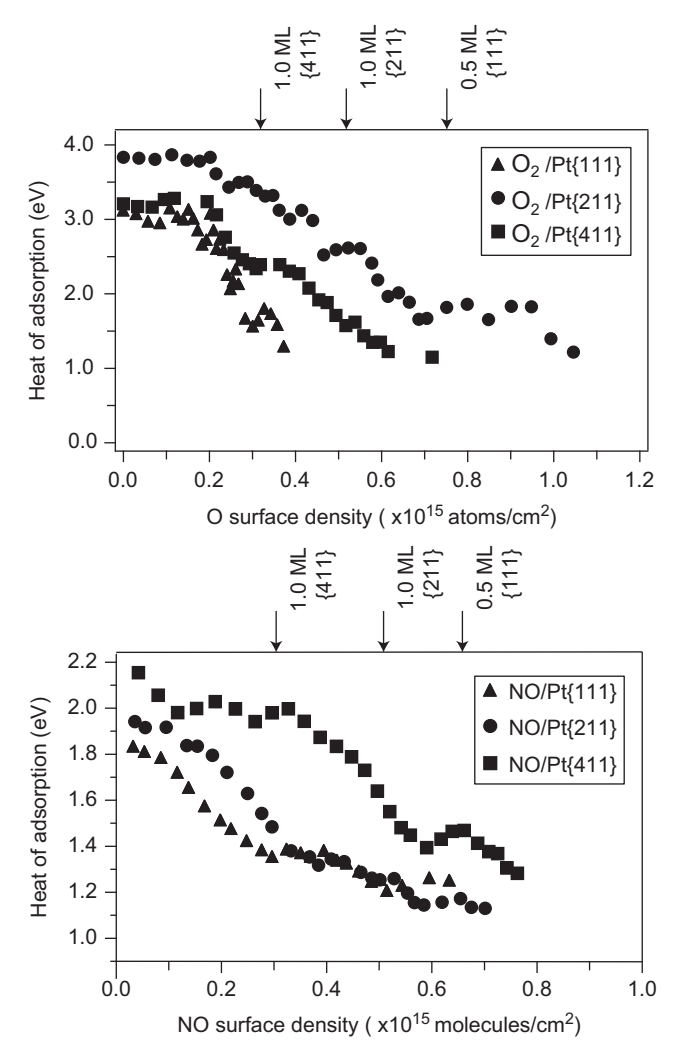


Fig. 6.48 Results of SCAC measurements of the coverage-dependent heat of adsorption associated with oxygen and NO adsorption on Pt{111}, and on two stepped Pt surfaces, {211} and {411}. Coverages corresponding to 1 ML or 0.5 ML on the three different surfaces are indicated by the arrows. Reprinted from Fiorin *et al.* (2009), copyright 2009, with permission from Elsevier.

such experiments are performed with either RAIRS or HREELS. The former technique has the advantage of higher spectral resolution and is applicable in non-UHV environments, so it can be used to study gas—surface reactions at higher pressures. Its strong dipole selection rule means that not all vibrational modes of the molecule are accessible, while the need for a window limits the spectral range at low energies, typically meaning that adsorbate—surface stretching frequencies are not accessible. The HREELS technique offers a wider spectral range but with

poorer resolution and the UHV constraint that characterises incident low energy electron techniques. The combination of both dipole-active and impact-active modes in HREELS means that more vibrational modes can be accessed and, with careful experiments in different geometries and at different energies, more complete orientational information may be available. As yet, at least, SFG is something of a niche technique as an alternative to RAIRS. Its real strength is its applicability to high pressure environments and its ability to probe even buried interfaces, although there have also been some notable successes in applications to UHV surfaces.

The iHAS technique is primarily of interest in the study of surface phonon modes, where its notable strength is the ability to map phonon bands (HREELS also offers this possibility, which has less often been exploited). The fact that it is able to access only rather low frequency vibrational modes (with an energy significantly less than that of the incident atoms) means it is unable to access many of the dominant molecular stretching modes that prove so useful in molecule characterisation using RAIRS or HREELS.

The STM-IETS technique provides a very different way to probe vibrational modes in adsorbed molecules. It is far more experimentally challenging than RAIRS or HREELS but offers a unique capability to identify local vibrational modes within adsorbed molecules on a submolecular spatial scale. It is not a competitive technique for routine molecular characterisation but offers exquisite control in highly detailed studies of single-molecule adsorption and reaction investigations.

The alternative approach to identify molecular character in adsorbates is using valence-band photoemission (and inverse photoemission). The fact that these molecular orbital valence states occur within a range of only 10–20 eV and that spectral peaks are commonly ~1 eV or more in width makes this approach less specific than the vibrational spectroscopies in identifying molecular character, particularly in larger molecules. However, if the contributions from specific molecular orbitals can be identified in angle-resolved photoemission then significant information on molecular orientation can be extracted, even resulting in molecular orbital imaging in systems in which the orbital tomography technique is applicable.

The other techniques described in this chapter relate more to investigations of how molecules interact with surfaces and, in particular, the energies of adsorption and identifying surface reactions (for which the molecular spectroscopies described above are also important). The classic method to determine desorption energies is TPD and, along with TPRS can identify the character of desorbing molecules through their molecular mass. Relatively simple standard TPD experiments allow one to identify differing adsorption states of an adsorbate on a surface

and can provide estimates of the desorption energies, even using the simple Redhead graph of Fig. 6.33 and an assumed value of the pre-exponential factor in the desorption-rate equation, although substantially more careful analysis is required to extract more accurate energy values. Measuring adsorption energies through microcalorimetry is substantially more challenging experimentally, but significant advances have been made in this technique since the original pioneering experiments, and a number of groups worldwide are exploiting this technique.

A rather different source of information regarding adsorption mechanisms is provided by sticking probabilities, and here variants of the King and Wells approach dominate modern studies, although simple surface-uptake measurements monitored by surface composition spectroscopies still offer a valuable source of information on relative coverage-dependent changes in sticking probabilities.